Dissertation
submitted to the
Combined Faculties for Natural Science and for Mathematics
of the Ruperto-Carcla University of Heidelberg, Germany
for the degree of

Doctor of Natural Sciences

presented by

M.Sc Fanzhen Meng

born in Weifang,China

Oral examination: January 10 th 2007

IR Spectroscopy Studies of Silver and Copper Nano-films

Referees: Prof. Dr. Annemarie Pucci
Prof. Dr. Josef Bille

IR studies of Silver and Copper nano-films

The present work is focused on the infrared optical properties of thin Ag and Cu films grown on MgO(001) and the Surface-Enhanced Infrared Absorption (SEIRA) of CO on these metal films. During both the deposition of the metal films onto MgO(001) and gas exposure to the metal films at low temperatures ($< 100\,\mathrm{K}$) in Ultra High Vacuum (UHV), infrared spectra were captured in situ in transmission or reflection geometry. Afterwards the surface morphology of the films was examined ex situ by atomic force microscopy (AFM). For the first time, an infrared reflectance minimum was found during the metal film growth. The infrared optical properties of some films can be described by the Drude-type model or the Effective Medium Model. The Ag films show different surface morphologies at different substrate temperatures and at different final thicknesses. Also the SEIRA of CO adsorbed on Ag films is strongly related to the surface morphologies. The Cu films prepared at room temperature show island like surface morphology. SEIRA of CO adsorbed on Cu films shows differences depending on the Cu island size.

Infrarotuntersuchungen an Silber- und Kupfer-Nanofilmen

Die vorliegende Arbeit konzentriert sich auf die infrarotoptischen Eigenschaften dünner Silber- und Kupferfilme, die auf die MgO(001)-Oberfläche aufgedampft wurden, und oberflächenverstärkte Infrarot-Absorption (SEIRA) von auf diesen Filmen adsorbiertem CO. Sowohl während des Abscheidens der Metallfilme als auch während der Gasangebote bei tiefen Temperaturen ($<$100K) im Ultrahoch-Vakuum (UHV) wurden Infrarotspektren in situ in Transmissions-bzw. Reflexionsgeometrie aufgenommen. Die Oberflächen-Morphologie wurde anschließend ex situ mittels Rasterkraft-Mikroskopie (AFM) vermessen. Erstmalig konnte ein Infrarot-Refektivitätsminimum während des Metallfilmwachstums gefunden werden. Die infrararotoptischen Eigenschaften einiger Filme können durch Drude-artige Modelle bzw. Effektiv-Medien-Modelle beschrieben werden. Die Silberfilme zeigen bei verschiedenen Substrattemperaturen und verschiedenen Filmdicken unterschiedliche Morphologien. Auch SEIRA von auf Ag-Filmen adsorbiertem CO hängt stark von der Oberflächenmorphologie ab. SEIRA von CO auf Cu-Oberflächen zeigt Abhängigkeiten von der Größe der Cu-Inseln.

Contents

1 Introduction

Materials are named "nano-materials" if at least one dimension of them is well below 1000 nm. Nanosized metal films are interesting materials because of their novel chemical, physical, mechanical and optical properties compared to the bulk materials. Many deposition technologies are available for the preparation of metal nano-films (see Ref [1] for a review). One of the oldest techniques—thermal evaporation or vacuum evaporation—is still widely used.

Thin film growth is usually classified into three modes based on thermodynamic arguments: the Frank-van der Merwe mode (2D growth), the Volmer-Weber mode (3D growth) and the Stranski-Krastanov mode (first 2D then 3D growth). Bauer has developed a thermodynamic criterion for the growth mode [2] under equilibrium conditions. The criterion states that the growth mode is determined by an energy difference $\triangle\sigma$: $\triangle\sigma = \sigma_f + \sigma_i - \sigma_s$, where σ_f is the surface free energy of the film, σ_i is the free energy of interface and σ_s is the surface free energy of the substrate. 2D growth is preferred if the sign of the energetic difference is positive. The Stranski-Krastanov mode is the intermediate case, where this energetic difference changes sign at a critical layer thickness provoking a transition from 2D to 3D growth. However, the growth is a non-equilibrium phenomenon. Metal film growth usually proceeds through nucleation and growth stages. Such stages involve adsorption, surface diffusion, chemical binding and other atomic processes at surfaces. Theory of diffusion, nucleation and growth has been developed to describe the atomistic processes involved in the film growth [3, 4]. A critical size was often defined for describing the transition from the nucleation stage to the growth stage. In § 2.6 we cite the kinetic equations developed by Venables *et al.* [3], which gives a quantitative description of nucleation and growth and helps to illustrate some results in this work.

The surface or interface properties and the temperature of the substrate can drastically influence thin film characteristics due to surface contamination, nucleation effects, surface mobility, adsorbed gases, surface morphology, and crystallographic orientation etc. [1]. There are a lot of experimental means for the analysis of thin films and their surfaces, for example, Low-energy Electron Diffraction (LEED), IR spectroscopy, Surface-enhanced Raman Scattering (SERS), Surface-enhanced IR Absorption (SEIRA), and Scanning Probe Microscopy (SPM) etc. [5]. We apply IR spectroscopy and Atomic Force Microscopy (AFM, one kind of SPM) for the study of film growth under various conditions in this work. Although IR spectroscopy can not resolve the sub-monolayer growth, it offers information about the film conductivity. A film at the percolation threshold is indicated by a frequency independent transmittance

in IR spectroscopy [6]. A percolated film can be described by a Drude type model. The effect of the substrate temperature, adsorbed gases and the substrate surface prepared by different ways on the film growth are also recognizable from IR spectroscopy. With AFM the surface morphologies of films prepared under various conditions are examined. There are already reports [7] about the temperature dependent morphology of Cu films. In this work we present the temperature dependent morphology of Ag films grown on MgO(001) surfaces.

The effect of surface enhanced IR absorption (SEIRA) was first discovered on island metal films by Hartstein *et al.* in 1980s [8]. SEIRA of CO due to atomic scale roughness was often observed on cold-deposited films at a temperature below 50 K [9, 10, 11, 12]. However the SEIRA of CO adsorbed on Ag films at 100 K is rarely reported. At 100 K, we find that the SEIRA effect is very strong when CO adsorbs on Ag films prepared at or above 300 K. This strong enhancement is attributed to the excitation of transverse collective electron resonances by the incident radiation polarized parallel to the array of islands [13, 14]. The small channels (about 5 nm) between islands are very crucial for the enhancement [13]. SEIRA of CO adsorbed on Cu films at 100 K was already studied [15, 16].

The aim of this thesis is to demonstrate the ability of FTIR for investigating the IR properties of nanofilms. The growth process of ultra-thin Ag and Cu films on MgO(001) and the adsorption of CO gas on such film surfaces at low temperatures have been investigated. Ag/MgO(001) is an interesting system because of the little lattice misfit ($<3\%$), which is therefore favored by both theoretical and experimental researchers.

The organization of this thesis is as follows: In chapter 2, some basic theories related to our data analysis and the properties of the material we used in this work are introduced. For example, the Drude theory, effective medium theory, the theory of metal film growth, the optical properties of bulk metal and thin films, and the ground theory of gas adsorption are shortly introduced. In chapter 3, the experimental techniques and instruments, and the preparation method of samples are shown. Chapter 4 contains the experimental results and the analysis of Ag/MgO(001) system and chapter 5 contains that of Cu/MgO(001) system. Finally in chapter 6, we briefly summarize the results presented in this thesis.

2 Basic Theory

2.1 IR Spectroscopy

IR spectroscopy and particular Fourier transform IR (FTIR) spectroscopy is a very useful tool for determining the molecular composition and structure, and for measuring the optical properties of nanolayers located not only on a solid surface but also at solid-gaseous, solid-liquid, liquid-gaseous, and solid-solid interfaces. IR spectroscopy offers various modes for sample measurement, e.g., transmission, diffuse transmission, diffuse reflection (DRIFTS), external IR reflection (IRRS), and attenuated total reflection (ATR) etc. In this work we perform transmission and external reflection measurements during thin metal-film deposition on MgO(001) and CO molecules adsorption on metal films in an ultra high vacuum (UHV).

The reflection and transmission spectra of a thin film can be calculated from the electromagnetic theory, in terms of the refractive index and thickness of the film [17, 15, 18] as shown in § 2.2. For analyzing the infrared spectra of adsorbed molecules on metal films, we introduce some basic information here.

Molecules possess discrete levels of rotational and vibrational energy. A vibrational transition at frequency ω_0 will occur when the molecules absorb photons which have the same frequency as ω_0 in the infrared range (wavelength 1-1000 μm, wave numbers 10000-10 cm^{-1}, energy differences 1240-1.24 meV). In Fig. 2.1 we show a simple sketch map about how an alternate electric field interacts with the dipole in a molecule. We call the molecules IR active if they show a change on the dipole moment during vibrating. Otherwise they are IR inactive and can not be detected by IR spectroscopy. Generally, polar molecules are IR active. For example, CO molecules in gas phase show an IR absorption line at 2143 cm^{-1}.

When a molecule adsorbs on a metal surface, it loses the rotational degrees of freedom, and its dipole will induce an instantaneous image dipole in the metal, as shown in Fig. 2.2. The dipole parallel to the metal surface was cancelled by its image dipole. However, the dipole perpendicular to the metal surface has the same orientation as its image, so its dipole moment is doubled. This is called image effect. Also from the basic laws of electrostatics we know that outside a conductor near its surface the electric field is always perpendicular to the conductor surface. As shown in Fig. 2.1, since the IR absorption is defined by the interaction between the oscillating dipoles of the molecules and the electric field, the result of these two effects is that only a vibration perpendicular to the metal surface can be detected. This selection rule is

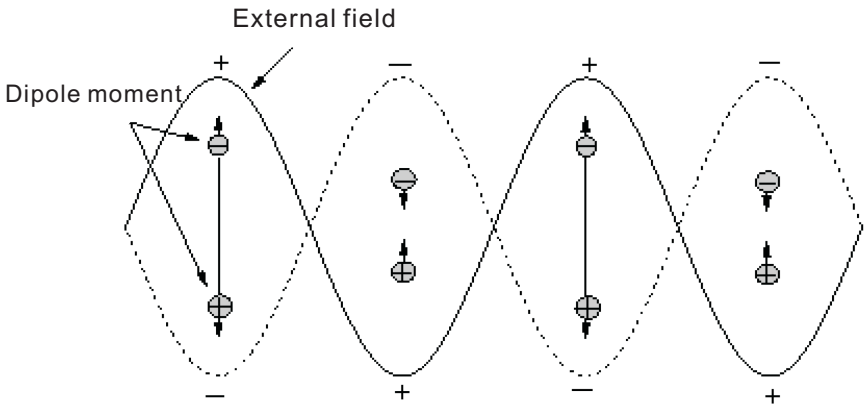

Figure 2.1: Interaction between the alternate electric field from IR radiation and the dipole in a molecule. The arrows show the direction of the forces generated by the external electric field on the dipole in a molecule. The external field changes the dipole moment by pulling or compressing the dipole.

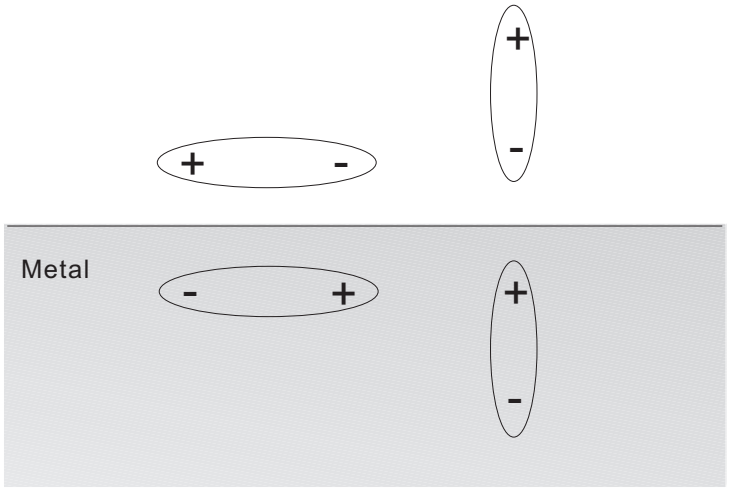

Figure 2.2: The dipoles and their induced dipoles on a metal surface.

rather universal, being valid not only for a smooth but also for a rough metal surface and metal particles.

Now we consider a dipole mode perpendicular to the metal surface (normal mode) having a non zero dynamic dipole moment ρ [15]:

$$\rho \propto \partial p/\partial q_i \neq 0, \tag{2.1}$$

where p is the electric dipole moment, q_i is the normal coordinate. The value of p depends on the relative ionicity of the species and can be obtained only by quantum-chemical calculations. Generally, the more polar the bond the larger the p term is. The matrix element of the dynamic dipole moment, $|\langle j\,|\rho|\,i\rangle|$, is called the transitional dipole moment (TDM) of the corresponding normal mode. The integral intensity A of the absorption band of the normal mode is proportional to the *probability* per unit time of a transition between an initial state i and a final state j. The *probability* is proportional to the square of the element of the Hamiltonian $\hat{H} = \hat{E} \cdot \hat{\rho}$, where E is the electric field vector, resulting in the absorption[18, 15]

$$A \propto E^2 \,|\langle j\,|\rho|\,i\rangle|^2 \cos^2 \vartheta, \tag{2.2}$$

where ϑ is the angle between vector E and ρ. This equation gives a mathematical view of the selection rule. An excitation is active if a change of the dipole moment takes place and the projection of this change onto the direction of the electric field is nonzero. A maximum is observed when E is parallel to the dynamic dipole. For adsorbed molecules, E is the localized electric field vector on the metal surface.

2.2 Transmission and Reflection at Interfaces

2.2.1 Two-phase System

Let us imagine an electromagnetic radiation propagates in medium 1 with refractive index n_1 and in medium 2 with refractive index n_2 ($n_2 > n_1$). Both media are assumed to be homogeneous and isotropic and are described by dielectric function of ε_1 and ε_2. At the interface ($z = 0$), as we can see from Fig. 2.3, the incident beam splits into a reflected and a transmitted component. The incident beam, the reflected beam, and the normal to the interface at the point of incidence all lie in the same plane (the plane of incidence). The angle of incidence θ_i, the angle of reflection θ_r, and the angle of refraction θ_t are related by the Snell's law [18]:

$$\theta_i = \theta_r, \tag{2.3}$$

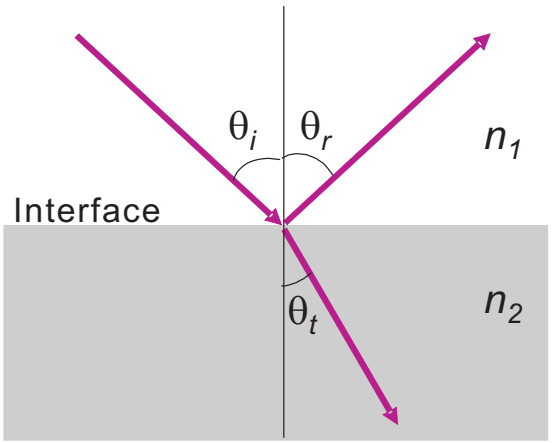

Figure 2.3: Reflection and refraction at interface of two phases, $n_1 \neq n_2$. θ_i denotes the angle of incidence, θ_r denotes the angle of reflection, and θ_t denotes the angle of refraction.

$$\frac{\sin\theta_t}{\sin\theta_i} = \sqrt{\frac{\varepsilon_1}{\varepsilon_2}} = \frac{n_1}{n_2}. \tag{2.4}$$

At the interface, for p- and s-polarized radiation, the electric field amplitude of the reflected ($E_{r,p}$ and $E_{r,s}$) and transmitted ($E_{t,p}$ and $E_{t,s}$) beam are connected to that of the incident beam ($E_{i,p}$ and $E_{i,s}$) by *Fresnel* coefficients r_p, t_p, r_s and t_s [18]:

$$r_p = \frac{E_{r,p}}{E_{i,p}} = \frac{\varepsilon_2\cos\theta_i - \sqrt{\varepsilon_1\varepsilon_2 - \varepsilon_1^2\sin^2\theta_i}}{\varepsilon_2\cos\theta_i + \sqrt{\varepsilon_1\varepsilon_2 - \varepsilon_1^2\sin^2\theta_i}} = -\frac{n_1\cos\theta_t - n_2\cos\theta_i}{n_1\cos\theta_t + n_2\cos\theta_i} \tag{2.5}$$

$$t_p = \frac{E_{t,p}}{E_{i,p}} = \frac{2\sqrt{\varepsilon_1\varepsilon_2 - \varepsilon_1^2\sin^2\theta_i}}{\varepsilon_2\cos\theta_i + \sqrt{\varepsilon_1\varepsilon_2 - \varepsilon_1^2\sin^2\theta_i}} = \frac{2n_1\cos\theta_i}{n_1\cos\theta_t + n_2\cos\theta_i}, \tag{2.6}$$

$$r_s = \frac{E_{r,s}}{E_{i,s}} = \frac{\sqrt{\varepsilon_1}\cos\theta_i - \sqrt{\varepsilon_2 - \varepsilon_1\sin^2\theta_i}}{\sqrt{\varepsilon_1}\cos\theta_i + \sqrt{\varepsilon_2 - \varepsilon_1\sin^2\theta_i}} = \frac{n_1\cos\theta_i - n_2\cos\theta_t}{n_1\cos\theta_i + n_2\cos\theta_t}, \tag{2.7}$$

$$t_s = \frac{E_{t,s}}{E_{i,s}} = \frac{2\sqrt{\varepsilon_1}\cos\theta_i}{\sqrt{\varepsilon_1}\cos\theta_i + \sqrt{\varepsilon_2 - \varepsilon_1\sin^2\theta_i}} = \frac{2n_1\cos\theta_i}{n_1\cos\theta_i + n_2\cos\theta_t}, \tag{2.8}$$

where the subscripts s and p indicate the s- and p-polarized component respectively.

The reflectivity R (transmissivity T) is defined as the ratio of the time averaged z-component of the Poynting vector of the reflected (transmitted) beam to that of the incident beam. The Poynting vector component of the corresponding wave normal to the boundary is given by [18]

$$\bar{S}_z = \frac{c\sqrt{\varepsilon_{1(2)}}}{8\pi} |E_{\alpha,\beta}|^2 \cos\theta_\alpha, \tag{2.9}$$

where c is the light speed in vacuum, the subscripts $\alpha = i, r, t$, and $\beta = s, p$. If both media are non-absorbing, the reflectivity and the transmissivity are

$$R_{s,p} = |r_{s,p}|^2 , \tag{2.10}$$

$$T_{s,p} = \frac{n_2 \cos\theta_t}{n_1 \cos\theta_i} |t_{s,p}|^2 . \tag{2.11}$$

Additionally, if the beam is at near-normal incidence to the interface ($\theta_i = \theta_r \approx 0$), the reflectivity and the transmissivity are given by:

$$R_s = R_p = \left(\frac{n_1 - n_2}{n_1 + n_2}\right)^2 , \tag{2.12}$$

$$T_s = T_p = \frac{4n_1 n_2}{(n_1 + n_2)^2}. \tag{2.13}$$

When medium 2 is absorbing, n_2 is complex. The reflectivity and the transmissivity are

$$R_{s,p} = r_{s,p} \cdot r^*_{s,p}, \tag{2.14}$$

$$T_{s,p} = \frac{n_2 \cos\theta_t}{n_1 \cos\theta_i} t_{s,p} \cdot t^*_{s,p}. \tag{2.15}$$

2.2.2 Three Phase System-Thin Film Optics

In practice, we usually deal with a three phase system at least, for example, thin film deposited on a solid surface, and adsorbed species on a film etc. The case of a thin film located at the interface of two semi-infinite media is shown in Fig. 2.4. The equivalent Fresnel reflection and transmission coefficients are defined in analogy to the two-phase system. The Fresnel reflection coefficient can be written for both s- and p-polarization as

$$r_{123} = \frac{r_{12} + r_{23} e^{-2i\beta}}{1 + r_{12} r_{23} e^{-2i\beta}}, \tag{2.16}$$

while the Fresnel transmission coefficients are give in the form :

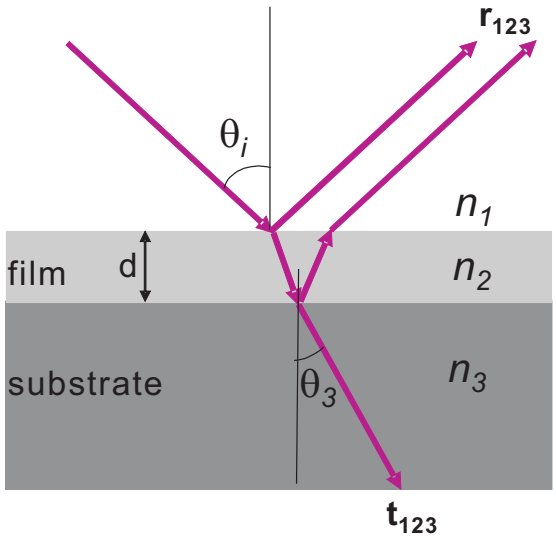

Figure 2.4: Transmission and reflection at the interfaces of a thin film located at the interface of two semi-infinite media. The film thickness is denoted by d. Generally medium 1 is air or vacuum.

$$t^p_{123} = \frac{t^p_{12} r^p_{23} e^{-i\beta}}{1 + r^p_{12} r^p_{23} e^{-2i\beta}}, \tag{2.17}$$

$$t^s_{123} = \frac{t^s_{12} t^s_{23} e^{-i\beta}}{1 + r^p_{12} r^p_{23} e^{-2i\beta}}, \tag{2.18}$$

where

$$\beta = 2\pi(\frac{d}{\lambda})\sqrt{\varepsilon_2 - \varepsilon_1 \sin\theta_1} \tag{2.19}$$

is the phase shift of the electromagnetic wave after one pass through the film, λ is the wavelength of light in vacuum, θ_1 is the angle of incidence, ε_1 and $\varepsilon_2 = \varepsilon_2' + i\varepsilon_2''$ are the dielectric functions of medium 1 (usually it is air or vacuum) and the film respectively.

In IR measurement, the thickness d of our metal film is much smaller than the wavelength λ of IR light, thus the so called *thin film approximation* can be used. Let $\exp(-2i\beta) \approx 1 - 2i\beta$, the Fresnel coefficients can be simplified to :

$$r_{123} = \frac{r_{12} + r_{23}(1 - 2i\beta)}{1 + r_{12} r_{23}(1 - 2i\beta)}, \tag{2.20}$$

$$t^p_{123} = \frac{t^p_{12} r^p_{23}(1 - 2i\beta)}{1 + r^p_{12} r^p_{23}(1 - 2i\beta)}, \tag{2.21}$$

$$t^s_{123} = \frac{t^s_{12} t^s_{23}(1 - 2i\beta)}{1 + r^p_{12} r^p_{23}(1 - 2i\beta)}. \tag{2.22}$$

Analogous to the two phase system, the reflectivity and the transmissivity for the three phase system are

$$R^{s,p}_{123} = |r_{123}|^2, \tag{2.23}$$

$$T^{s,p}_{123} = \frac{n_3 \cos\theta_3}{n_1 \cos\theta_i} |t^{s,p}_{123}|^2. \tag{2.24}$$

In the three phase system, the reflectivity and the transmissivity of a film free interface (R_{13} and T_{13}) are identical to that of a two phase system. Using Eq. 2.23 and Eq. 2.24 with $d = 0$, we can write the value of R_{13} and T_{13} as

$$R(d) = R_{123},\ R(0) = R_{13}, \tag{2.25}$$

$$T(d) = T_{123},\ T(0) = T_{13}. \tag{2.26}$$

In accordance with the measured spectra, we get expressions of relative reflectivity and transmissivity as [18, 15]

$$\left(\frac{R(d)}{R(0)}\right)_s \approx 1 - \frac{8\pi d n_1 \cos\theta_i}{\lambda} \mathrm{Im}\left\{\left(\frac{\varepsilon_3 - \varepsilon_2}{\varepsilon_1 - \varepsilon_3}\right)\right\}, \tag{2.27}$$

$$\left(\frac{R(d)}{R(0)}\right)_p \approx 1 - \frac{8\pi d n_1 \cos\theta_i}{\lambda} \mathrm{Im}\left\{\left(\frac{\varepsilon_3 - \varepsilon_2}{\varepsilon_1 - \varepsilon_3}\right)\left[\frac{1 - (\varepsilon_1/\varepsilon_2\varepsilon_3)(\varepsilon_3 + \varepsilon_2)\sin^2\theta_i}{1 - (1/\varepsilon_3)(\varepsilon_3 + \varepsilon_1)\sin^2\theta_i}\right]\right\}, \tag{2.28}$$

$$\left(\frac{T(d)}{T(0)}\right)_s \approx 1 - \frac{4\pi d}{\lambda n_1 \cos\theta_i} \mathrm{Im}(\varepsilon_2), \tag{2.29}$$

$$\left(\frac{T(d)}{T(0)}\right)_p \approx 1 - \frac{4\pi d}{\lambda} \mathrm{Im}\left[n_1^{-1} \mathrm{Im}(\varepsilon_2)\cos\theta_i + \mathrm{Im}(\frac{1}{\varepsilon_2})\frac{n_1^3 \sin^2\theta_i}{\cos\theta_i}\right], \tag{2.30}$$

where ε_3 is the dielectric function of the substrate. If the beam is at near-normal incidence to the interface ($\theta_i \approx 0$), the reflectivity and the transmissivity, which are independent of the polarization, are given by:

$$\left(\frac{R(d)}{R(0)}\right)_{s,p} \approx 1 - \frac{8\pi d n_1}{\lambda} \mathrm{Im}\left\{\left(\frac{\varepsilon_3 - \varepsilon_2}{\varepsilon_1 - \varepsilon_3}\right)\right\}, \tag{2.31}$$

$$\left(\frac{T(d)}{T(0)}\right)_{s,p} \approx 1 - \frac{4\pi d}{\lambda n_1}\mathrm{Im}(\varepsilon_2). \tag{2.32}$$

As can be seen from these two formulas, due to $d \ll \lambda$, the relative reflectance and transmittance of a film decrease with the increase of average film thickness. The IR relative spectra of thin metal films can be calculated by these formulas. In this work we use the commercial software SCOUT [19] for the calculation of measured relative transmission and reflection spectra. In the software, these formulas are applied, and multi-reflection at the interface was considered.

2.3 SEIRA effect

The infrared absorption intensity of molecules is remarkably enhanced when they adsorb on very thin metal films consisting of small islands. This phenomenon is called surface enhanced infrared absorption (SEIRA) effect which was first observed by Hartstein *et al.* in 1980s [8]. There have been extensive efforts over the past 20 years to explain the SEIRA (see Ref. [20] for a review). At least two mechanisms responsible for it have been accepted by many researchers. First, the incident photon interaction with metal surface enhances the electric field at the surface (electromagnetic mechanism). Second, there are chemical interactions between the molecule and the metal surface (chemical mechanism). There is general consensus that the majority of the enhancement is attributed to the electromagnetic effect [15, 21].

The local electric field enhancement can be roughly described by modeling an island-like metal film with oblate ellipsoids as shown in Fig. 2.5 [23, 22]. The incident IR radiation polarizes the metal particles and induces a dipole moment

$$p = \varepsilon_0 \alpha E, \tag{2.33}$$

where α is the plausibility of the metal island, ε_0 is the permittivity of free space in vacuum, and E is the amplitude of the incident radiation [23, 22]. The dipole produces an electric field around the metal island. Its amplitude is written as:

$$E_{\mathrm{local}} = \frac{2p}{4\pi\varepsilon_0 l^3}, \tag{2.34}$$

where l is the distance from the center of the metal island. The local electric field is stronger than the electric field of the incident radiation [23, 22]. The adsorbed molecules are excited by this local electric field. The oscillating dipole fields in the molecules induce additional dipole fields in the metal island, the polarization of the metal island is modulated at frequencies of the molecular vibrations. Refering to Eq. 2.2, the absorption of molecules are strongly enhanced. The enhanced absorption (SEIRA) can be observed in both s- and p-polarized IRRAS and in normal incident transmission spectra of an island film.

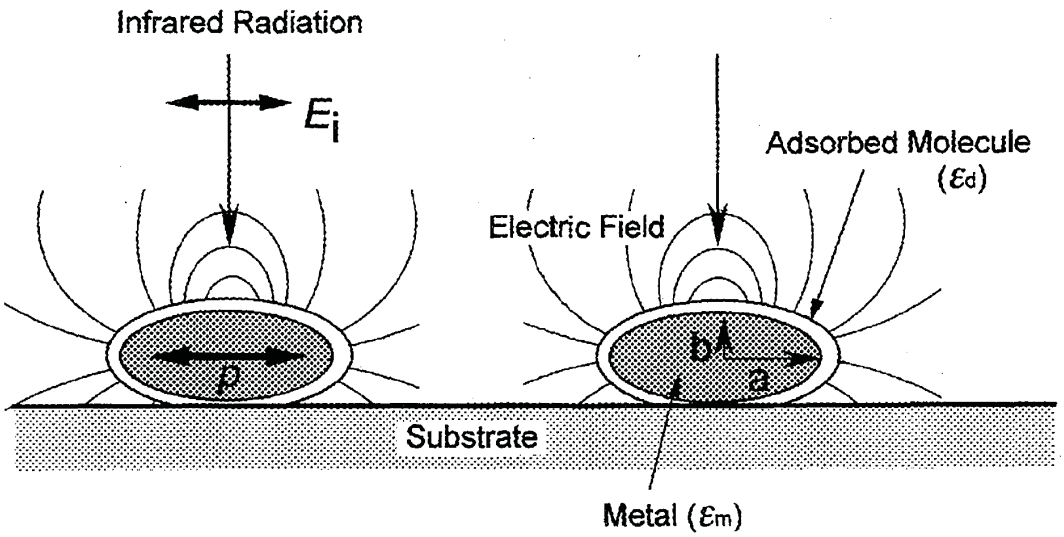

Figure 2.5: Polarization (p) of metal islands by the incident IR radiation and the electric field around the islands produced by the polarization. The islands are modeled by rotating ellipsoids with dielectric function of ε_{m} [22]. The adsorbed molecule is modeled by a thin layer with dielectric function of ε_{d} covering the ellipsoids. The aspect ratio of the ellipsoids is defined as $\eta = a/b$.

2.4 Drude Type Model

Optical characteristics of a free-electron metal can be properly described by the Drude model

$$\varepsilon = \varepsilon_\infty - \frac{\omega_p^2}{\omega^2 + i\omega\omega_\tau}, \tag{2.35}$$

where ω is the circular frequency of the external field, $\omega_\tau = 1/\tau$ is the relaxation rate, ε_∞ is the background polarizability, ω_{p} is the plasma frequency:

$$\omega_p = \sqrt{\frac{Ne^2}{\varepsilon_0 m^*}}, \tag{2.36}$$

where N is the free electron density, e is the electronic charge and m^* is the effective mass of an electron.

The complex dielectric function ε is related to the complex index of refraction n_c by the following equation

$$\varepsilon = \varepsilon_1 + i\varepsilon_2 = n_c^2 = (n + ik)^2. \tag{2.37}$$

By separating the real and the imaginary part of ε we get

$$\varepsilon_1 = \varepsilon_\infty - \frac{\omega_p^2}{\omega^2 + \omega_\tau^2}, \tag{2.38}$$

$$\varepsilon_2 = \frac{\omega_p^2 \omega_\tau}{\omega^3 + \omega \omega_\tau^2}. \tag{2.39}$$

The two Drude parameters ω_τ and ω_p can be obtained from optical data by solving Eq. 2.38 and Eq. 2.39:

$$\omega_\tau = \frac{\omega \cdot \varepsilon_2}{\varepsilon_\infty - \varepsilon_1}, \tag{2.40}$$

$$\omega_p = \sqrt{(\omega^2 + \omega_\tau^2)(\varepsilon_\infty - \varepsilon_1)}. \tag{2.41}$$

The dc conductivity $\sigma_0 = \frac{Ne^2}{m^* \omega_\tau}$ is related to ω_p and ω_τ by

$$\sigma_0 = \frac{1}{\rho_0} = \frac{Ne^2}{m^* \omega_\tau} = \frac{\varepsilon_0 \omega_p^2}{\omega_\tau}, \tag{2.42}$$

where ρ_0 is the resistivity.

2.5 Effective Medium Model (Bruggeman Model)

IR spectra of metal island films below the percolation threshold can not be described by a simple Drude-type model that needs at least one big conductive cluster. However, if the film structure meets the model assumptions, for example, when the film consists of metal particles that are randomly arranged on a quadratic surface lattice, the two-dimensional Bruggeman model can be applied to describe the dielectric function of such a system [24, 25]. The effective dielectric function ε_{eff} of such a system follows the relation

$$F \frac{\varepsilon_{\text{m}} - \varepsilon_{eff}}{\varepsilon_{\text{m}} + (D-1)\varepsilon_{eff}} = (F-1) \frac{\varepsilon_{\text{h}} - \varepsilon_{\text{eff}}}{\varepsilon_{\text{h}} + (D-1)\varepsilon_{\text{eff}}}, \tag{2.43}$$

Where ε_{h} is regarded as the dielectric constant of embedding host, ε_{m} as the dielectric constant of metal particles and it can be Drude like, F as the filling factor and D as the dimension (D=2, two dimensions; D=3, three dimensions). It is important to note, that ε_{eff} from Eq. 2.43 describes only the dielectric function for fields parallel to the film plane.

For the two dimensional case, Eq. 2.43 can be solved for ε_{eff}

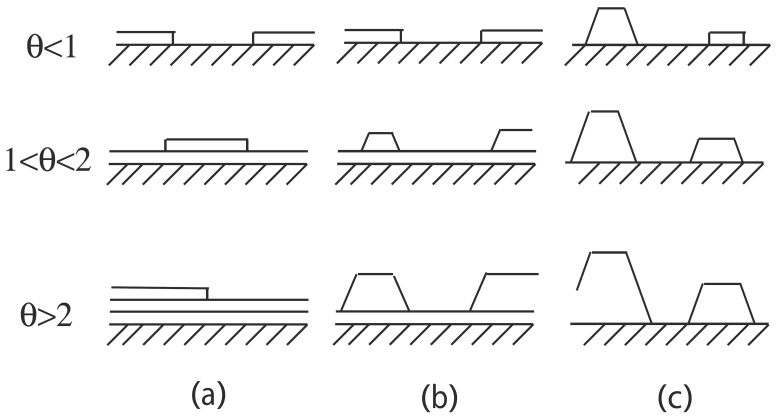

Figure 2.6: Schematic representation of the three growth modes of a growing film for different coverage Θ regimes (Θ is given in monolayers): (a) layer-by-layer growth mode (Frank-van der Merwe mode); (b) island growth mode (Stranski-Krastanov mode); (c) layer-by-layer plus island growth mode (Volmer-Weber mode) [26].

$$\varepsilon_{\text{eff}} = \frac{(1-2F)(\varepsilon_{\text{h}}-\varepsilon_{\text{m}}) \pm \sqrt{(2F-1)^2(\varepsilon_{\text{h}}-\varepsilon_{\text{m}})^2 + 4\varepsilon_{\text{h}}\varepsilon_{\text{m}}}}{2}, \tag{2.44}$$

where the sign of the square root has to be chosen to fulfill $\operatorname{Im}\varepsilon_{\text{eff}}>0$. Except for F in the vicinity of the critical filling F_c, which is $1/2$ in two dimensions, the negative sign of the root is valid.

2.6 Metal Film Growth

There is a strong connection between the growth mode and the film morphology. Various experimental and theoretic studies are focused on the growth mode, which usually falls into one of the three categories: Frank-van der Merwe mode, Stranski-Krastanov mode and Volmer-Weber mode as shown in Fig. 2.6. Frank-van der Merwe growth is defined by the sequential filling of the layers. The growth of the $(n+1)$th layer starts only after the nth layer has been completed. Therefore it is also called layer-by-layer growth. Volmer-Weber growth is defined by the growth of three-dimensional islands on the substrate. Stranski-Krastanov growth is encountered for systems that initially grow in a layer-by-layer fashion but then develop three-dimensional islands above a certain thickness. It is simply called a layer-by-layer plus island mode.

Normally an ultrathin metal film grown by physical vapor deposition onto a step free substrate evolves in several stages. In the beginning, atoms from vapor source arrive at the substrate surface and migrate on it until one of the processes described below occurs. These processes, as it is shown in Fig. 2.7, include reevaporation into the

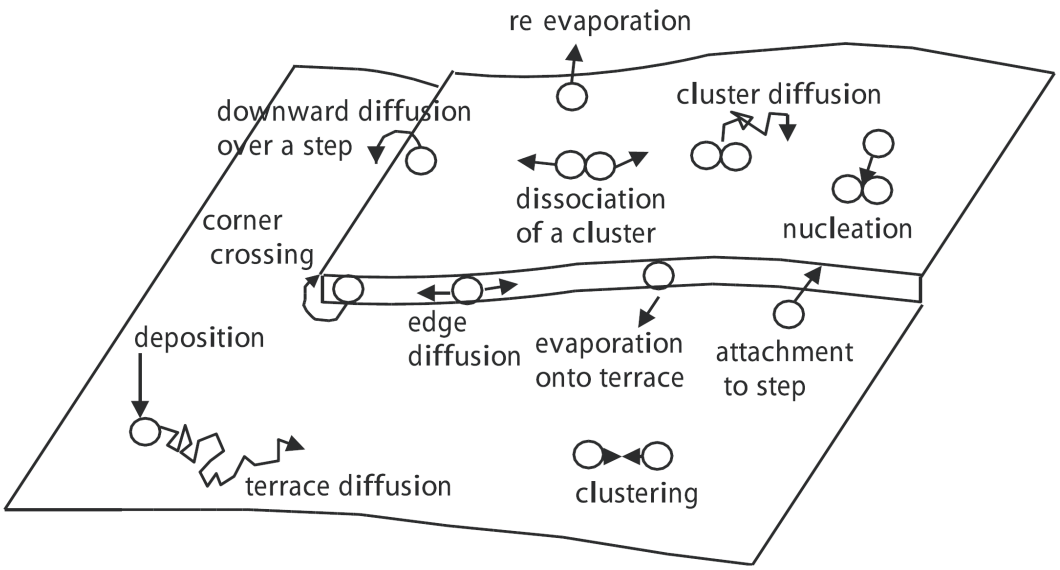

Figure 2.7: Sketch of elementary atomistic processes in nucleation and growth on a substrate [2].

vacuum, capture by existing steps and clusters, and nucleation into clusters. The atoms on the substrate surface are then called adatoms. Following the evaporation the density of adatoms $n_1 = Rt_a$ increases and some steady clusters are formed, where R is the evaporation rate and t_a is the life time of an adatom (the time between its arrival and reevaporation). The steady clusters act as sink and capture the adatoms. Later on, after some time τ_c, which is called capture time, the density of adatoms starts to decrease. The total number of steady clusters n_x is defined as

$$n_x = \sum_{j=i+1}^{\infty} n_i$$

where i is the number of atoms in a cluster at the critical size. The cluster is subcritical when $j \leq i$, and the cluster is stable when $j > i$. The time dependence of the density of adatoms n_1 and steady clusters n_x is shown in Fig. 2.8. n_x keeps increasing until the coalescence of clusters dominates the growth. For a metal film grown on a non-wetting substrate surface, in a later stage, fully coalescence of clusters no longer occurs and elongated structures forms because of the partial coalescence of touched clusters. The elongated structures are ascribed to grain boundaries and substrate defects. Generally, nucleation dominates the early stages and growth does in the later stages of film formation.

The diffusion coefficient D of adatoms on a square surface lattice has the form of:

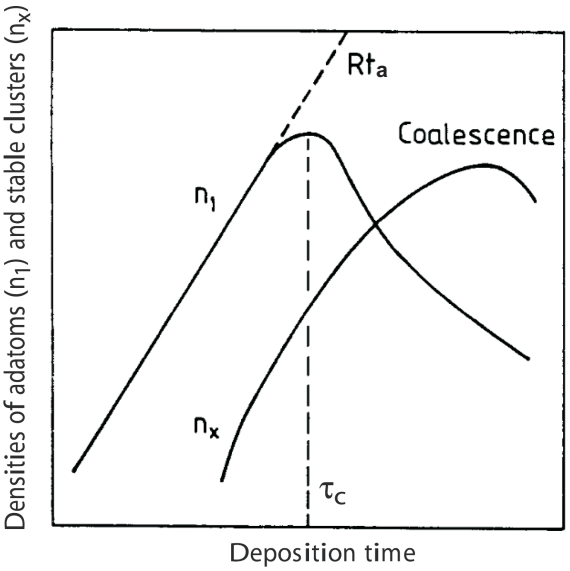

Figure 2.8: Development of the density of single adatoms n_1 ($n_1 = Rt_a$, t_a is the lifetime of an adatom) and stable clusters n_x along the deposition time. Before capture time τ_c the density of adatoms increases linearly with deposition time. The number of steady clusters (n_x) also keep increase util the coalescence dominates the growth [2].

$$D = \frac{a^2}{4}\nu_0 \exp\left(-\frac{E_d}{k_B T}\right), \tag{2.45}$$

where a is the lattice constant of the square surface, ν_0 is a slightly temperature dependent pre-factor and can be safely taken as a constant, E_d is the diffusion barrier.

A set of kinetic equations have been developed by Zinsmeister, Logan, Frankl and Venables to quantitatively describe the nucleation and growth. Here we show a useful result from Venables *et al.* [2, 3]:

$$n_x = \frac{\sigma_i}{\sigma_x^{i+1}}\Theta^{1/(i+2)}\left(\frac{R}{D}\right)^{i/(i+2)} \exp\left\{E_i/\left[(i+2)\,k_B T\right]\right\}, \tag{2.46}$$

where σ is the capture number of a cluster, which describes the diffusional flow of single atoms to critical (σ_i) or stable (σ_x) clusters, R is the evaporation rate, $\Theta \approx \int R\,dt$ is the total coverage, E_i is the binding energy of i-atom cluster, $k_B = 1.380658 \times 10^{-23}\,\mathrm{J\cdot K^{-1}}$ is the Boltzmann constant, T is the temperature.

With Eq. 2.45, Eq. 2.46 can be written as

$$n_x = \frac{\sigma_i}{\sigma_x^{i+1}}\Theta^{1/(i+2)}\,(R)^{i/(i+2)} \exp\left\{(E_i + i\cdot E_d)/\left[(i+2)\,k_B T\right]\right\}. \tag{2.47}$$

For Ag grown on the MgO(001), the energy barrier E_d for the Ag adatom diffusion on MgO(001) is very small (≈0.05 eV) along the <110> direction but higher along the <100> direction (≈0.12 eV) [27]. At submonolayer coverage, the Ag adhesion energy for binding to O sites on the MgO(001) surface lies between 0.18 eV (monolayer coverage) and 0.26 eV (below monolayer coverage) per adatom [27].

For Cu films grown on MgO(001), the energy barrier E_d for the Cu adatoms jumping between neighboring binding sites is 0.45 eV at room temperature [28, 29]. The adhesion energy of a Cu adatom binding onto O sites on the MgO(001) surface ranges from 0.2 to 1.4 eV [30, 28] depending on different calculation methods and onto Mg sites in the range of 0.2 eV [30, 31, 32]. V. Musolino *et al.* reported an 0.99 eV adhesion energy together with the 0.45 eV energy barrier shown above.

2.7 MgO, Ag and Cu

2.7.1 MgO

Magnesium oxide (MgO) is an ionic material, crystallizing in the rock-salt structure and cleaving on (100) and (111) planes. High physical strength and stability, a melting point near 2852 °C, and excellent optical transparency throughout the range of 0.25 to 6.8 μm combine to make the material of considerable interest. Some physical properties of MgO are listed in table 2.1.

In this work, all the metal films are deposited on a MgO(001) surface, which is the most stable surface form of MgO without reconstruction and with only a small relaxation and rumpling. As introduced above, the IR spectra of layer-on-substrate system can be fitted either by a Drude type model or by an Effective Medium Model. The IR transmission or reflection spectrum of the bare MgO substrate is described by dielectric function data collected by David M. Roessler *et al.* [34]. The numerical calculations are performed with the commercial software SCOUT [19]. In Fig. 2.9 a calculated transmission spectrum of MgO(001) compared to a measured one at room temperature is shown. Although the calculated MgO spectrum does not fit the measured one very well, it will not affect the fit quality of Ag film spectra.

Table 2.1: Physical properties of MgO [33, 34].

Symbol	MgO	Transmission range	0.25... 6.5 μm
Molecular weight	40.32 u	Lattice spacing,a_0	0.4215 nm
Density (25°C)	3.576 g/cm^3	ε_∞(300 K)	3.01
Melting point	2852 °C	ε_0(295 K)	9.64
Crystal structure	cubic, NaCl type	ε_0(85 K)	9.44

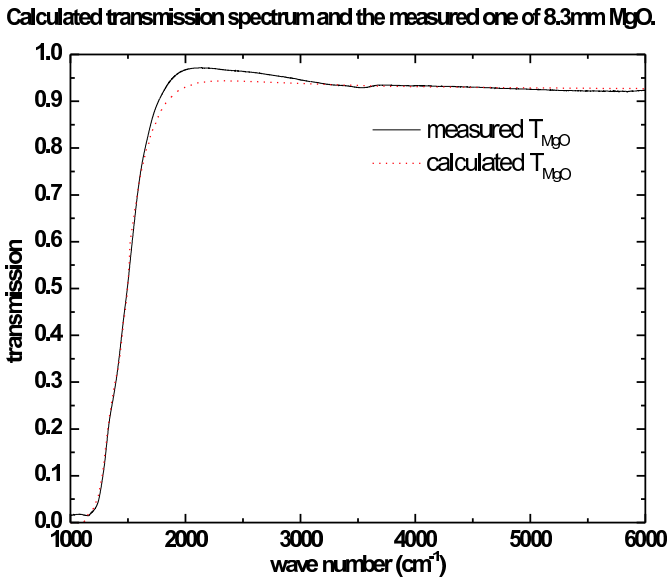

Figure 2.9: A calculated spectrum of MgO compared to a measured one at room temperature. The thickness of MgO is 8.3 mm.

2.7.2 Ag and Cu

Physical and Chemical Properties of Ag and Cu

In table 2.2, a list of physical and chemical properties of Ag [35, 36] and Cu [37] is given. It is easy to find more than one secondary source for many of the data in the table, and there are usually small (within one or two percent) disagreements among the various values for a given property. For Ag, where multiple values can be found, a representative (most frequently occurring) value was chosen for listing in this table [35].

Optical Properties of Bulk Ag and Cu

If the external excitation energy is too small to enable interband transitions, the optical properties of noble metals can be described by the Drude model. For both Cu and Ag studied in this work, the interband transition can be ignored in the range we are interested ($500\,\mathrm{cm}^{-1}$~$7000\,\mathrm{cm}^{-1}$). As shown in Fig. 2.10, the onset energy of the interband transition for Cu and Ag locates at 2 eV (about $16000\,\mathrm{cm}^{-1}$) and 4 eV (about $32000\,\mathrm{cm}^{-1}$) respectively.

The dielectric function of bulk Ag and Cu are all obtained from literature. There are two sets of Ag bulk data in the paper of Ordal[38]. One is measured by H. -J. Hagemann *et al.* [39] and another is measured by H. E. Bennett *et al.*[40]. The data of Hagemann kept the weak frequency dependence of reflection and that of Bennett took a linear approximation. Because of this reason we take the data from Hagemann for our spectral calculations later. The two Drude parameters, relaxation rate $\omega_{\tau\mathrm{b}}(\omega)$ and plasma frequency $\omega_{p\mathrm{b}}(\omega)$ were derived from both sets of bulk data using Eq. 2.40 and Eq. 2.41 and by setting ε_∞ to unity [38]. All these parameters were shown in

Table 2.2: Fundamental physical and chemical properties of Ag and Cu.

Properties	Silver, Ag	Copper, Cu
Atomic number,Z	47	29
Atomic mass, A	107.8682 u	63.546 u
Electronic structure	[Kr] $4d^{10}5s^1$	[Ar]$3d^{10}4s^1$
Crystal structure	face-centered cubic(fcc)	face-centered cubic(fcc)
Lattice spacing,a_0	0.4078 nm (20°C)	0.361 nm
Cohesive energy (25°C)	2.66 eV/atom, 285.8 kJ/mol	
Elec. resistivity	0.0147$\mu\Omega$·m (0°C)	0.0156$\mu\Omega$·m (0°C)
Melting point	961.93°C	1083.4°C
Density(20°C)	10.492g/cm^3	8.96g/cm^3
(0 K)	10.63g/cm^3	
Debye temperature	226.5 K (0 K)	
	215 K (20°C)	
Fermi energy	5.52 eV=8.84×10^{-19}J	7.0 eV
Fermi surface	Spherical, with necks at (111)	Spherical, with necks at (111)
Fermi velocity	1.39×10^6 m/s	1.57×10^6 m/s

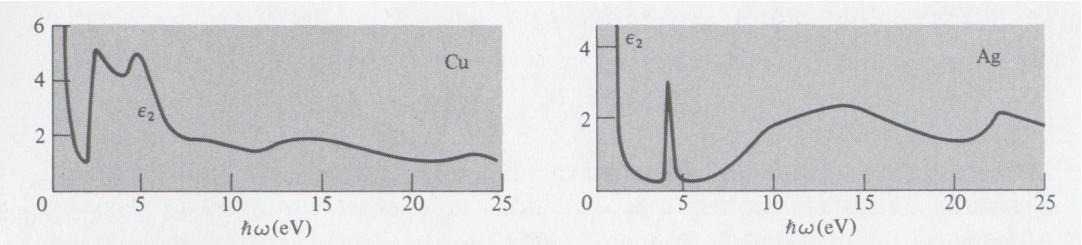

Figure 2.10: The imaginary part of dielectric constant, $\varepsilon_2(\omega) = \mathrm{Im}\varepsilon(\omega)$ vs. $\hbar\omega$, as deduced from reflectivity measurements(H. Ehrenreich and H. R. Phillip, *Phys. Rev.*128, 1622(1962).). Note the characteristic free electron behavior ($1/\omega^3$) below about 2 eV in copper and below about 4 eV in silver. The onset of interband absorption is quite apparent [36].

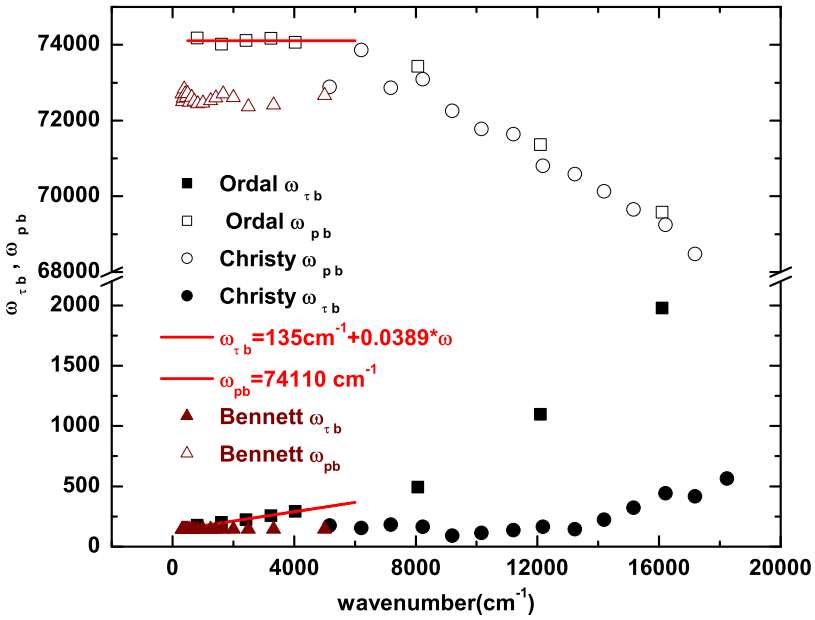

Figure 2.11: Drude parameters ω_{pb} and $\omega_{\tau\mathrm{b}}$ for Ag at 300 K calculated from different experimental bulk dielectric function data: Christy [41], Bennett and Ordal [38]. A background with $\varepsilon_\infty = 1$ is assumed [38]. The approximate relations in Eq. 2.48 are also shown as solid lines.

Fig. 2.11. Another set of bulk data measured by Christy *et al.*[41] was also plotted in the same figure for comparison.

In the data of Hagmann and in the range ($500\sim6000\,\mathrm{cm}^{-1}$) we are interested in, the plasma frequency is oscillating in a small range and the relaxation rate is nearly linear frequency dependent. We interpolate these two items approximately by the relations below in a range of $500\,\mathrm{cm}^{-1}$ to $6000\,\mathrm{cm}^{-1}$:

$$\omega_{\tau\mathrm{b}} = \omega_{\tau 0} + 0.0386 \cdot \omega = 135\,\mathrm{cm}^{-1} + 0.0386 \cdot \omega, \quad \omega_{pb} = 74110\ \mathrm{cm}^{-1} \tag{2.48}$$

With those two relations and using Eq. 2.38 and Eq. 2.39, we interpolated the dielectric function of Ag and plotted it in Fig. 2.12 together with the original measured data in literature.

The dielectric function shown in Eq. 2.48 is for Ag at about 300 K. According to our spectral calculations of Ag films prepared at low temperatures we need corresponding bulk Ag data. As shown in Eq. 2.42, the frequency independent part of the relaxation rate $\omega_{\tau 0}$ is related to the dc resistivity. Matthiessen's rule assumes that the total electrical resistivity is well approximated by summing two terms. The first is

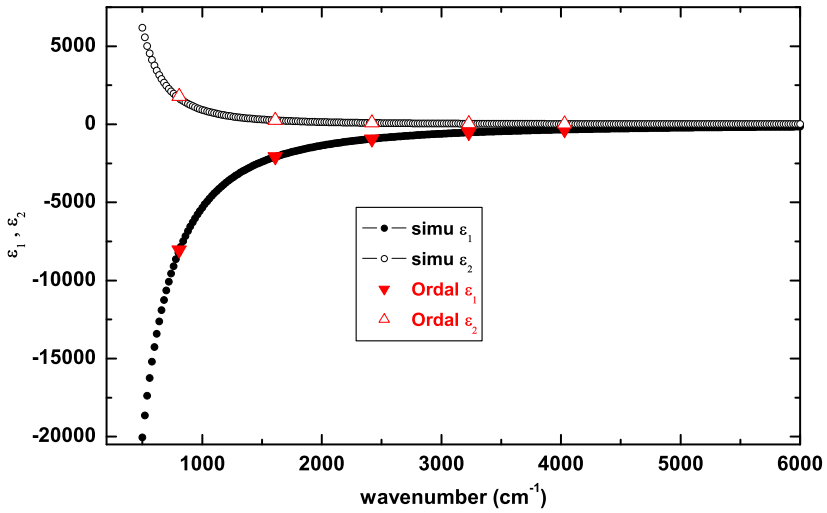

Figure 2.12: The simulated dielectric function compared to the original measured data for Ag by Ordal *et al.*

a temperature-dependent intrinsic term which is produced by thermal vibrations of the lattice and is zero at absolute zero. The second term is a residual term produced by static defects, and does not vanish at absolute zero. Above a certain temperature (for example 80 K [35, 42]) the second term is linearly proportional to the temperature. Therefore the relaxation rate changes linearly with the temperature too. With a relation measured by D. B. Tanner *et al.* [42] shown in Fig. 2.13, using Eq 2.42 and Eq. 2.42 we can estimate the $\omega_{\tau 0}$ at 60 K and 100 K:

$$\omega_{\tau 0-60\mathrm{K}} = 16.5\,\mathrm{cm}^{-1}, \quad \text{and} \quad \omega_{\tau 0-100\mathrm{K}} = 37.6\,\mathrm{cm}^{-1} \tag{2.49}$$

With the dielectric function of Ag and MgO mentioned above, using the commercial software SCOUT, we calculated the relative IR transmission spectra of Ag grown on MgO at room temperature, which are shown in Fig. 2.14.

The dielectric function for Cu measured by Ordal *et al.* [43] was used for our calculations and was plotted in Fig. 2.16. Using the same method as for silver we derived the two Drude parameters $\omega_{\tau \mathrm{b}}(\omega)$ and $\omega_{p\mathrm{b}}(\omega)$ for Cu (shown in Fig. 2.15) from the Ordal data shown in Fig. 2.16. In the mid-IR ($700\,\mathrm{cm}^{-1} \sim 5000\,\mathrm{cm}^{-1}$) the relaxation rate of Cu at 300 K can be expressed approximately by a relation as [44]:

$$\omega_{\tau \mathrm{b}} = 186 + (9.57 \times 10^{-2}) \cdot \omega. \tag{2.50}$$

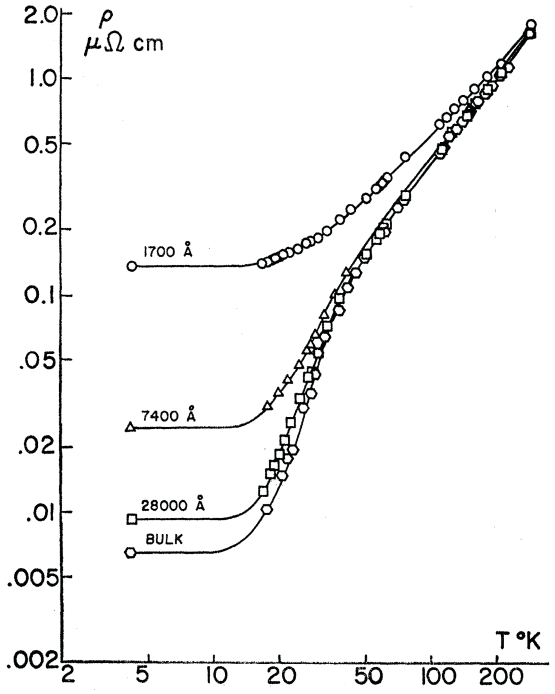

Figure 2.13: Total resistivity of Ag films and a bulk specimen as a function of temperature [42].

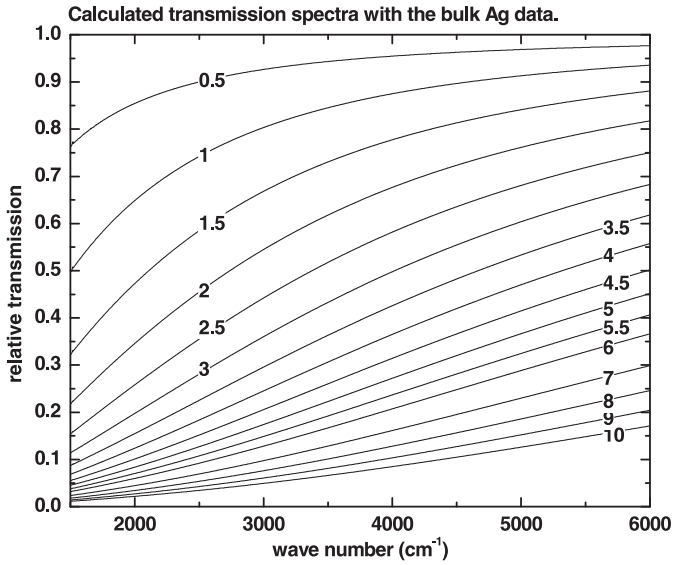

Figure 2.14: Calculated relative IR transmission spectra of Ag grown on MgO(001) at room temperature with bulk data. The numbers indicate the film thicknesses in nm.

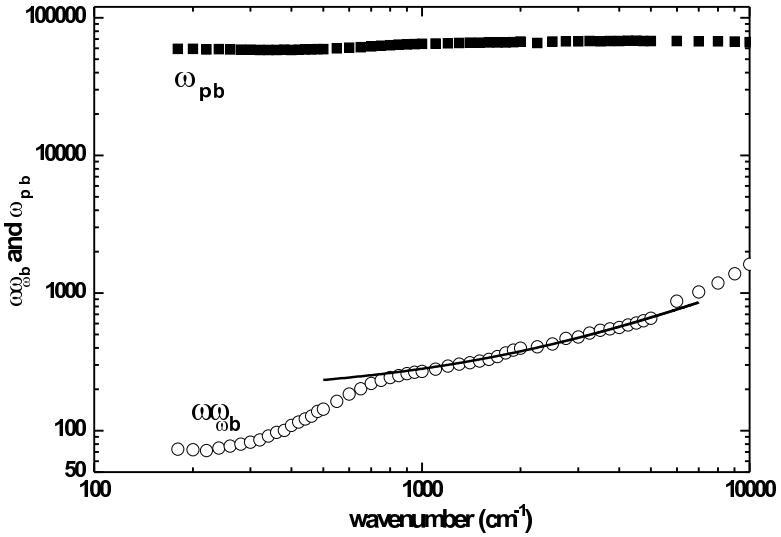

Figure 2.15: Drude parameters ω_{pb} and $\omega_{\tau \mathrm{b}}$ calculated from the experimental bulk dielectric function of Ordal [43] for Cu at 300 K. A background with $\varepsilon_{\infty} = 1$ is assumed. The approximate relation in Eq. 2.50 is shown as a solid line.

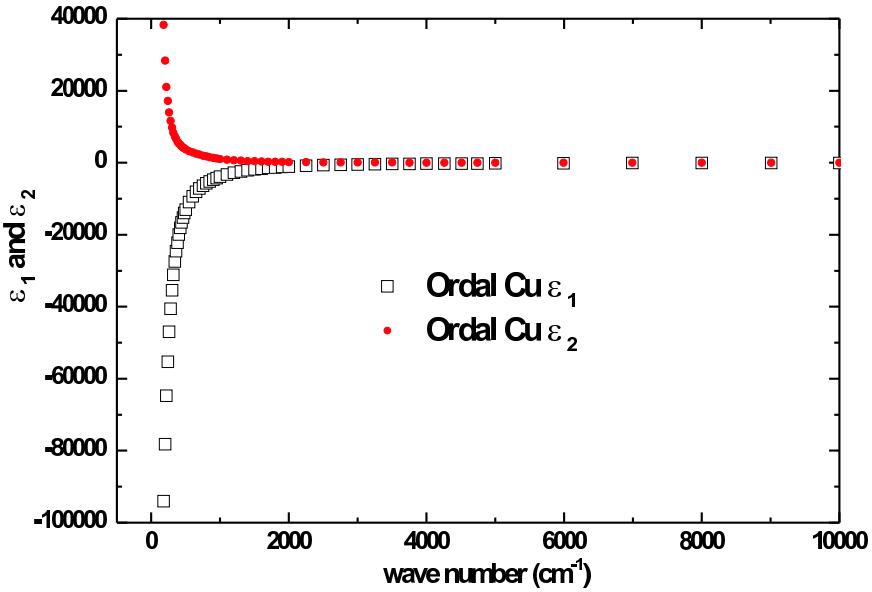

Figure 2.16: Dielectric function of bulk Cu from literature [38].

2.7.3 Optical Properties of Thin Films

The optical properties of conductive matter depend on the electronic structure, i.e., the relaxation of electrons close to the Fermi level and their effective mass. In thin films both quantities are different from their bulk values. First, additional relaxation mechanisms due to electron-interface scattering lead to the so called classical size effect (CSE). The CSE depends on the surface roughness and is influenced by adsorbates. Second, the confinement of electrons due to the interfaces changes the band structure and the density of states at Fermi level. This is called quantum size effect (QSE). Due to all these effects, when calculating the measured IR spectra, we take the frequency dependent dielectric function as we showed above and consider the additional electronic relaxation and depolarization effects induced by the irregular surfaces and interfaces of real thin films. We introduce an additional thickness d dependent relaxation rate $\omega_{\tau\mathrm{s}}$ to the bulk relaxation rate $\omega_{\tau\mathrm{b}}$ by

$$\omega_\tau = \omega_{\tau\mathrm{b}}(\omega) + \omega_{\tau\mathrm{s}}(d). \tag{2.51}$$

$\omega_{\tau s}(d)$ is an additional frequency independent contribution to the bulk relaxation rate which considers scattering from the surface, from the interface, and also from the defects in the volume of a film [44, 45].

We also take into consideration a thickness dependent variation $\beta(d)$ of bulk $\omega_{p\mathrm{b}}$ by

$$\omega_{p\mathrm{b}} = \beta(d)\omega_{p\mathrm{b}}(\omega) \tag{2.52}$$

With this frequency independent scaling factor $\beta(d)$ we may account for the quantum size effects and also for depolarization effects in films with non-flat surfaces.

The calculation is performed with the commercial software SCOUT that considers the multiple reflections in the film. $\omega_{\tau\mathrm{s}}(d)$ and $\beta(d)$ are used as fit parameters. Before we apply such a calculation to the spectra of metal films, the validity of local optics should be checked.

The relevant IR optical parameters of both Ag and Cu [44] at $2000\,\mathrm{cm}^{-1}$ are shown in table 2.3. At 300 K, the propagation length l_p of the electrons in an ac field is well below the penetration depth δ of the external field, which allows the use of local optics. Additionally, the fact that the average film thickness d$<\lambda_b$ ensures that we have a nearly homogeneous conductivity in Ag metal films.

A lot of valuable results were already obtained from IR studies of metal films (for example Fe and Cu etc.) grown on MgO(001) [45, 46, 47] or on KBr [48] concerning the effects of the substrate temperature and the existence of CO gas etc. [49]. The IR spectra of Fe and Cu films above the percolation threshold were theoretically calculated successfully using the commercial software SCOUT [19] by the Drude-type model described above. In this work we will show that the IR spectra of Ag and Cu films grown on MgO(001) are calculated successfully.

Table 2.3: IR optical parameters at $\omega = 2000\,\mathrm{cm}^{-1}$ and electronic parameters for silver and copper: plasma frequency $\omega_{p\mathrm{b}}$, relaxation rate $\omega_{\tau\mathrm{b}}$, Fermi velocity v_F , penetration depth δ of the external field, mean free path of the electrons λ_b, propagation length l_p of the electrons in an ac field. The temperature is 300 K.

parameter	unit	Ag	Cu
$\omega_{p\mathrm{b}}$	$[10^3\,\mathrm{cm}^{-1}]$	74.11	66
$\omega_{\tau\mathrm{b}}$	$[\mathrm{cm}^{-1}]$	212.2	377
v_F	$[10^6\,\mathrm{m/s}]$	1.39	1.13
$\delta = c/\omega_{p\mathrm{b}}$	[nm]	21.48	24.1
$\lambda_b = v_F/\omega_{\tau\mathrm{b}}$	[nm]	34.75	15.9
$l_p = v_F/\omega$	[nm]	3.69	3.0

2.8 Adsorption Theory and Adsorbate CO

2.8.1 Physisorption

Physisorption is a weak interaction characterized by the lack of a true chemical bond between adsorbate and surface, i.e. no electrons are shared. The physisorption interaction is conveniently divided into two parts: A strongly repulsive part at close distances and Van der Waals interactions at medium distances of a few angstroms.

When an atom or molecule approaches a surface, the electrons in the particle — due to quantum fluctuations — set up a dipole, which induces an image dipole in the polarizable solid. Since this image dipole has the opposite sign and is correlated with fluctuations in the particle, the resulting force is attractive. The interaction between them is an attractive potential $V(d)$ behaving as

$$V(d) \propto -\frac{C_v}{d^3}, \tag{2.53}$$

where d is the distance between the atom and the metal surface, C_v is called Van der Waals constant, which depends on the polarizability of the atom and the response of the metal. The interaction doesn't require a permanent dipole. Hence rare gas atoms such as Argon and Xenon may also physisorb on the surface.

When the distance between the atom and its image becomes smaller, the attraction between them can not continue because the electrons of the atom begin to interact strongly with the electrons of the surface. The kinetic energy of the electrons increases as they will have to orthogonalize to the localized electrons of the atom as a consequence of the Pauli principle. Some energy will be gained as the same electrons also become attracted to the positive nucleus. This may lead to chemisorption , but if the atom is a rare gas then repulsion dominates. An exponential function like [50]

$$V_R \propto e^{-d/\alpha}, \tag{2.54}$$

can give an approximate description of the potential in such a regime. So the summed potential is given by [50]

$$V(d) \cong C_R e^{-d/\alpha} - \frac{C_v}{d^3}. \tag{2.55}$$

This potential is very similar to the Lennard-Jones potential because physisorption is very similar to the molecular van der Waals interaction. The only difference is this potential can describe the repulsive part of the potential better.

2.8.2 Chemisorption

When adsorbate molecules strike the substrate surface, they may bind to some sites on the substrate by forming a surface chemical bond. This process is called chemisorption. The most important features of chemisorption are well captured by Newns-Anderson model [50], which successfully accounts for the main features of bonding when an adsorbate approaches the surface of a metal and its wave functions interact with those of a metal. In § 2.8.2.2 we only simply cite some qualitative outcome of this model with regard to a molecule adsorbed on a noble metal.

2.8.2.1 CO

CO is the favorite test molecule to surface scientists, as it is stable and shows a rich chemistry upon adsorption that is conveniently tracked by vibrational spectroscopy. In Fig. 2.17 a schematic diagram of the CO molecule orbitals is shown. Upon adsorption, the 5σ and the antibonding $2\pi^*$ orbitals will interact strongly with the metal orbitals as shown in Fig. 2.18.

2.8.2.2 CO Adsorbed on Noble Metals

When an atom or a molecule (which has a pair of bonding and antibonding states) adsorbs on simple metal surfaces like Na, Mg, or Al without d states, the electronic states of the adsorbate are broadened and shifted down in energy through the interaction with the broad metal sp states, as shown by a sketch in Fig. 2.19.

Noble metals (copper, silver, and gold) have broad sp bands and a fully filled d band. The d band is narrow (the less the overlap of electron orbitals the narrower the band is) and has a pronounced shape and orientation. In the periodic table from Cu down to Au ($3d$ to $5d$) the d band broadens since the orbitals get even larger and therefore the overlap increases. The center position of the d band also changes when going to the right side in the periodic table, as shown in Fig. 2.20 [50].

When an atom approaches to such a surface, its energy level, in addition to be broadening and shifting as in the case above, has a strong interaction with the d band in

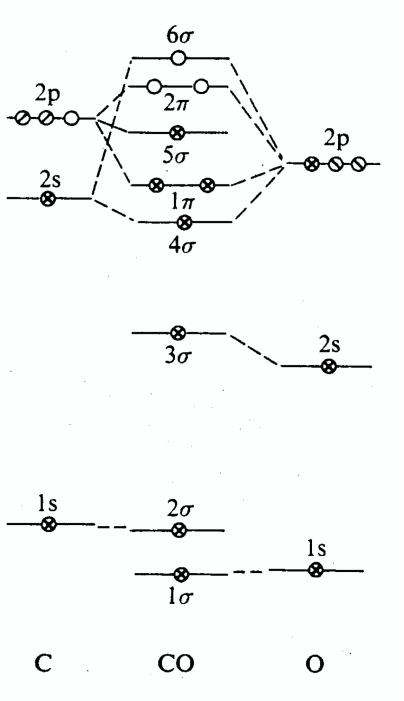

Figure 2.17: Schematic diagram of CO molecular orbitals [26].

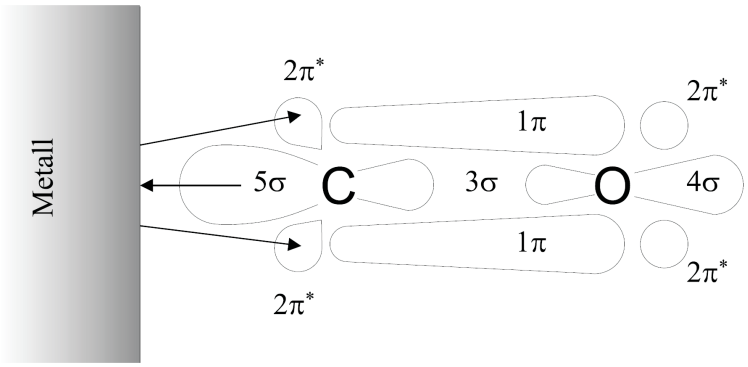

Figure 2.18: Sketch map of the interaction between a CO molecule and a metal surface [16].

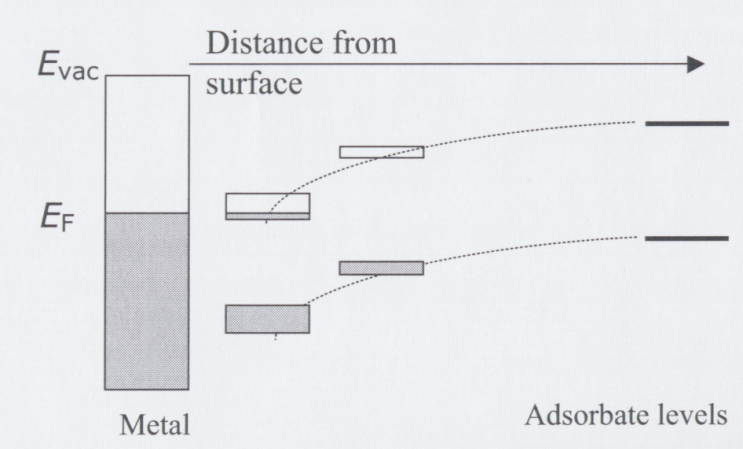

Figure 2.19: The energy levels of an adsorbate are broadened and lowered in energy when it approaches a free-electron metal surface with a broad *sp* band [50]. Note that the initially empty upper electron level of the adsorbate becomes filled when the bonding interaction shifts it below the Fermi level of the metal.

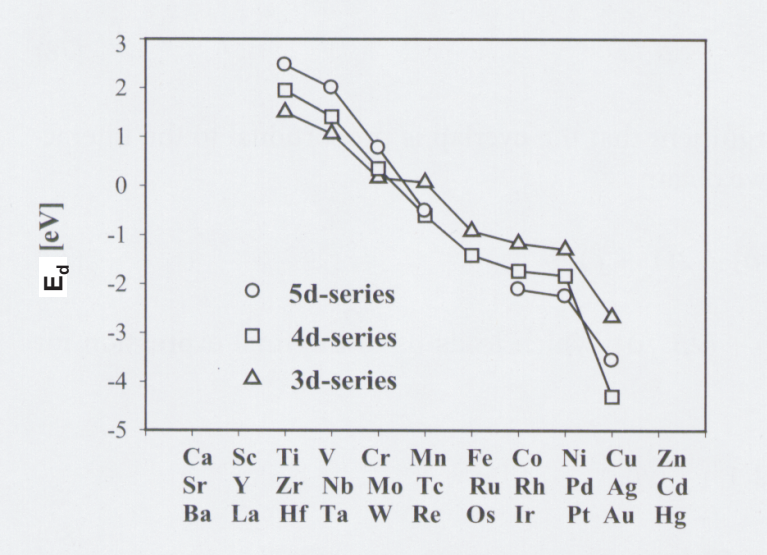

Figure 2.20: Position E_d of the center of *d* band for the three series of transition metals [50]. Note that the *d* band center shifts down towards the right side of the periodic table. When the *d* band is completely filled, it shifts further down and becomes a core level with little influence on the chemical behavior of the metal.

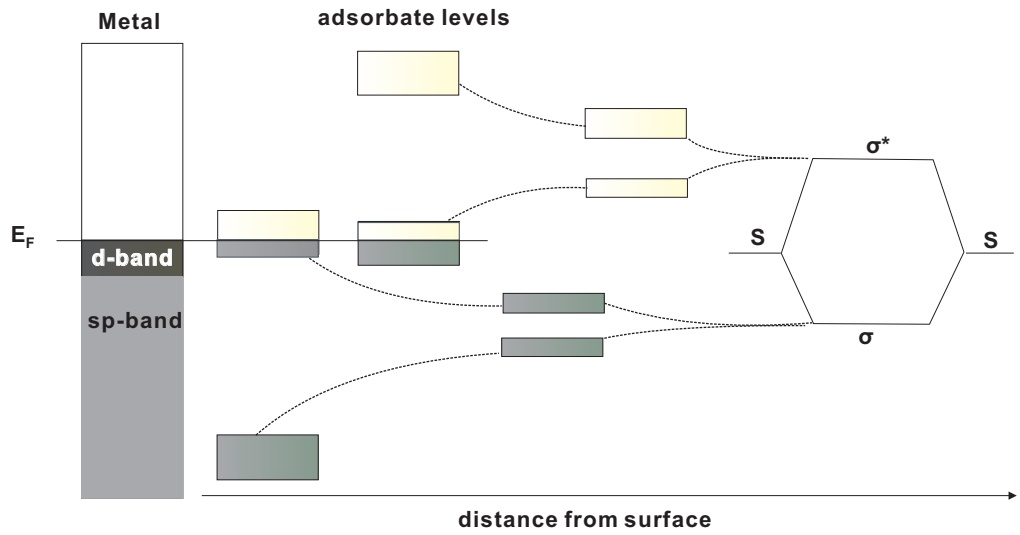

Figure 2.21: A molecule with a bonding σ and antibonding orbitals $\sigma*$ interacts with both the *sp* band and the narrow *d* band of the noble metal [50]. The former leads to the lowering and broadening of the bands of the molecule, while the latter results in splitting into bonding and antibonding orbitals. If there is back donation from metal to the antibonding orbital of the molecule, the internal bonding in the molecule will become weaker and maybe dissociate, but the bonding between the molecule and metal will become stronger.

the metal. Such an interaction leads the adsorbate energy level to a pair of bonding and antibonding chemisorption orbitals. When a molecule with a pair of bonding and antibonding states chemisorbed on a *d*-band metal surface, each state will follow the case of an atom interacting with *sp* and *d* bands. As shown in Fig. 2.21, if back donation from metal orbitals to the antibonding orbitals of molecules happens, the internal bonding in the molecule will become weaker and maybe dissociate. This is the key to understanding how a surface dissociates molecules.

For example, a full *d* orbital overlapping with the $2\pi^*$ antibonding orbital of carbon monoxide has the effect of weakening the carbon-oxygen bond compared with free carbon monoxide. The lattice mismatch between the metal film and the substrate induces strain or stress on the surface of the metal film. The strain or stress will either lead to narrower or broader *d* bands that are shifted up or down in energy, respectively. An upward shift leads to a stronger interaction with the adsorbed molecule thus to a stronger chemisorption bond. The same theory, allows us to understand why CO and similar molecules adsorb so much strongly on under-coordinated sites, such as steps and defects on surfaces. Since the surface atoms on these sites are missing neighbors they have less overlap and their *d* band will be narrower. Consequently, the *d* band shifts upwards leading to a strong bonding.

CO adsorbed on Ag surfaces is a good example. In this work, most of the studies about it are made at 100 K and some at 50 K. However, until now, rare reports about CO

adsorption on Ag films at about 100 K exist in literature. Many studies below 50 K have been reported. Here we cite some studies from literature.

CO was found giving a signal around 261±4 meV (2105±32 cm^{-1}) when adsorbed on a Ag (110) surface at 30 K [51] studied with electron energy loss spectroscopy (EELS). Another HREELS study [52] found CO physisorbed on a Ag(111) surface below 35 K shows a band at 265 meV (2137 cm^{-1}).

Studying with IR absorption spectroscopy P. Dumas *et al.* [9] found only physisorbed CO on Ag films prepared above 150 K, while on Ag films prepared below 150 K, both physisorbed and chemisorbed CO were observed. The thickness of the films was about 20 nm. The physisorbed CO molecules are oriented perpendicular to the metal surface. Films prepared below 150 K contain about 0.01 monolayer of 'chemically active sites' at which CO chemisorbs. At 2 K, on a 4 K prepared Ag film, the physisorbed band was found at 2143 cm^{-1} and the chemisorbed one at 2148 cm^{-1}. The band of chemisorbed CO shifts to lower frequencies with increased CO coverage. This down-shift arises from two effects: the partial filling of the CO $2\pi^*$ antibonding orbital on adsorption and the "self-image" effect caused by the electrostatic response of the metal. The chemisorbed CO desorbs from the surface at about 80 K.

With Raman spectroscopy, V. Klein *et al.* [53] found two CO peaks around 1998 cm^{-1} and 2070 cm^{-1} after a room-temperature prepared film was cooled down to 78 K in 2 Torr CO gas. On a Ag film prepared at low temperature they found one band at 2124 cm^{-1}appearing in the beginning, and another band at 2010 cm^{-1} appearing after 10 L exposure and growing in intensity through 10^5 L. The multiple lines maybe due to CO adsorbed on different surfaces of the polycrystalline sample, or adsorbed on different sites on the same surface. M. Moskovits *et al.* [12] with Raman spectroscopy also found one band at 2111 cm^{-1} when CO adsorbed on a cold-deposited Ag film at 11 K .

Also with Raman spectroscopy, at 17 K, on clean silver island films, A. Otto *et al.* [10, 11] found one band at 2119 cm^{-1} due to chemisorbed CO and another band at 2139 cm^{-1} due to physisorbed CO. The band due to physisorbed CO is very close to the frequency of the stretch vibration of condensed CO. The chemisorbed CO band arises from the atomic scale roughness, which is equivalent to the 'chemically active sites' from the study of P. Dumas *et al.* [9]. This band also shifts to low frequencies with increasing CO coverage. The desorption temperature for physisorbed CO is below 50 K and the desorption for the chemisorbed CO starts between 70 K and 100 K [11]. Because the CO molecule is both Raman active and IR active, the results from both kinds of studies can be compared to each other.

A. M. Bradshaw *et al.* [54] reported a band of CO adsorbed on cold-deposited Ag at 113 K at 2160 cm^{-1} by IR spectroscopy study.

A summary of all these studies done at low temperatures is:

1. on low-temperature (< 25 K) prepared films, a band due to chemisorbed CO appears at 2148 cm^{-1} in IR absorption spectroscopy and at 2119 cm^{-1} in Raman

spectroscopy, both of them shift to lower frequencies with increasing CO coverage because of the partial filling of the CO $2\pi^*$ antibonding orbital on adsorption and the "self-image" effect caused by the electrostatic response of the metal. Sometimes a band due to physisorbed CO appears on the same film at 2143 cm^{-1} in IR and at 2137 cm^{-1} in Raman spectroscopy, which is very close to the stretching frequency of condensed CO.

2. on Ag films prepared at room temperature only one band appearing at 2143 cm^{-1} in IR and at 2139 cm^{-1} in Raman due to physisorbed CO was found. HREELS studies ascribe it to the physisorbed CO on Ag(111) at 35 K.

In this work, with IR-spectroscopy, we find some coincidence with the studies from literature. The results of CO adsorbed on Ag surfaces at 100 K are quite new.

2.8.3 CO Adsorbed on MgO(001)

For all the film studies in this work we use MgO(001) single crystals as substrates. Some Ag films were cooled down to about 50 K with liquid Helium and exposed to CO gas. At about 50 K, CO can also adsorb on the cold MgO(001) surface. As a byproduct, we measured the stretching vibration of CO on MgO(001) for various cases, which will be shown in § 4.5.2. In Fig. 2.22 the thermal desorption spectra of CO adsorbed on UHV-cleaved MgO (100) measured by R. Wichtendahl *et al.* [55] are shown. The peak at 29 K is for desorption from multilayers of CO and the one at 57 K is for desorption from layers with small coverage. The low coverage adsorption energy for CO on MgO (100), which is about 0.14 eV, was also calculated [55].

A lot of studies were also made on the orientation [56] of CO molecules adsorbed on MgO(001) and the phase transition [57, 58] following the temperature etc. Above about 50 K, CO adsorbs on MgO(001) in a (1×1) structure [58], which is attributed to a lattice gas, in which the CO molecules randomly occupy on-top sites. With polarization infrared spectroscopy, above 45 K, only a single adsorption peak at about 2150 cm^{-1} is detected, which is attributed to CO dipoles oriented perpendicular to the surface attached to Mg^{2+} with the C end down [56]. Other infrared experiments [59] performed at 77 K for CO adsorbed on the MgO smoke, which consists of cubic microcrystals with nearly perfect (100) faces, also conclude that the CO adsorption was preferentially on the Mg site leading to a single narrow and intense peak at about 2148 cm^{-1}. In our studies, at about 50 K, on Ag films at low coverage (< 0.5 nm), a peak at 2138 cm^{-1} due to CO adsorbed on MgO(001) is often measured.

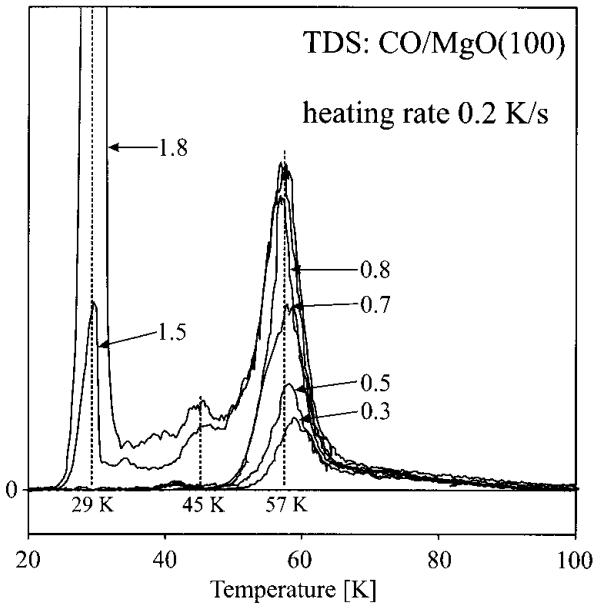

Figure 2.22: Thermal desorption spectra of CO on MgO (100) cleaved in UHV. CO doses are given relative to the dose needed for the preparation of a monolayer [55].

3 Experimental

3.1 Experimental Setup and Method

3.1.1 The UHV Chamber

A pressure as low as 1×10^{-10} mbar is reachable in our UHV chamber with an ion getter pump and a TSP (Titanium Sublimation Pump). When the ion getter pump and the TSP are replaced by a turbo molecular pump a pressure at 1×10^{-9} mbar is reachable. The FTIR spectrometer is kept in rough vacuum. When performing measurements in the UHV chamber the infrared light coming from the spectrometer is guided into the UHV chamber through a KBr window and the transmitted or reflected light is detected by a liquid nitrogen cooled MCT (Mercury/Cadmium/Telluride) detector at the opposite site of the chamber. Compared with DTGS (deuterated triglycine sulfate) detectors, the MCT photoconductive detector supports higher sensitivity and faster response time.

As shown in Fig. 3.1, most of the instruments we need in this work are indicated, for example, FTIR-spectrometer, metal evaporator, mass spectrometer, LEED, crystal cleaver, and polarizer etc. On the chamber we have two metal evaporators installed. One metal evaporator is drawn in the figure, another is installed at the position of "FC". When we prepare a metal film with the evaporator drawn in the figure, both transmission and reflection geometries are good to be applied to capture IR spectra. However,

Table 3.1: Full names of of the abbreviations in Fig. 3.1.

CC	Crystal Cleaver	M	Manipulator
Cr-E	Chromium Evaporator	ME	Metal evaporator
D1, D2, D3, D4	Detector positions	P	Polarizer holder
FC	Second evaporator	QMS	Mass spectrometer
GV	Plate valve	RO	Rotatable Optical Unit
IFS	FTIR-Spectrometer	S	Sample position
IG	Ion gauge	SP	Exit for vacuum
IGP	Ion getter pump	T	Transfer staff
IR-W	IR window	TMP	Turbo molecular pump
IS	Ion gun (Ar^+)	TSP	Titanium Sublimation Pump
LV	Gas dose valve	VP	View windows

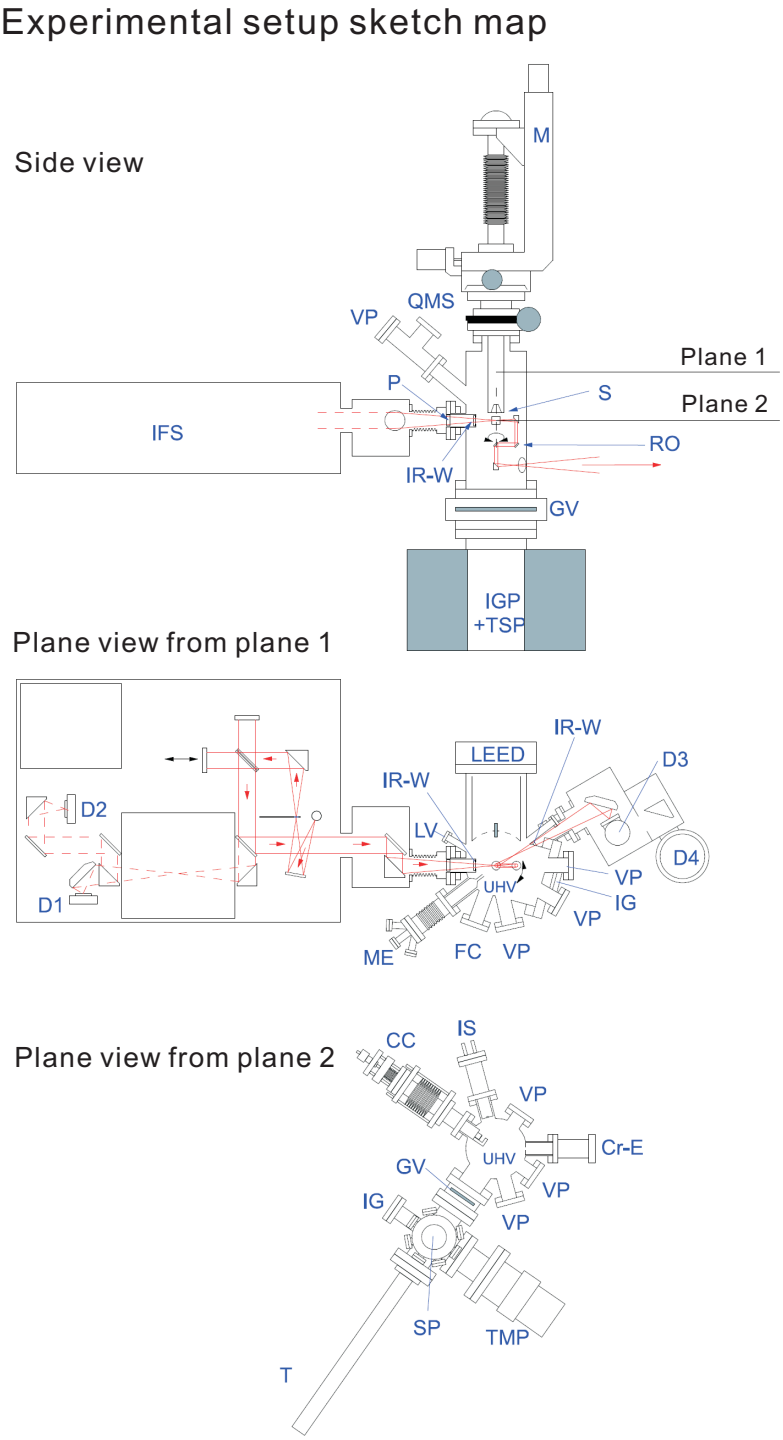

Figure 3.1: Sketch map of experimental setup for measuring IR spectroscopy of film growth and gas adsorption in UHV chamber. The picture in the middle shows the plan view from top till plane 1; the picture at the bottom shows the plan view from plane 2 till the bottom of the machine.[Adapted from [60]]

with the evaporator installed at "FC" position, a reflection geometry is preferable to avoid the effect of a large angle between metal flux and substrate surface normal.

In the UHV chamber, a sample temperature from 40 K to 1300 K can be accessed. The sample temperature was measured by a chromel-alumel thermocouple attached to the sample holder. For getting high temperatures we apply electronic bombardment to the sample holder. The manipulator can be filled with liquid N_2 or liquid He, so low temperatures can be obtained. The crystal cleaver allowed a fresh and defect free substrate surface (e.g. MgO) to be prepared in the UHV chamber. The mass spectrometer is for residual gas analysis and temperature programmed desorption spectroscopy is also possible with it.

Besides the gate valve above the ion getter pump, there is another one between the UHV chamber and the transfer system, so the transfer system can be vented or pumped separately without disturbing the UHV chamber, and the UHV chamber need not to be baked at every time a new sample is introduced.

3.1.2 FTIR Spectrometer

In a Fourier transform infrared (FTIR) spectrometer, the light source, interferometer and detector are the three main principle components. A schematic of a FTIR spectrometer incorporating a Michelson interferometer is shown in Fig. 3.2. The IR spectrometry is based upon optical interference between two beams. The incident light coming into the interferometer is divided into two components by a beam splitter, and a phase difference between the two beams is introduced by changing the optical path length traveled by the two beams. Optical interference is achieved by subsequent superposition of the two beams. The detector detects the summation of superposition of every wave component–a time domain spectroscopy (interferogram). If the wave number of one wave is ν, actually one source consisting of radiation spanning a large number of wavenumbers, the difference between wave components is $d\nu$, then the detected total intensity $I(p)$ is:

$$I(p) = \int_0^\infty I(p,\nu)d\nu = \int_0^\infty I(\nu)\left[1+\cos(2\pi\nu p)\right]d\nu, \tag{3.1}$$

where p stands for the difference in path length. Nevertheless what we want to get is $I(\nu)$, the variation of intensity with wave number. It is a simple work to get $I(\nu)$ by mathematically resolving the interferogram into its frequency components when there are only a few wave components. The work becomes very tedious when more wave components were included as a actual case. Fortunately, there is quite a simple and general way to solve this task, the Fourier transform (FT) process. Here is the expression of the FT of the interferogram:

$$I(\nu) = 4\int_0^\infty \left[I(p) - \frac{1}{2}I(0)\right]\cos(2\pi\nu p)dp. \tag{3.2}$$

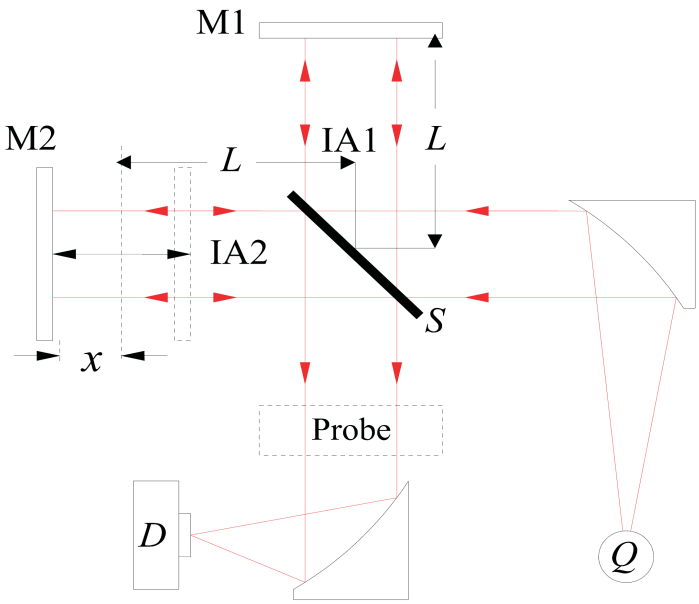

Figure 3.2: Schematic of an interferometer.The lines with arrows show the optical path in a Fourier transform spectrometer with Michelson interferometer in transmission geometry, (Q) light source, (D) detector, (S) beam splitter, (M1) stationary plane mirror, (M2) movable plane mirror offset.

This integration is usually performed by a computer that is the interface to the spectrometer and the output $I(\nu)$ is the absorption spectrum of the sample.

Compared to a conventional spectrometer in which a monochromator discards most of the radiation from the broadband IR source, the big advantage of a FTIR spectrometer is that all radiation is monitored continuously. Therefore, a FTIR spectrometer has a higher sensitivity than a conventional spectrometer. The resolution it can achieve is determined by the maximum path length difference, p_{max}, of the interferometer:

$$\triangle\nu = \frac{1}{2p_{max}}. \tag{3.3}$$

An evacuable (pressure = 3 mbar) FTIR spectrometer, *Bruker IFS 66v/S*, is equipped in our lab. As shown in Fig. 3.1, the IR light coming from a globar in the spectrometer can be inducted into the UHV chamber through a KBr window. Therefore measurements can be performed either in the spectrometer itself or in the UHV chamber.

3.1.3 How Relative Spectra are Measured

In IR spectroscopy studies a relative spectrum is often measured because of its high sensitivity and easy operation. In this work we mainly measure the changes on one

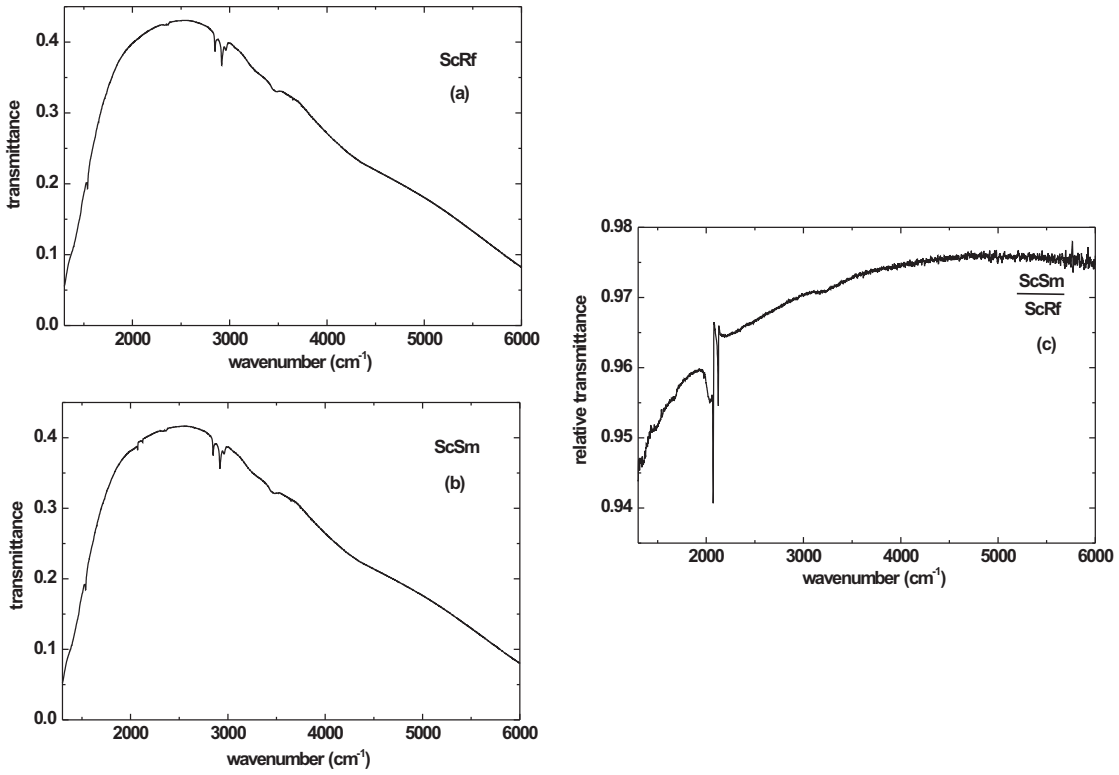

Figure 3.3: The procedure of measuring a relative transmission spectrum. The single channel spectrum of a film "ScRf" is shown in (a), that of the sample (the adsorbate and the film) "ScSm" is shown in (b), the relative transmission spectrum of the adsorbate is shown in (c).

surface due to metal deposition or gas adsorption. Relatively measuring is a convenient way to see small changes on the surface.

In Fig. 3.3 we show how a relative transmission spectrum is measured. First, we put the substrate into the optical path and measure a single channel spectrum "ScRf" as reference (see (a) in Fig. 3.3); second, after the sample is present on the substrate, another single channel spectrum "ScSm" is measured for the sample and substrate together (see (b) in Fig. 3.3); at last, the relative spectrum is achieved when dividing spectrum "ScSm" by spectrum "ScRf" (see (c) in Fig. 3.3), this work is done by computer. The same method is used when we measure a relative reflection spectrum.

The reference of a measured spectrum can be changed. We get out the single channel spectrum of sample and of the new substrate then divide former one by the later one, then a relative spectrum based on a new reference is derived. This method is very useful when we want to get information on the same sample in both transmission and reflection geometries. For example, during Ag film growth on MgO, reflection spectra

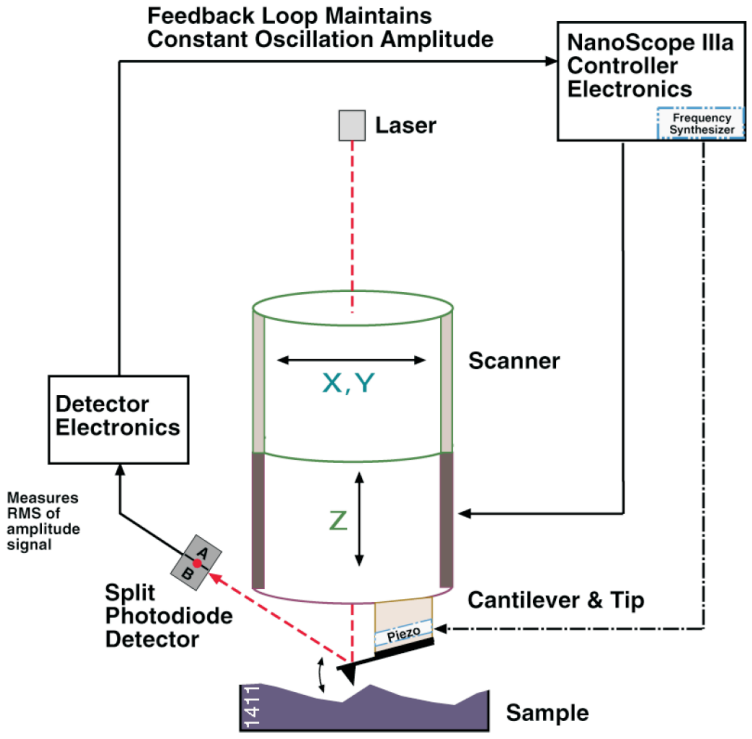

Figure 3.4: Tapping mode of Atomic Force Microscope.

were measured; then at the final thickness, we can measure a single channel spectrum of the Ag/MgO system in transmission geometry; at last we can use a pre-measured single channel spectrum of MgO to get the relative transmission spectrum of Ag at the final thickness. Thus we get the relative spectra of the Ag film at the final thickness in both geometries.

3.2 Atomic Force Microscopy (AFM)

Atomic force microscopy (AFM) or, as it is also called, scanning force microscopy (SFM) is based on the minute but detectable forces–of the order of nano Newtons– between a sharp tip and atoms on the surface. The tip is mounted on a flexible arm, called a cantilever, and is positioned at a subnanometer distance from the surface. If the sample is scanned under the tip in the $x - y$ plane, the tip feels the attractive or repulsive force from the surface atoms and hence it is deflected in the z-direction. The deflection can be measured with a laser and photo detectors as indicated schematically in Fig. 3.4. Atomic force microscopy can be applied in two ways.

In the contact mode, the tip is within a few angstroms above the surface, and the interaction is determined by the interactions between the individual atoms in the tip

and on the surfaces.

The second mode of operation is the non-contact mode, in which the distance between tip and sample is much larger, between 2 and 30 nm. In this case one describes the forces in terms of the macroscopic interactions between bodies.

A third mode, which has recently become a standard for work on surfaces that are easily damaged, is in essence a hybrid between contact and non-contact modes, and is sometimes called the tapping mode. In this case the cantilever is brought into oscillation such that the tip just touches the surface at the maximum deflection towards the sample. When the oscillating cantilever approaches the maximum deflection, it starts to feel the surface and the oscillation becomes damped, which is detected by the electronics and used as the basis for monitoring the topography when the sample is scanned. In tapping mode, shear forces due to dragging the tip horizontally along the surface ("scratching") are avoided, while forces in a perpendicular direction are greatly reduced. It has become the favorite way of imaging small particles on flat substrates.

3.3 Sample Preparation

3.3.1 MgO(001) Substrate Preparation

Fresh, clean and well-defined surfaces of brittle materials can be prepared in UHV by cleavage. This technique is derived from the classical method of preparing an alkali halide surface by cleaving the crystal with a razor individual or blade, and it is a simple and straightforward way. Surfaces prepared by this way usually contain defects such as steps which expose edge atoms that are in a different surrounding compared with those in the flat areas. Another important limitation applies to cleavage is that only brittle materials like alkali halides (NaCl, KCl, etc.), oxides (ZnO,TiO_2, SnO_2, etc.) and semiconductors can be studied in this way. Furthermore, cleavage is only possible along certain crystallographic directions which are determined by the geometry and nature of chemical bond. The number of covalent bonds being cut, or the compensation of electric fields within the cleavage plane in the case of ionic crystals are determining factors. Cubic alkali-halide crystals cleave along the {100} faces, which are nonpolar; i.e. they contain equal number of both types of ions such that the fields between the opposite charges can be compensated within the surface.

In our measurements, commercial MgO(100) crystals were cleaved just before the metal deposition with a stainless steel knife in the UHV chamber controlled by a mechanical feedthrough outside. If the MgO(001) is cleaved in air it will be transferred into high vacuum ($\sim 1\times10^{-7}$ mbar) within ten minutes and heated by two filaments for over night. It was heated again to about 700 K in the UHV chamber for about 3 hours at the day before metal deposition. Normally if the MgO(001) was cleaved in air, more defects will exist on the surface and will affect the film growth.

3.3.2 Metal Deposition

Our manipulator allows to changing the sample temperature in a wide range: about 50 K∼1200 K. The high temperature was gained by electron bombardment and the cryogenic temperature is obtained by liquid Nitrogen or liquid Helium. When the substrate is brought to the intended temperature we deposit a defined quantity of metal onto the surface. The metal source was put in a tungsten crucible and was heated by a EFM3/4 evaporator. The evaporation rate was calibrated with a quartz microbalance just before and after the evaporation. Since ultrathin metal films are transparent in the IR range, IR transmission measurements can be in situ performed during the film growth in a large thickness range. Oblique incident reflection measurements in the UHV chamber are available with an incident angle in the range of 75° to ∼82°.

For the Ag films grown on MgO(001) at different temperatures, the sticking probability of Ag on MgO(001) should be considered. The sticking coefficient of Ag on MgO at room temperature has been determined by J. H. Larsen [61] and M.-H. Schaffner *et al.* [62] and different results are given. J. H. Larsen *et al.* reported sticking probabilities ranging from 0.94 to unity as a function of Ag coverage; whereas M.-H. Schaffner *et al.* only get a sticking probability of 0.6. Because the sticking probability determined by M. -H. Schaffner *et al.* at 500 K is not in accord with our measurements at various temperatures, we assume a sticking probability near to unity as J. H. Larsen *et al.* reported for Ag grown on MgO(001) at room temperature. Without considering the sticking probability, the error of thickness in our measurements is already about 10%. Thus at higher Ag coverage the thickness error due to sticking probability can be neglected.

Metal ions from the beam source may produce some defects on the deposited film. We can take away the ions by putting a piece of magnet at the outside of the evaporator to change the trajectory of ions. In Fig. 4.17 (A) we show the spectra of a such a film, during its preparation the ions from the beam source were taken away.

3.4 Gas Exposure

As mentioned above, we expose CO (purity 99.997 vol.%) or N_2 (purity 99.999 vol.%) gas to Ag or Cu film surfaces as they were prepared and cooled down to low temperatures. These two kinds of gases might adsorb on the metal surface only at low temperatures which could be reached with liquid Nitrogen or liquid Helium. During gas exposure, IR relative transmission or reflection spectra can be measured *in situ* and normally SEIRA effect can be observed. The impurity in the gas can be checked with a mass spectrometer (Smart IQ).

4 Experimental Results and Analysis I: Ag Films Grown on MgO(001)

The Ag/MgO(001) system has been chosen as a model metal/ceramic interface because the number of effects intervening in adhesion is reduced to a minimum: the lattice mismatch is small (3%), with cube-on-cube epitaxy, and the species are nonreactive. Large numbers of theoretical studies [61, 63, 64] focus on the adsorption properties of Ag on MgO(001) at low coverage and give valuable information for experimental work. David Fuks *et al.* predict high mobility of adsorbed Ag atoms on MgO even at low temperatures which aids their aggregation, so 3D islands formation is unavoidable [65]. Layer-by-layer growth mode is possible at very high temperatures. From Eq. 2.46 we can also learn that the substrate temperature plays an important role on the film growth. Studied by X-ray scattering, a cube-on-cube epitaxy growth with respect to the MgO(001) substrate was reported in detail by O. Robach *et al.* and they found that the ordered interface dislocation network was oriented to MgO <110> direction [66]. In this work, an epitaxial distribution of islands is observed on a Ag film grown at 500 K on MgO(001). Besides the substrate temperature, the film growth can also be affected by a lot of other factors, such as the base pressure, surfactant, and evaporation rate etc. Also films at different thicknesses show different morphologies. Yuji Nishikawa *et al.* have reported the effects of such factors on Ag-film morphologies grown on BaF_2 in a vacuum chamber by showing SEM images [67]. In this chapter we will show the effect of substrate temperature, base pressure, CO and N_2 gas exposure etc. on the Ag film growth on MgO(001) studied by IR spectroscopy and AFM. Different surface morphologies for different Ag-film thicknesses will be presented too.

As discussed above, films that consist of small islands can give a SEIRA effect for adsorbates. In this chapter the SEIRA spectra of CO adsorbed on many kinds of Ag films at low temperatures will be shown.

4.1 Ag Films Prepared at Room Temperature

Table 4.1 provides a list of experiments of which the important results are shown in this section.

Table 4.1: List of experiments performed at room temperature. "d" denotes the average film thickness; "rate" denotes the evaporation rate; "geometry" means the measurement in transmission (T) or in reflection (R) geometry.

	Substrate temperature	Pressure during deposition	Deposition	final thickness	IR Spectroscopy	CO exposure		
Exp	T (K)	P (10^{-10} mbar)	rate (nm/min)	d (nm)	geometry	T (K)	P_{co} (10^{-8}mbar)	geometry
meng5	300	510	0.122	10.1	T			
ds3	298	1.3	0.1	12.2	T	93	4.3	T
ds4	301	9.1∼7.2	0.096	9.5	T			
mag1	299	8.7∼9	0.13	6.4	T	95	8	T
mag3	300	7.5∼8.2	0.115	5.3	T	95	8.1	T
mag4	298	4.4	0.114	3.4	T	98	8	T
mag6	302	2.6∼3.4	0.133	11.1	R	100	8	R
mag7	297	400 (CO)	0.118	5.2	T	100	6	T
mag8	301	2.4	0.143	6	R	98	6	R&T
mag9	296	2	0.134	3.9	T			
mag11	294	1.2	0.145	3.6	R	90	5	T
mag13	300	1.8	0.159	5.4	R	93	5	T
mag20	296	7.9	0.111	14.6	R	93	5	R
mag21	298	400 (N_2)	0.13	5.2	T			
meng19	300	2	0.134	7.6	R			

4.1.1 IR Transmission Spectra of Ag Films Grown on MgO(001)

In Fig. 4.1 (A) we show IR relative transmission spectra of four Ag films grown on UHV cleaved MgO(001) at room temperature. The multi-phonon absorption edge of MgO causes the low frequency limit of the spectral range. The spectra from different experiments are almost superposable at corresponding average film thicknesses, which means that our measurements are reproducible. The small discrepancy of the average film thickness between each film is within the thickness error range of our measurement. In each figure a decrease of transmittance with an increase of the average film thickness is obviously found. However, the shape of the spectrum changes with the increasing Ag coverage. Spectra at lower thicknesses show a negative slope with the circular frequency ω. This corresponds to the properties of metal particles embedded in a non-metallic matrix. At higher thicknesses, the spectra show a positive slope corresponding to Drude-type conductivity. At a certain thickness an optic crossover is observed, which is attributed to the percolation threshold [68]. At the percolation threshold the transmittance is almost frequency independent, which is a well-known fact.

Another interesting finding is that, at low Ag coverage, the relative transmission is more than one hundred percent for frequencies near the MgO multi-phonon edge. This effect is a shift of the substrate absorption edge towards lower wave numbers caused by the anti-reflecting effects of a certain array of small metal islands. Since the weak substrate absorption plays a role for the effect, as we know from studies on other substrates (e.g. CaF_2), advanced theoretical work is necessary for a detailed explanation. Until now, such photonic effects are only studied on transparent substrates.

In Fig. 4.1 (B) we show the AFM images of these four films. Since the Ag-film growth experiments at room temperature are reproducible (as can be seen from the IR spectra in (A)), their AFM images should be varied only by the thickness. As we can see from (1) to (4), the average film thickness increases, and we get bigger and bigger structures, finally we get smooth films with smaller and smaller shallow holes. Comparing (1) and (2), we can see the sinuous-structured islands prefer to connect end by end. The increased Ag coverage contributes to the growth in width and height of the islands, but the distance between the islands does not become smaller. The surface morphologies shown by image (1) and (2) correspond to the vicinity of the percolation threshold and those in image (3) and (4) correspond to thick films. As that will be discussed in § 4.5, on Ag films shown by image (3) and (4) we can not get CO adsorbate signals by measuring in normal transmission geometry, but on films like the ones in image (1) and (2) strongly enhanced CO signals were observed by measuring in both transmission and reflection geometries.

In Fig. 4.2 (A), IR spectra of sample No.ds3 are shown together with the ones of film No. ds4 . Their spectra show a better superposition than those shown in Fig. 4.1 (A). There is almost no discrepancy on the corresponding thicknesses. The AFM image of this film is shown in (B). Because sample No.ds3 is thicker than sample No.ds4, we

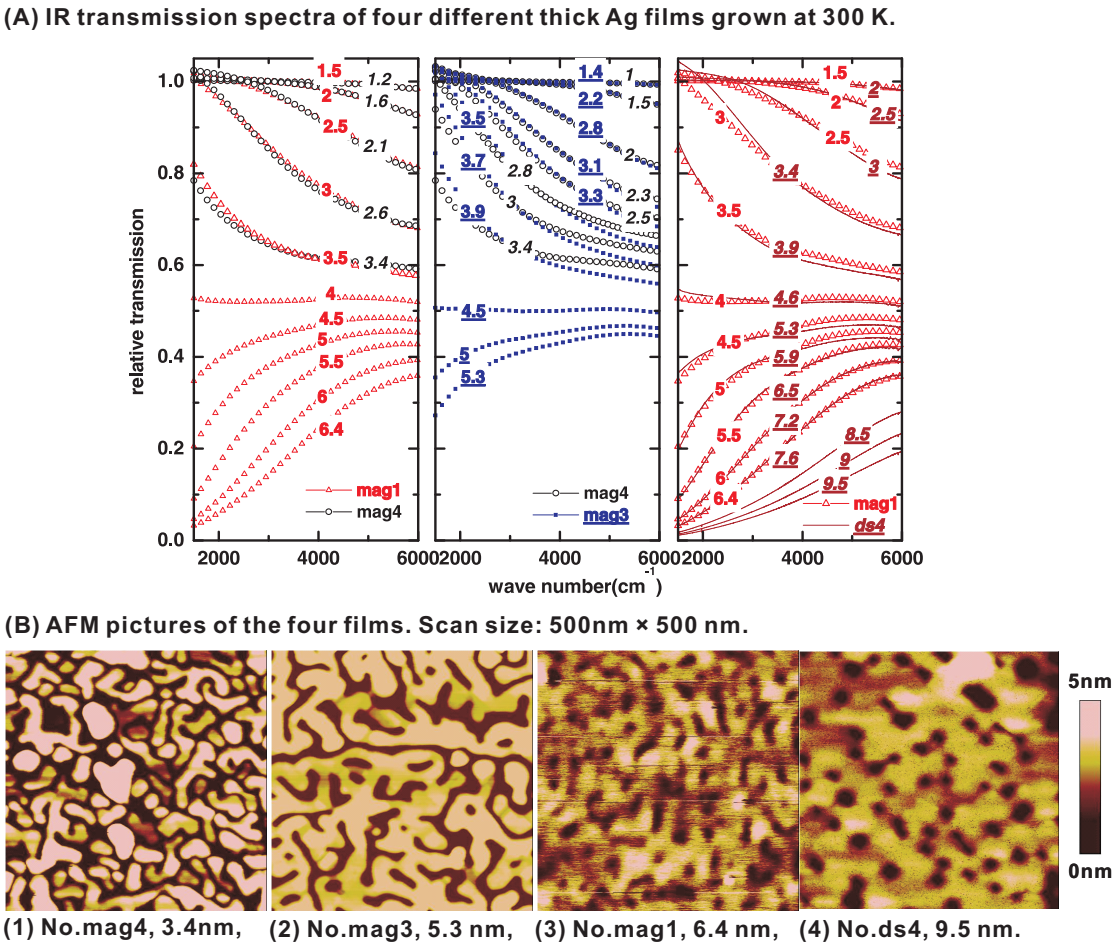

Figure 4.1: (A) Selected relative transmission spectra of four Ag films grown on UHV cleaved MgO(001) surfaces at room temperature. The spectra of different films are shown as different symbolic lines and also their thicknesses are given in different kinds of fonts or styles. These four films were prepared at similar conditions and only the final thickness of each film is different. (B) The AFM images of the four films.

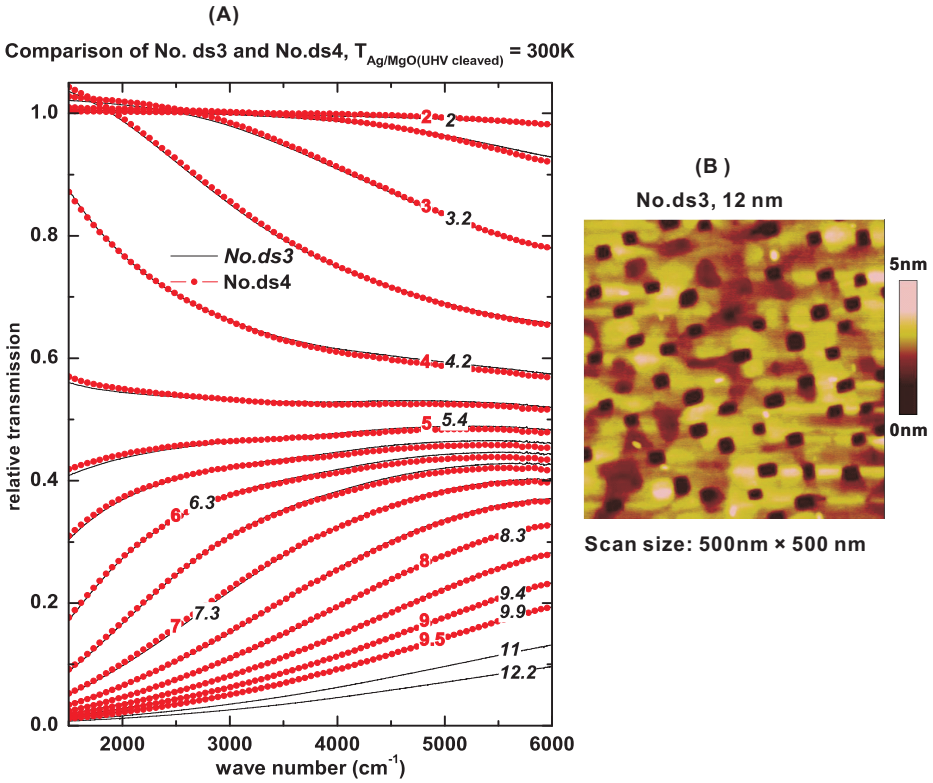

Figure 4.2: (A) Comparison of selected IR relative transmission spectra from two Ag-film growth experiments at room temperature on UHV cleaved MgO(001) surfaces under similar conditions. Spectra at the same thickness are perfectly superposed. The spectra of film No.ds4 have been shown in Fig. 4.1 (A).
(B) The AFM image of this film.

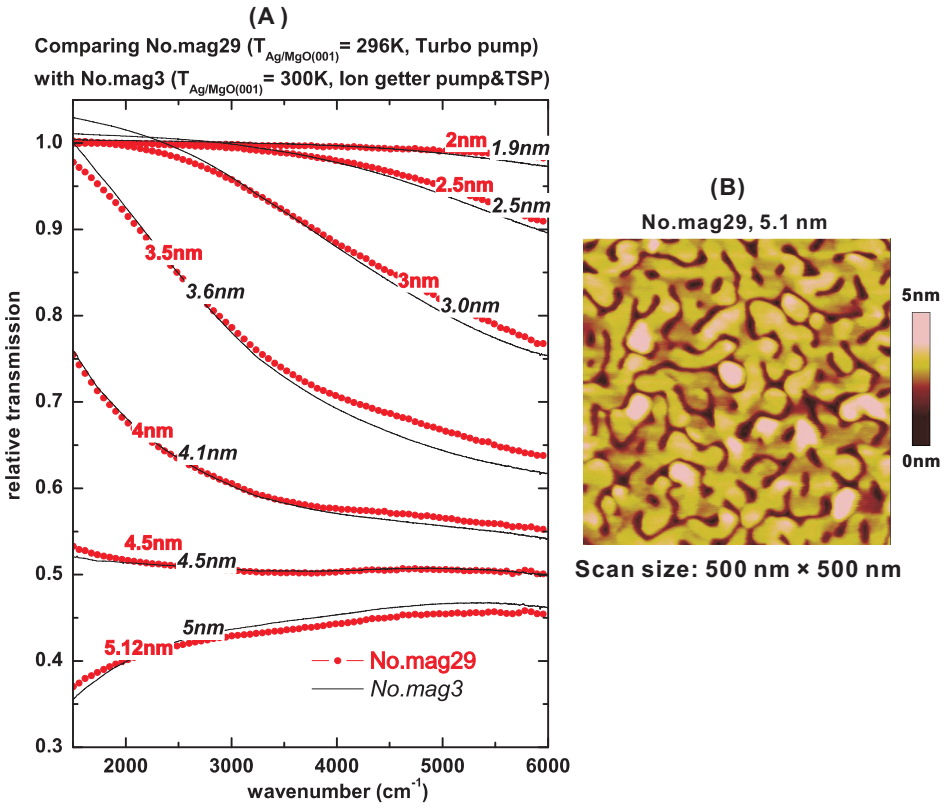

Figure 4.3: (A) Comparison of IR relative transmission spectra from two Ag-film gowth experiments on UHV-cleaved MgO(001) at room temperature. A pressure below 1×10^{-10} mbar was kept by an ion getter pump and a TSP (Titanium Sublimation Pump) during the growth of film No.mag3, and a pressure around 3×10^{-9} mbar was kept only by a turbo molecular pump during the growth of film No.mag29. Only a slight effect of base pressure on film growth is observed. Spectra of film No.mag3 have been shown in Fig. 4.1 (A).
(B) The AFM image of film No. mag29.

observed a smooth surface with smaller holes on film No.ds3 than that on film No.ds4 (see image (4) in Fig. 4.1 (B)).

Base pressure is also a possible factor influencing the film growth. Some molecules in the residual gas may act as surfactant and affect the film morphology [69]. In Fig. 4.3 (A) we compare the spectra of a Ag film (No.mag29) prepared at a relatively high base pressure (3×10^{-9} mbar) with that of film No.mag3 (the base pressure during this film growth is below 1×10^{-10} mbar). The spectra of the two films only show a slight difference. Comparing the AFM image of film No. mag29 in Fig. 4.3 (B) with that of film No.mag3 (see image (2) in Fig. 4.1 (B)) results in a slightly smaller average width of the elongated structures of film No.mag29 due to a smaller film thickness.

4.1.2 IR Transmission Spectra of Ag Films Grown on MgO(001) with Gas Exposure

Tersoff *et al.* [70] pointed out that the onset of nucleation of the second layer on top of an island is associated with a critical island radius R_c, which depends on the Ehrlich-Schwoebel barrier at the step edge. Above this critical radius the islands start to coalescence. Another length scale L_n, which is roughly half the distance between islands, is helpful to illustrate the growth process [70]. If $R_c < L_n$, a second layer of islands can nucleate before the former islands coalescence, and a multilayer growth can be obtained. Hence a high density of islands, i.e. small island size, helps to grow a smooth film. From Eq. 2.46 we can see the density of clusters increases directly with the deposition rate and inversely with the diffusion coefficient in accordance with a power law, so the deposition rate is not a sensitive factor. If we increase the density of clusters by lowering the temperature, we will encounter the Ehrlich-Schwoebel barrier at step edges, which can suppress the interlayer transport at low temperatures. Hence the arriving adatoms nucleate on the top of clusters and give rise to the growth of three-dimensional islands with pyramid-like features. So, for getting a smooth film, on the one hand we need a high nuclei density in the nucleation stage, on the other hand we want high adatoms mobility in the growth stage so that they can roll over the steps effectively. We cannot achieve both by adjusting the temperature, but a surfactant can help a lot.

A surfactant, whose presence changes the growth mechanism and promotes smooth film growth, could be a metal layer deposited on the substrate surface before film deposition or it could be adsorbed gases. For using as surfactants, materials that have a low surface energy and a lack of chemical affinity to the growing material are required. In order to understand the function of surfactants many different models have been proposed. The function of a surfactant could be [2]: (a) modify the thermodynamic balance of the surface and interface energies; (b) promote interlayer diffusion; (c) introduce a high density of nuclei. As a method to produce smooth films, surfactants have been successfully applied in the epitaxial growth of ultrathin semiconductor and metal films [71, 72, 73, 74, 75].

Gas exposure during film growth may affect the morphology of the film by acting as a surfactant. A report [49] shows that CO exposure during Fe and Cu film growth on UHV-cleaved MgO(001) surfaces at different temperatures can decrease the percolation threshold. The presence of CO enhanced the lateral growth by changing the diffusion on the islands and in their vicinity [49]. We tried CO gas exposure at a pressure of 4×10^{-8} mbar as they did during the growth of film No.mag7 on a UHV-cleaved MgO(001) surface at room temperature. In Fig. 4.4 (a), comparing the spectra of film No.mag7 with the ones of film No. mag3 which was grown without gas exposure, no obvious discrepancies were found. That might be ascribed to the smaller surface energy of Ag compared to Cu. Hence the mobility of Ag adatoms or small islands in a low-pressure CO-gas surrounding is comparable with the case in UHV.

We also checked the effect of the presence of N_2 on the Ag film growth. The measured

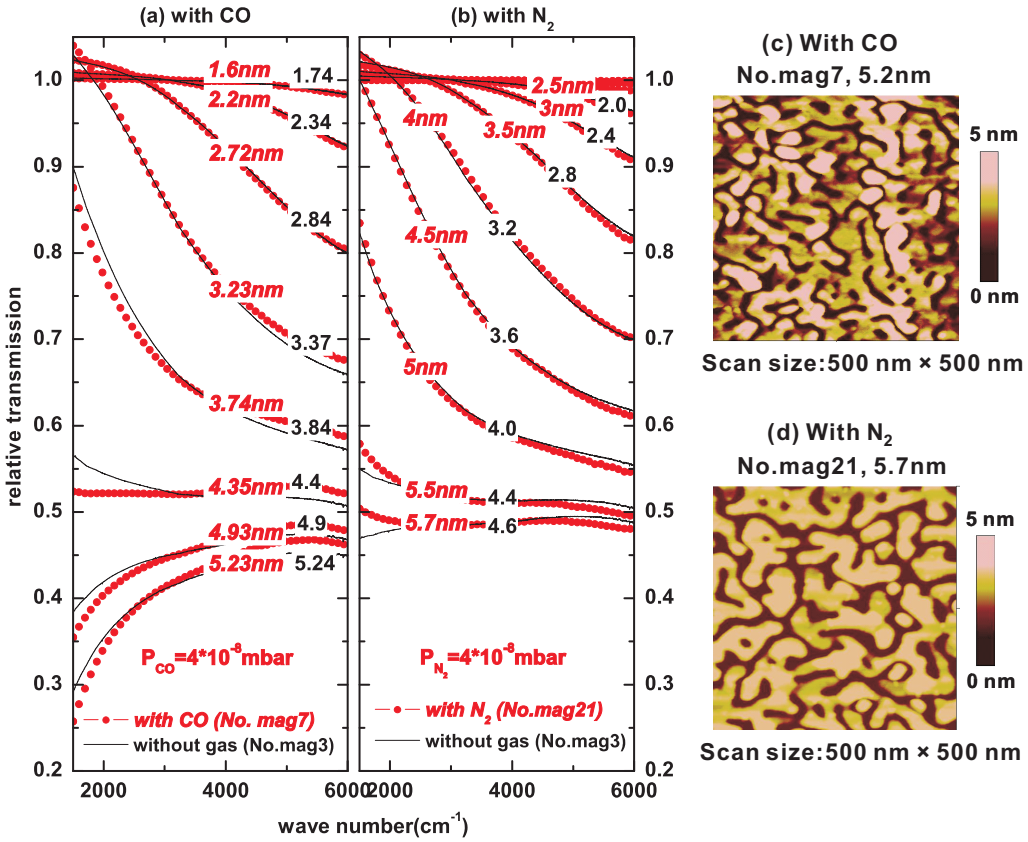

Figure 4.4: (a) Comparison of IR relative transmission spectra from two Ag-film growth experiments: one (No.mag7, dotted lines) is grown with CO exposure and another one (No.mag3, solid lines) without gas exposure.
(b) Similar comparison as in (a): the one (No.mag21, dotted lines) grown with N_2 exposure comparing to the same one (No.mag3, solid lines) grown without gas exposure.
All three films are grown on UHV-cleaved MgO(001) at about 300 K with almost the same deposition rate.
(c) and (d) AFM images of the films grown with CO and N_2 exposure respectively.

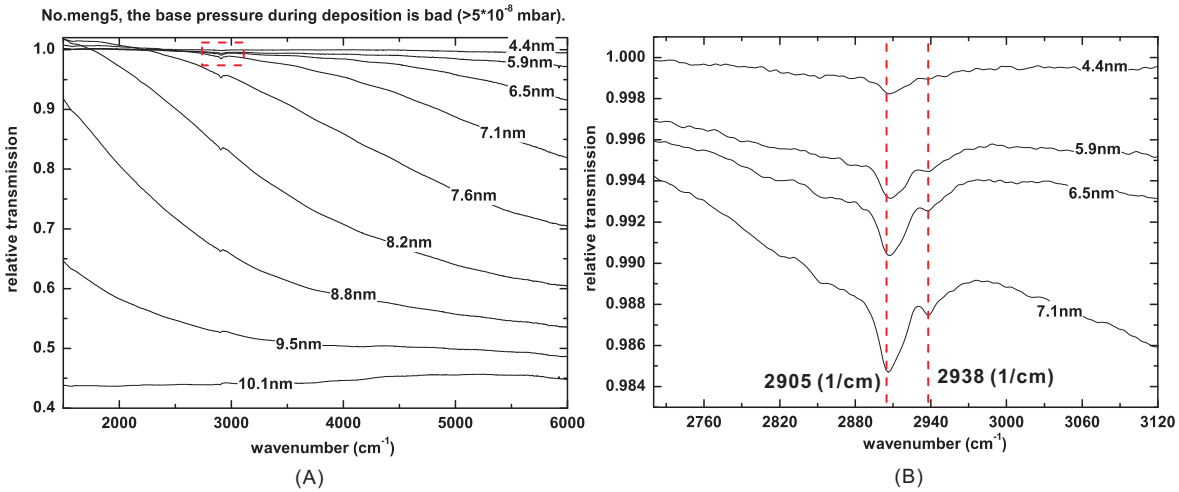

Figure 4.5: (A) Selected transmission spectra of a Ag film grown on a UHV-cleaved MgO(001) surface at room temperature in a bad base pressure ($> 5 \times 10^{-8}$ mbar). The part in the box in (A) is shown in a big scale in (B). Two peaks at around 2905 cm $^{-1}$ and 2938 cm^{-1} appeared on the spectra due to hydrocarbons in the residual gas.

spectra are shown in Fig. 4.4 (b) and compared to those of the same film grown without gas exposure as in (a). Like the case of CO exposure, we did not find any big effect due to N_2. The AFM images of these two films grown with gas exposure are shown in Fig. 4.4 (c) and (d). Both films show structures corresponding to the percolation threshold.

However, when there are hydrocarbons in the residual gas the film growth and the surface morphology can be changed. In Fig. 4.5 (A) we show the IR transmission spectra of a Ag film grown on a UHV cleaved MgO(001) surface at a relatively high base pressure ($> 5\times10^{-8}$ mbar). The high pressure was ascribed to the uncooled evaporator. The box area in (A) is shown in (B) in a big scale. As we can see, the spectra show two peaks at around 2905 cm^{-1} and 2938 cm^{-1} due to the adsorbed H-C bonds. Comparing the spectra of this film to those of the others shown in Fig. 4.1 (A), no superposition was observed, moreover, the thrasmittance of the spectrum at the percolation threshold is lower. The presented film thickness was overestimated due to the mislignment of the metal flux and the substrate surface.

Seeing from the IR spectra in Fig. 4.5, this film should have a surface morphology corresponding to the percolation threshold. However, as shown in Fig. 4.6, its AFM image shows big globose islands instead of the sinuous structures.

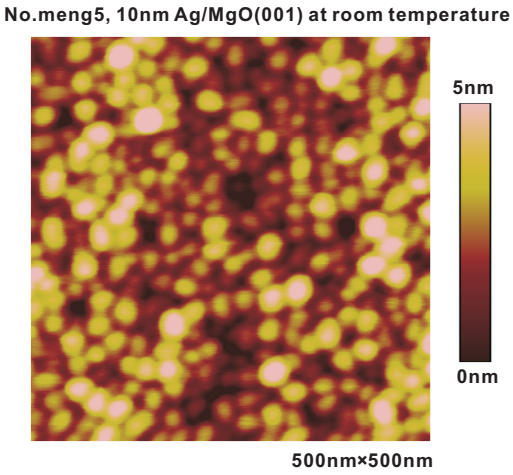

Figure 4.6: The AFM image of the 10 nm Ag film No.meng5. The IR spectra of this film was shown in Fig. 4.5.

4.1.3 Calculation of IR Transmission Spectra of Ag Films Grown on MgO(001)

Calculated results with the Drude-type Model

Above the percolation threshold, the Ag film becomes conductive and its spectra can be calculated with the Drude type model. As discussed in § 2.7.3, based on the bulk Ag data from literature, we use two additional frequency independent parameters $\omega_{\tau s}$ and β as fit parameters to calculate the spectra. The bulk Drude parameters $\omega^*_{\tau b}$= 135 cm^{-1} + 0.0386 ω and ω_{pb}= 74110 cm^{-1} are calculated from the data of Ordal *et al.* (see Fig. 2.11). The frequency dependence of the bulk relaxation rate $\omega^*_{\tau b}$ is very weak. In Fig. 2.11, the bulk Ag data from Christy *et al.* and Bennett *et al.* were also shown and they did not show a frequency dependence. We performed a fit with a constant $\omega_{\tau b}$=135 cm^{-1} too and compared it to the fit with $\omega^*_{\tau b}$.

A Drude fit was performed on all the measured spectra of film No.ds4. In (a) of Fig. 4.7 we show the fitted parameters based on $\omega^*_{\tau b}$ and $\omega_{\tau b}$ in a spectral range of 1500-3000 cm^{-1}. Here we introduced "*deviation*", which is the mean squared difference between measured spectra and calculated ones, to evaluate the fit quality. A smaller *deviation* means a better quality of fit.

Above a certain average thickness d_1 (around 8 nm), by varying the value of $\omega_{\tau s}$ in a certain range (e.g. from 0 to 500 cm $^{-1}$), the fit quality does not change significantly. That means the film already behaves like bulk Ag and some scattering from the surface will not disturb its properties. Thus we calculated the spectra only with the bulk relaxation rate $\omega_{\tau b}$. In accordance with this fact, β^2 approaches unity above d_1.

At another certain average thickness d_2 (around 6.5 nm), a strong increase in $\omega_{\tau s}$ starts. These large relaxation rates denote very short mean free paths of the charge carriers and indicate the breakdown of the Drude-type conductivity at this average

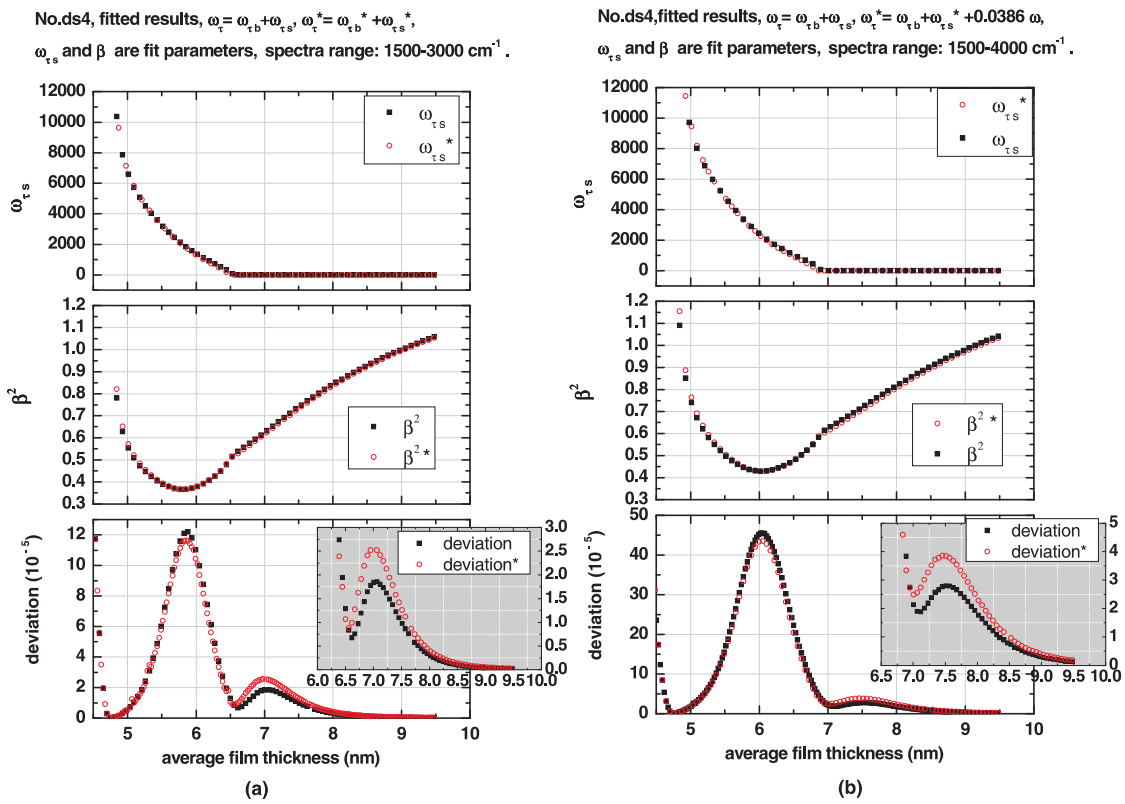

Figure 4.7: (a) The *deviation* and the best-fit parameters $\omega_{\tau s}$ and β^2 (solid square symbol lines, obtained with constant bulk $\omega_{\tau\ b} = 135\,\mathrm{cm}^{-1}$) and *deviation**, $\omega^*_{\tau s}$, β^{2*} (void circle symbol lines, fitted with frequency dependent bulk $\omega^*_{\tau b} = 135\,\mathrm{cm}^{-1} + 0.0386 \cdot\omega$) versus film thickness, the fit is performed in the range of 1500-3000 cm^{-1}; (b) fitted parameters and the *deviation* for a fit in the range of 1500-4000 cm^{-1}.

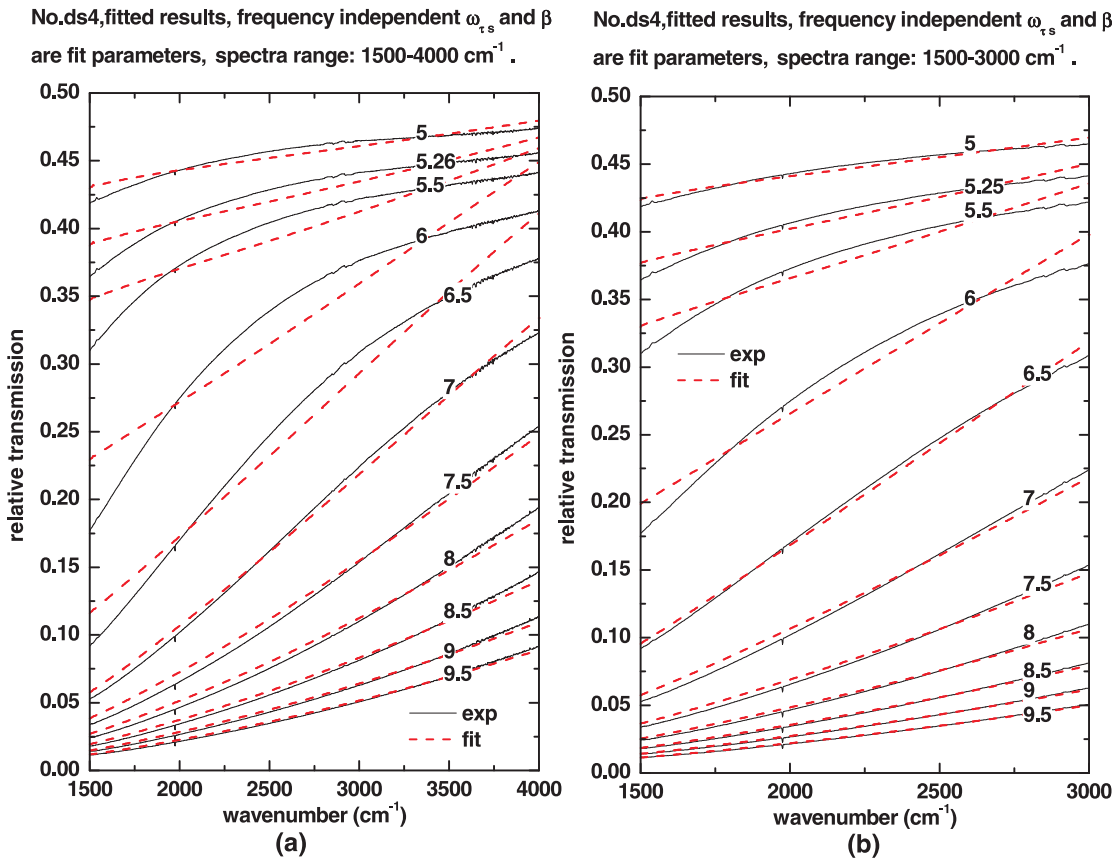

Figure 4.8: Comparison of the measured spectra of film No.ds4 with fits in different ranges: (a) 1500-4000 cm^{-1}; (b) 1500-3000 cm^{-1}. The numbers denote the film thickness.

thickness and below it. The thickness d_2 locates at the position of the first minimum value of *deviation* when we count from the high-thickness side.

The decrease of β^2 with decreasing thickness corresponds to an increase of depolarization fields. An increase of these depolarization fields indicates an increasing amount of tilted surface area or an increasing long-range roughness amplitude. Where the minimum of β^2 appears, the *deviation* shows a maximum value.

At another point, for the two fits based on $\omega_{\tau\mathrm{b}}$ and $\omega^*_{\tau\mathrm{b}}$ respectively, the *deviation* for the one based on $\omega_{\tau\mathrm{b}}$ is smaller. Thus the fit based on $\omega_{\tau\mathrm{b}}$ is better.

In (b) of Fig. 4.7, we show the results of fits to the same film in a spectral range of 1500-4000 cm^{-1}. Compared with that in (a), only because the spectral range was expanded to higher frequencies, d_1 and d_2 shift to higher thicknesses (d_1 to 8 nm and d_2 to 7 nm). Also the *deviation* for both fits show bigger values than that shown in (a). The minimum value of β^2 is at a higher thickness than in (a). The valid fit extends from the final film thickness to a smaller one in (a) than in (b).

In Fig. 4.8 and Fig. 4.9, we show the fitted spectra in different spectral ranges based on $\omega_{\tau\mathrm{b}}$ together with the measure ones. From these two figures, we get an intuitive insight

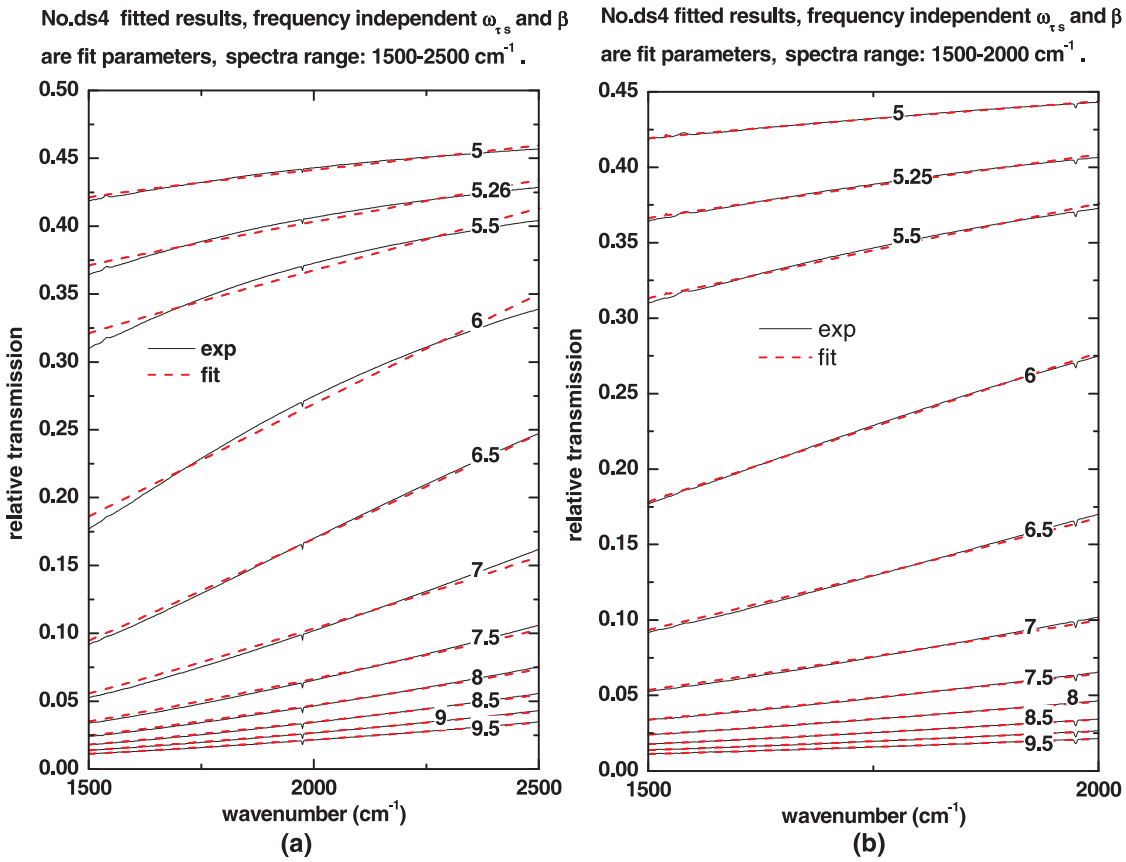

Figure 4.9: Comparison of the measured spectra of film No. ds4 with fits in different spectral ranges: (a) 1500-2500 cm^{-1}; (b) 1500-2000 cm^{-1}. The numbers denote the film thickness.

of that effect. d_2 becomes smaller when the spectral range of the fit is concentrated to the low-frequency side. For example, in Fig. 4.8, d_2 locates around 7 nm in (a) and around 6.5 nm in (b); in Fig. 4.9, d_2 locates below 6.5 nm in (a) and below 5 nm in (b).

In Fig. 4.10 we collected the fitted parameters of some fits to the spectra of film No.ds4 in different spectral ranges. It is more clear that when the spectral range of the fit is more concentrated to low-frequency side, the onset of the strong increase of $\omega_{\tau\mathrm{S}}$ shifts to lower thicknesses and the *deviation* becomes smaller. Above about 6.2 nm, the value of β^2 does not vary much with the fits in different spectral ranges.

To explain that conclusion we need to recall a study by G. Fahsold *et al.* [76]. As we mentioned above, although we can calculate the IR spectra of Ag film above the percolation threshold with the Drude type model, the film is still rough and inhomogenous as we saw from the AFM images. The effective medium model developed by Bruggeman is well suited for calculating the IR-optical properties of such kind of films even in the vicinity of the percolation threshold (below and above) [76]. In the Bruggeman model, a rough metal film is regarded as a two- or three-dimensional mixture of a metal (with

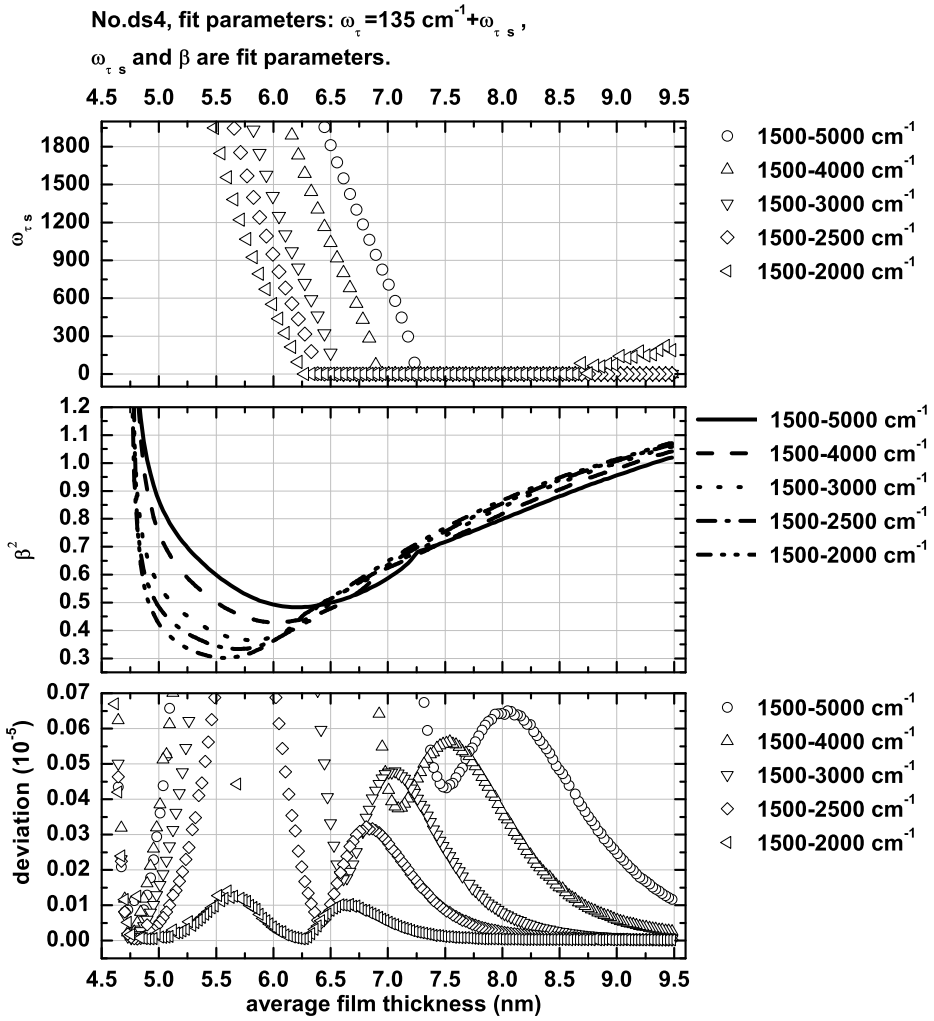

Figure 4.10: The *deviation* and the best-fit parameters $\omega_{\tau \mathrm{s}}$ and β^2 versus film thickness of some fits in different spectral ranges. The dielectric function of the Ag film is based on the constant Drude parameters: $\omega_{\tau\ \mathrm{b}} = 135\,\mathrm{cm}^{-1}$ and $\omega_{p\mathrm{b}} = 74110\,\mathrm{cm}^{-1}$.

volume fraction F) and a dielectric (with volume fraction 1-F). A very thin Ag island film can be considered as a two-dimensional mixture. Using Eq. 2.44 we can calculate the effective dielectric function ε_{eff} of such a two dimensional-mixture. In the equation, the dielectric function ε_{m} for Ag was calculated with the two constant Drude parameters ($\omega_{\tau\text{b}}$= 135 cm^{-1} and $\omega_{p\text{b}}$ = 74110 cm^{-1}) by Eq. 2.35, and that for the dielectric (in our case is vacuum), ε_{h}, we took 1. Here we only consider the case of conducting films above the percolation threshold, i.e., F>F_c (F_c is the critical filling fraction, which is 1/2 for a two dimensional medium). In Fig. 4.11 we show the imaginary part of calculated ε_{eff} at a few volume fractions F. The imaginary part of the Drude bulk Ag dielectric function is shown for comparison. On each curve with different F, the frequency dependence of Im ε_{eff} shows a transition at a certain frequency, which was roughly marked by a dashed line. G. Fahsold *et al.* [76] call this certain frequency ω_{max}. They found above ω_{max}, the ε_{eff} is dominated by ε_{h} (if there are adsorbate layers on the film surface, ε_{h} has a value above 1), whereas below ω_{max} at the low-frequency region, ε_{eff} is almost independent from ε_{h} and shows metal-like effective properties. In addition, when the filling fraction F of a film fullfills a relation like

$$\left|\frac{\text{Re}\varepsilon_{\text{m}}}{\varepsilon_{\text{h}}}\right| \gg \frac{1}{(F-F_c)^2} - 2, \tag{4.1}$$

the film can be described by a Drude-type dielectric function. As it is shown in Fig. 2.12, Re ε_{m} has smaller values at high-frequency side. Thus at a certain F, the invalidity of this relation always starts from the high-frequency side. Relation 4.1 corresponds to a spectral range of ω<ω_{max}, where to a good approximation

$$\omega_{max} = \omega_{p\text{b}} \cdot (F - F_c)/\sqrt{\varepsilon_{\text{m}}}, \tag{4.2}$$

with $\omega_{p\text{b}}$ being the plasma frequency of bulk Ag. A small change of ε_{h} will modify ω_{max} (a bigger value of ε_{h} shifts ω_{max} to low-frequency side) but it does not influence the effective Drude parameters $\omega_{\tau\text{eff}}$ and $\omega_{p\text{eff}}$ in the spectral range ω<ω_{max} [76].

It could be due to the existence of ω_{max} in our measured spectral range so that we cannot fit the spectra in the whole spectral range as they were measured. Above ω_{max}, the IR properties of a film are not Drude-like any more. For example, for the fitted $\omega_{\tau\text{s}}$ in a spectral range of 1500-4000 cm^{-1}, the strong increase appears at around 7.1 nm. That means for the 7.1 nm film, we can only fit its spectrum with the Drude type model in a spectral range below 4000 cm^{-1}, which can be regarded as ω_{max} for the 7.1 nm thick film. Using Eq. 4.2 we can calculate the filling fraction of the 7.1 nm film. In table 4.2 we show the estimated filling factor F at a few thicknesses from the fitted results shown in Fig. 4.10. The filling factor F shows an increase with the increase of average film thickness. This is in accord with the findings on AFM images of room-temperature prepared films shown in Fig. 4.1 (B), where the surface area of Ag increases with the increased average film thickness.

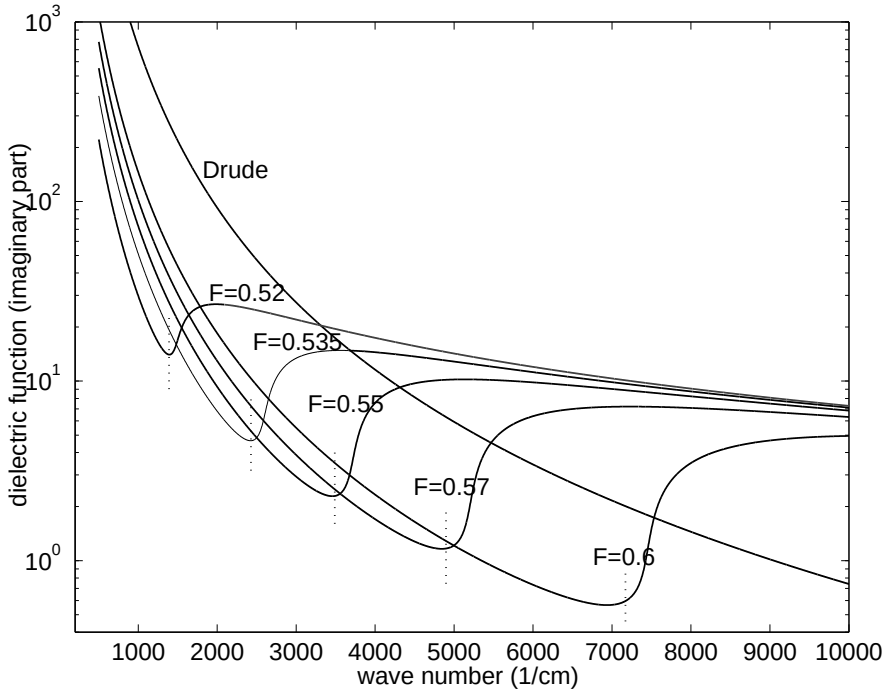

Figure 4.11: Imaginary part of the dielectric function ε_{eff} for a two-dimensional inhomogeneous medium in different filling fraction F of metal (for example F =0.55 means a medium composed of 55% Ag and 45% vacuum) and for Drude bulk Ag. The dashed lines mark the position of ω_{max} where the transition starts. On each curve, the part below ω_{max} can be calculated with a Drude type model.

Table 4.2: Estimated filling fraction of a film at a few thicknesses from the fit results of Fig. 4.10 obtained with Eq. 4.2, ε_{h}= 1, F_c = 0.5, ω_{pb} = 74110 cm $^{-1}$.

thickness(nm)	$\omega_{max}(\mathrm{cm}^{-1})$	F
7.5	5000	0.567
7.1	4000	0.554
6.6	3000	0.54
6.4	2500	0.534
6.3	2000	0.527

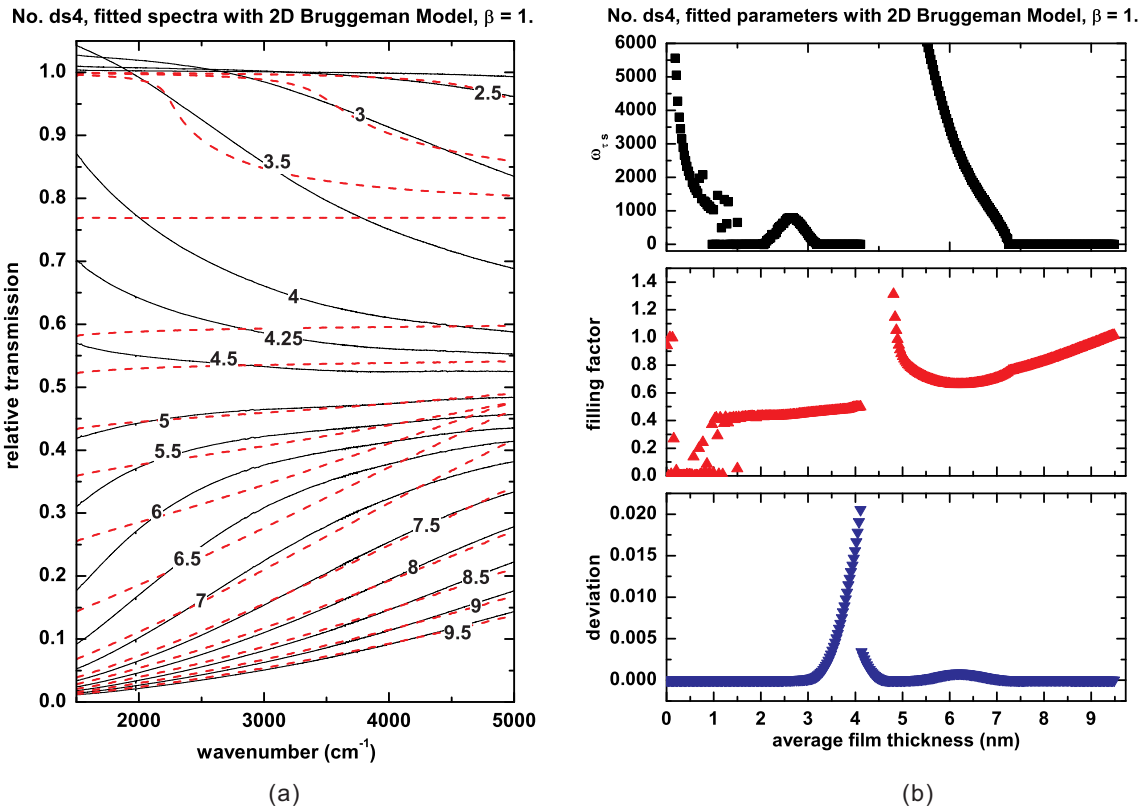

Figure 4.12: (a) Best fitted spectra of film No.ds4 by the Bruggeman Model together with the measured ones. The Bruggeman model cannot describe the relative transmittance over 100% at low coverage of Ag. In the vicinity of the percolation threshold (below and above), the spectra also cannot be fitted due to the special surface morphology. The numbers denote the film thicknesses.
(B) The *deviation* and the best-fit parameters $\omega_{\tau s}$ and F versus average film thicknesses, $\beta = 1$. Near the percolation threshold, the fit parameters have no physical meaning. Near the final thickness, F is close to 1.0 and $\omega_{\tau s}$ equal to zero, which indicates the bulk properties of the Ag film.

Calculated Results with the Bruggeman Model

- The IR optical properties of a Ag film consisting of islands or holes can be described by the Bruggeman model. In the effective dielectric function of such a system (described by Eq. 2.43), for the dielectric function of metal particles ε_{m} we take the Drude-type one for thin films. The dielectric in our case is vacuum, so $\varepsilon_{\mathrm{h}} = 1$. In the calculation, the frequency independent but thickness dependent parameters $\omega_{\tau \mathrm{s}}$ and the filling fraction F are used as fit parameters. As shown in § 4.5.2, the SEIRA peaks of CO adsorbed on ultrathin Ag films consisting of small islands did not show a shift following the increase of Ag coverage, so the islands already show bulk Ag properties. Thus for the calculation we set $\beta = 1$. In Fig. 4.12, the best fitted spectra are shown in graph (a) and fit parameters in (b).

At low-frequency side and at low coverage of Ag, the relative transmittance is over 100%, which cannot be described by the the Bruggeman model. In Fig. 4.12 (a), the fitted spectra show 100% transmittance in that area. Below the percolation threshold, above 3.5 nm, the *deviation* shows a sharp increase and the spectra cannot be fitted anymore. The model breaks down due to the big sinuous structures in reality (see AFM images in Fig. 4.1 (B)). Below the percolation threshold, we always get a filling factor $F < 0.5$. Above and near the percolation threshold, $\omega_{\tau \mathrm{s}}$ values are very high and F values are meaningless, which are the expected behaviour of percolation. Near the final thickness, F is close to 1.0 and $\omega_{\tau \mathrm{s}}$ equal to zero, which indicates the bulk properties of the Ag film. This is in accord with the fit parameters with the Drude type model shown in Fig. 4.10.

4.1.4 IR Reflection Spectra of Ag/MgO(001)

IR Reflection Spectra of Ag Films Grown on UHV Cleaved MgO(001)

In Fig. 4.13 we show the IR relative reflectance spectra measured during a Ag film growth in the range of 1000-6000 cm^{-1} with a resolution of 2 cm^{-1}. The spectra are recorded in oblique incidence (80°) with p-polarized IR light. The Ag film was grown on a UHV-cleaved MgO(001) surface at room temperature. In the beginning the relative reflectance decreases with the increase of Ag coverage. Then at a certain thickness we observed a minimum reflectance. Above that thickness, the reflectance starts to increases again. The reflectance changes fast with slowly changing Ag coverage near the minimum reflection area. A fast transition of film properties must occur there. The thickness at the minimum reflectance is found close to the percolation threshold found in transmission measurement at the same temperature. Since the Ag film growth at room temperature was reproduced very well as seen from the measured transmission spectra, it is reasonable to make a comparison of the spectral properties measured in both transmission and reflection geometries.

Generally, during a film growth process, we record one spectra in every 14 to 25 sec-

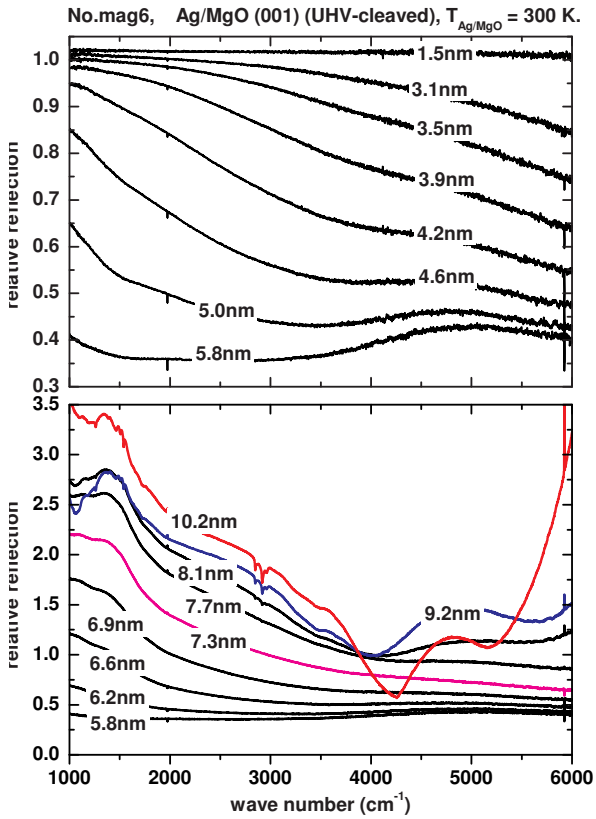

Figure 4.13: Selection of relative reflection spectra of Ag/MgO(001) at room temperature. The labels show the average film thickness. In the upper part are the spectra before the minimal reflectance spectrum and in the lower part are those of the same film beyond that. This thickness is related to the threshold which we explained in transmission spectra measurement.

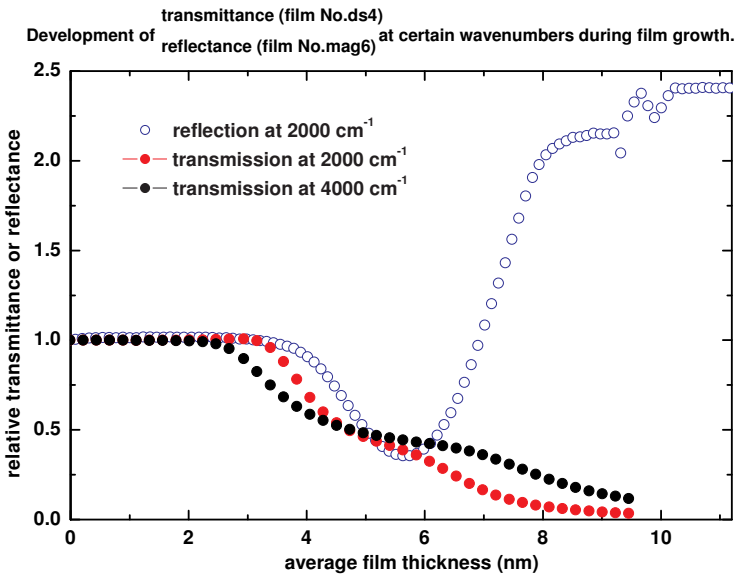

Figure 4.14: Comparison of the reflectance development at 2000 cm^{-1} of film No.mag6 with the transmittance development at 2000 cm^{-1} and 4000 cm^{-1} of film No.ds4 following the increase of Ag coverage. Both films are prepared on UHV-cleaved MgO(001) at room temperature. The crossover of the transmittance developments at two different frequencies indicates the percolation threshold.

onds. Running through all the measured spectra during the growth of a film, we make a cut at a certain wavenumber, so we get a section view of transmittance or reflectance development along the changing film thickness at this wavenumber. In Fig. 4.14 we plot the development of relative reflectance of this film at 2000 cm^{-1} together with the development of transmittance of another film (No.ds4) at 2000 cm^{-1} and 4000 cm^{-1}. The two films are prepared at similar conditions. We see the minimum of reflectance does not overlap with the optical crossover of transmittance that we define as the percolation threshold. It is well known that from this kind of minimum the real contribution of the Drude-type absorption starts to increase with average film thickness, whereas before the minimum the absorption really is caused by the polarizability of small particles [43]. In accord with this relationship the effect is due to the island-like growth process.

In the literature this effect is not reported until now, but actually it is very similar to the anomalous absorption behavior of granular gold films [77, 78], i.e., a maximum of the optical absorption near the percolation threshold. J. Peiro *et al.* [78] measured it on granular gold films (they studied in a range from $\lambda = 0$ to 3 μm) and also performed calculations based on the effective medium theories by taking into account the actual morphology of the films. According to their explanation this abnormal absorption at and near the percolation threshold can be attributed to the classical surface plasma modes, generally situated in the visible range for spheroidal inclusions, broadened here

towards higher wavelengths due to the formation of fractal clusters of various sizes. Because one side the optical resonant absorption due to this surface plasma modes in clusters has a maximum at the percolation threshold and starts to decrease above that, on the other hand the metallic absorption from the infinite cluster starts to increase at the percolation threshold, the absorption of the film gives a measured absorption maximum locating slightly above the percolation threshold. This conclusion also fits to our measured relation between the reflection minimum and the percolation threshold.

When the film becomes thicker (above 7.5 nm) the relative reflectance passes 100%, which indicates higher reflectance than that of the MgO surface. When the film becomes even thicker, a strong broad absorption band around 4250 cm^{-1} appeared. The explanation of that is still unclear.

In Fig. 4.15 we compare the spectra of film No. mag6 with that of film No. mag8. Their spectra below and above the minimum reflection are all superposable, while near the the minimum reflection area, there is a big difference. In most of the transmission measurements we hardly see that. It seems that the measurements in reflection geometry are more sensitive.

In Fig. 4.16 (a), we show the reflection spectra of a 3.94 nm Ag film grown on a UHV-cleaved MgO(001) surface. Above the reflectance minimum, after two more spectra were measured, the film deposition was stopped. The film thickness at the reflectance minimum is 3.86 nm. After the film was prepared we turn the sample to the position for transmission measurement. A single channel spectrum of the Ag/MgO(001) system was measured. With the way presented in § 3.1.3, the relative transmission spectrum at the final thickness was calculated with a pre-measured reference spectrum of MgO(001). In Fig. 4.16 (b), we compare this spectrum to one from film No.mag1 and we get an intuitive insight of how the percolation threshold is related to reflectance minimum.

IR reflection spectra of Ag films grown on air cleaved MgO

Here we present the effect of another factor on film growth: defects on the substrate surface. MgO (100) surfaces prepared by cleaving in air are irreversibly damaged by water vapor, which generates point defects [79]. Furthermore they are contaminated by H_2O and CO_2 adsorbed on steps and kinks. The surface can be cleaned by annealing in vacuum but surface defects, probably vacancies will remain. This is not the case for MgO(001) surface prepared by *in situ* cleaving in a UHV chamber. Such surfaces are clean but contain structural defects, which are mainly atomic steps. Studies of Fe films grown on such two kinds of MgO(001) surfaces have been reported by G. Fahsold *et al.* [46]. They knew from He-atom studies that Fe grows on perfect MgO(001) as 3D islands before the coalescence of these islands leads to a complete coverage of the substrate.The exposure of the substrate surface to air helps to partially overcome the tendency towards 3D growth. Finally they found, at the same thickness, the IR-transmittance of films grown on air-cleaved substrates is clearly lower compared to that of films grown on UHV-cleaved substrates. In this work we will show some similar studies on Ag-film growth here and Cu-film growth in § 5.1.

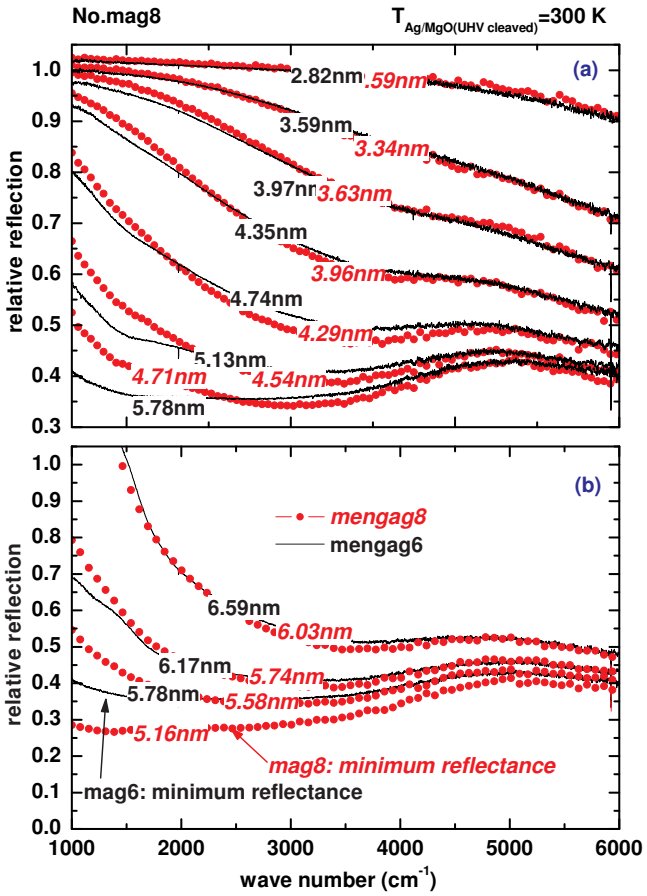

Figure 4.15: Comparison of selected IR relative reflection spectra from two Ag-film growth experiments on UHV cleaved MgO(001) surfaces at room temperature. In (a) are the spectra before the minimum reflectance spectrum and in (b) are those of the same film beyond that.The spectra of No.mag6 have been shown in Fig. 4.13. The average film thicknesses for the spectra in dotted lines are indicated in italic letters.

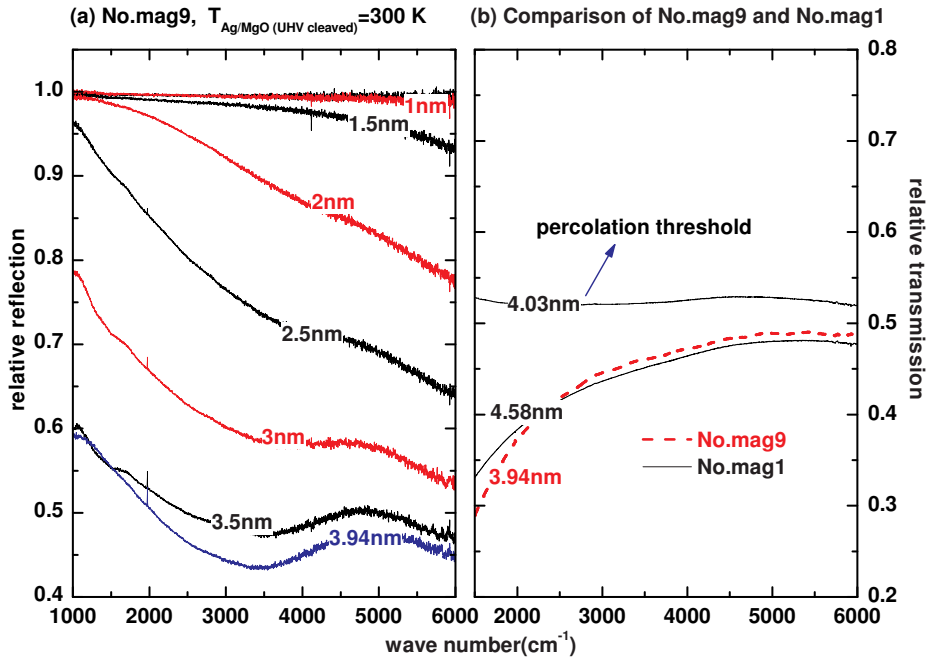

Figure 4.16: (a) Selected relative reflection spectra taken during a Ag-film growth on a UHV-cleaved MgO(001) surface at room temperature. After the minimum reflection appeared, two more spectra were measured before the deposition was stopped. (b) Comparison of the relative transmission spectrum measured at the final thickness of this film (dashed line) with the spectra from another experiment (solid lines, No.mag3).

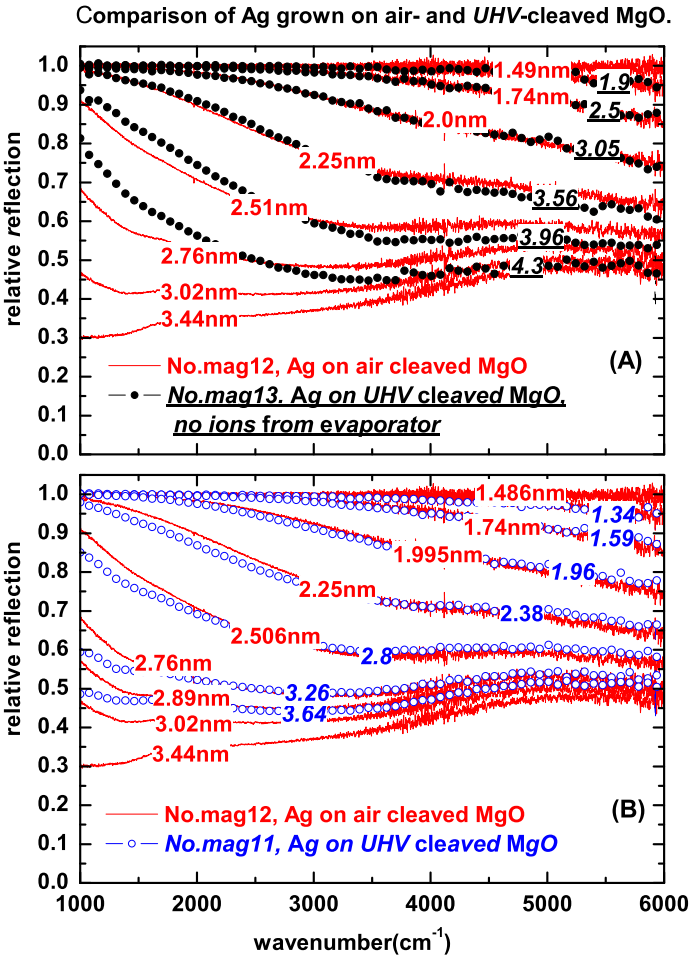

Figure 4.17: Comparison of IR relative reflection spectra from different Ag-film growth experiments at room temperature. The spectra of film No.mag12 grown on air cleaved MgO(001) was compared to that of film No. mag13 in (A) and to that of film No. mag11 in (B). Both film No. mag11 and film No. mag13 are grown on UHV-cleaved MgO(001) surfaces. For film No.mag13, the ions from the metal beam source were taken away by putting a piece of magnet at the outside of the evaporator.

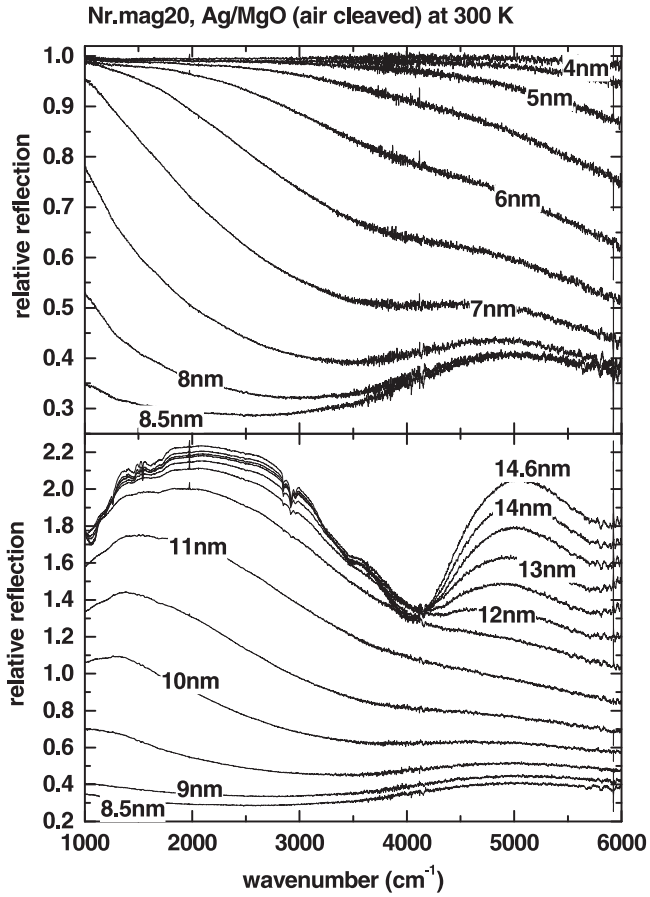

Figure 4.18: Selected IR reflection spectra of a Ag film grown on an air-cleaved MgO(001) surface at about 300 K. In (a) are the spectra before the minimum reflectance and in (b) are those beyond that. The film thickness is about 60% overestimated due to the misalignment of metal flux with the substrate surface. The broad absorption band around 4250 cm^{-1} was observed again.

Defects on MgO(001) were also investigated in cluster calculation, and it was found that a single metal atom (Cu, Ag) binds significantly more strongly there [80].

In Fig. 4.17, selected IR relative reflection spectra of Ag film No.mag12 grown on an air-cleaved MgO(001) surface are compared with those of two Ag films grown on UHV-cleaved MgO(001) surfaces. Film No.mag12 is compared to film No.mag13 in (A) and to film No.ag11 in (B). We find their spectra are superposable at low Ag coverage, but the corresponding thickness of film No.mag12 is always lower than that of the other two films. Thus the film grown on air-cleaved MgO reaches the minimum reflectance at a smaller thickness. In the vicinity of the minimum reflectance, big difference appears. Refer to the relation between the percolation threshold and the minimum reflectance, we see the percolation threshold was lowered down due to the defects on air-cleaved MgO surface. The defects affected the nucleation process.

In Fig. 4.18 reflection spectra of a Ag film grown on air-cleaved MgO are shown. The average film thickness of this film was about 60% over-estimated due to the misalignment of metal flux with substrate surface. Since the broad absorption band around $4250\,\mathrm{cm}^{-1}$ appears again, the film must be very smooth. On this film we measured weak CO signal only in reflection geometry.

In Fig. 4.19, IR reflection spectra from two Ag film growth experiments are compared. It shows that a MgO(001) surface prepared in the UHV chamber can be kept for at least one day without getting contaminated.

Calculation of Reflection Spectra with the Bruggemann Model

Both the perpendicular and parallel dielectric components in the film can be detected by measuring in oblique reflection geometry. The three dimensional (3D) Bruggeman Model is a easy way for including the perpendicular component in the calculation. With the same fit parameters $\omega_{\tau s}$ and F as we used for the calculation of transmission spectra, setting $\beta = 1$, the reflection spectra of a room-temperature prepared film can be calculated with the 3D Bruggeman Model. In the Model, the filling factor at the percolation threshold is $F_c = 1/3$. In Fig. 4.20, the best-fit parameters of a fit to the spectra of film No.mag6 are shown in (b) and the best-fit spectra are shown in (a). As we saw from Fig. 4.14, the absorption of the Ag film starts form about 2.5 nm. Thus, below 2.5 nm the fit parameters shown in (b) are meaningless. As shown in Fig. 4.20, in the range of 2.5 nm to 3.5 nm, the spectra are fitted well. For the range above 3.5 nm, as in the fit to the transmittance spectra, a Bruggeman Model is impossible to describe the spectra due to the special surface morphology. However, at higher thicknesses far beyond the minimum reflectance, the *deviation* between calculation and measurement is still big, which probably indicates the anistropy of the film conductivity.

The existance of the minimum reflectance was proved by an ideal reflection calculation with the 3D Bruggeman Model. In Fig. 4.21, the results of such an calculation were shown. During the calculation, the film thickness is set at 6 nm and the filling fractor F acts as the varying parameter. In Fig. 4.21, the calculated reflection spectra are shown in (a) and (b), and the reflectance development of these spectra at $4000\,\mathrm{cm}^{-1}$

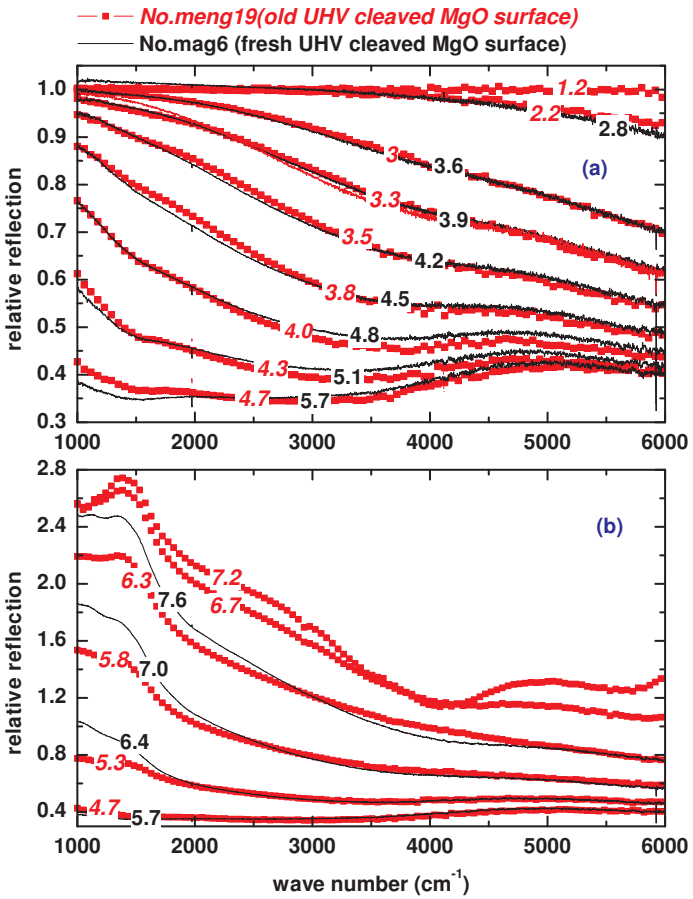

Figure 4.19: Selected IR reflection spectra of film No.meng19 grown on an old UHV-cleaved MgO(001) compared with those of the film No.mag6 grown on a fresh UHV-cleaved MgO at about 300 K. The old MgO(001) surface was kept in UHV for one day. No big discrepancy even near the minimum reflection area was found, as expected.

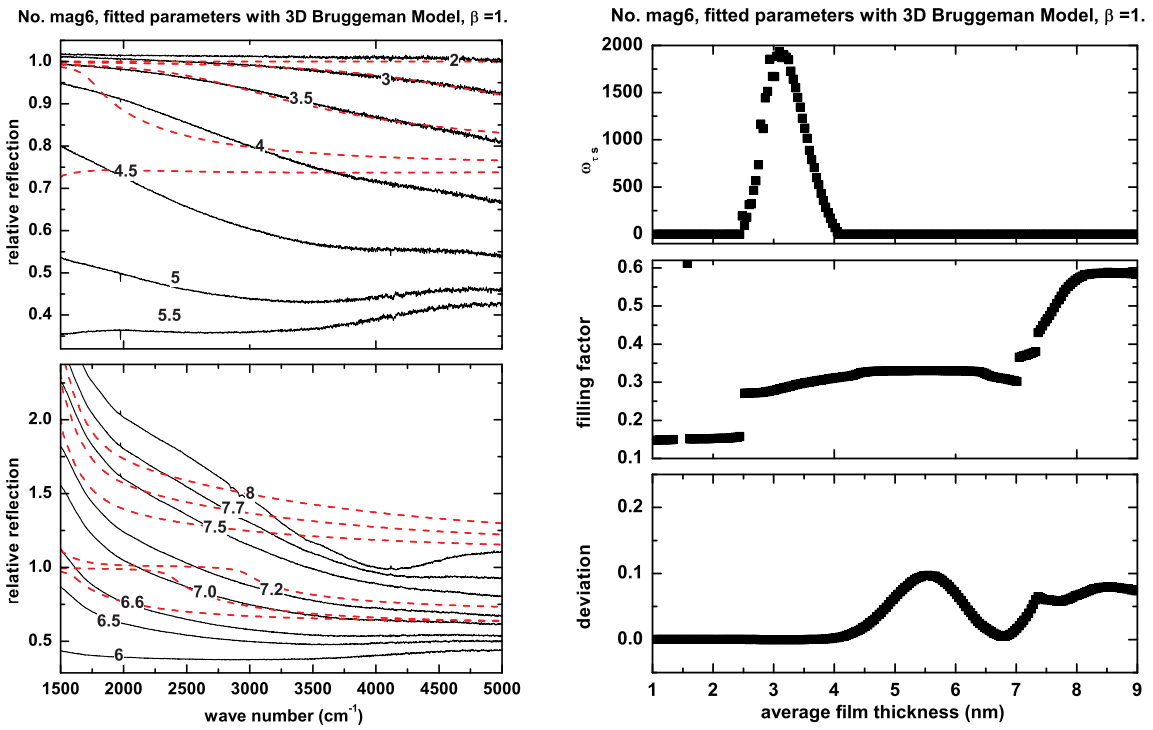

Figure 4.20: (a) The best fitted spectra of Ag film No. mag6 with the 3D Bruggeman Model shown in Eq. 2.43. The spectra before the minimum reflectance are shown in the upper picture and those beyond the minimum reflectance are shown in the picture below.
(b) The *deviation* and the best-fit parameters $\omega_{\tau s}$ and F versus the average film thickness.

Table 4.3: List of experiments performed at low temperatures. d denotes the average film thickness; "rate" denotes the evaporation rate; "geometry" means the measurement in transmission (T) or in reflection (R) geometry.

	Substrate temperature	Pressure during deposition	Deposition	final thickness	IR Spectroscopy	CO exposure		
Exp	T (K)	P (10^{-10} mbar)	rate (nm/min)	d (nm)	geometry	T (K)	P_{co} (10^{-8}mbar)	geometry
ds2	100	1.5	0.103	7.4	T	103	2.6	T
ds7	96	4.8	0.104	5.2	T	95	9	T
mag2	96	1.5	0.14	4.2	T			
mag19	93	<1	0.103	2.3	T			
d5	69~63	2.1	0.096	4.9	T	55	2	T
mag15	48	<1	0.156	5.7	R			
mag16	49	<1	0.92	4.5	T			

is shown in (c). Obviously, the minimum reflectance appears at $F = 1/3$, which is the filling factor at the percolation threshold. In reality, as we mentioned above, the real measured minimum reflectance locates slightly above the percolation threshold due to the island-like growth process. In (b), the spectrum of the assumed 6 nm Ag film calculated with a Drude Model was shown also. It overlaps with the spectrum calculated with the 3D Bruggeman Model at $F = 1$, that is in accordance with what we found in the fit to transmittance spectra.

4.2 Ag Films Prepared at Low Temperatures Cooled with Liquid N_2 or Liquid He

We can cool the sample down to about 100 K and 50 K with liquid Nitrogen or liquid Helium. Both IR spectra and AFM images of Ag films grown at such temperatures show different properties from that of Ag films grown at or above room temperature. Some interesting things are also found when CO was exposed to these films at the same temperature as they were prepared. Table 4.3 shows a list of experiments performed at low temperatures, of which the results are shown in this section.

4.2.1 IR Spectra of Ag Films Grown on MgO(001) at about 50 K

In Fig. 4.22 we show relative reflection spectra of a silver film (No.mag15) grown at about 50 K on an air-cleaved MgO(001) surface. As we measured on the room-

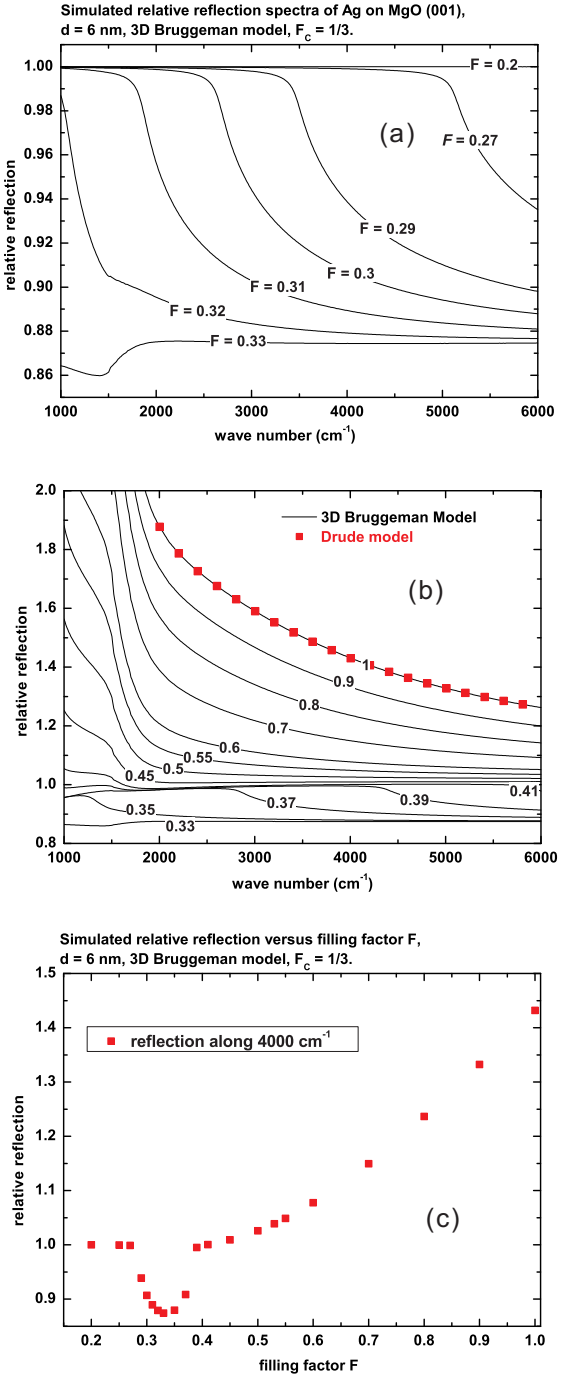

Figure 4.21: (a) (b) Simulated reflection spectra of a Ag film grown on MgO(001) with the 3D Bruggeman Model. The film thickness is fixed at 6 nm and the filling factor F is varied. The minimum reflection appears at $F_c = 1/3$. The square-symbol line in (b) is the spectrum of a 6 nm Ag film calculated with Drude Model. For the dielectric function of the Ag islands (Ag film in Drude Model) ε_{m}, we took the two constant Drude parameters: $\omega_{\tau \mathrm{b}} = 135\,\mathrm{cm}^{-1}$, $\omega_{p\mathrm{b}} = 74110\,\mathrm{cm}^{-1}$. The numbers in (b) denote the filling factor F.
(c) The reflectance development of simulated spectra at $4000\,\mathrm{cm}^{-1}$ versus the filling factor F.

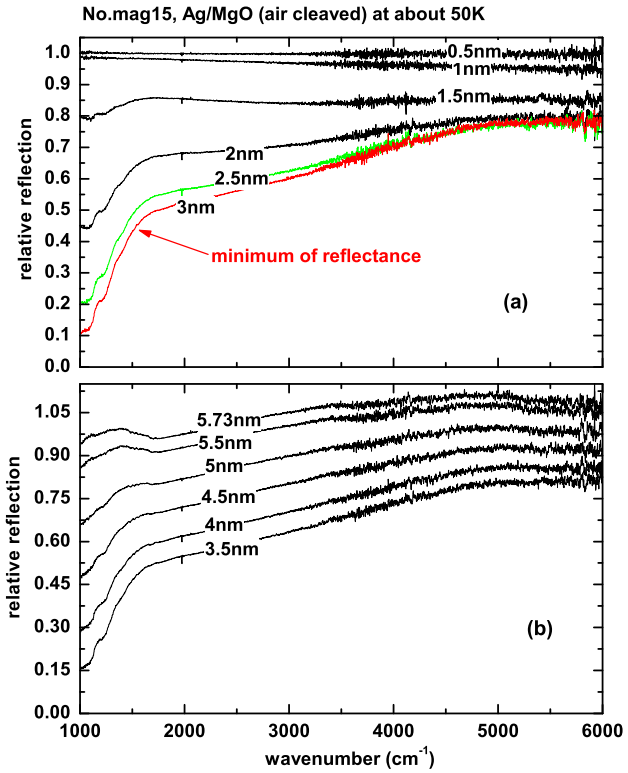

Figure 4.22: Selected relative reflection spectra of a Ag film grown on an air-cleaved MgO(001) surface at about 50 K. In (a) are the spectra before the minimum reflectance and in (b) are those beyond that.

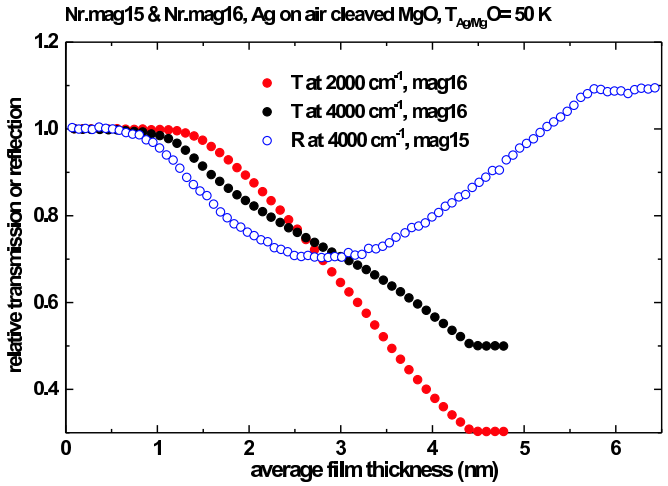

Figure 4.23: Comparison of the reflectance development at 4000 cm^{-1} of film No.mag15 with the transmittance development at 2000 cm^{-1} and 4000 cm^{-1} of film No. mag16 following the increase of Ag coverage. Both films are prepared on air-cleaved MgO(001) at about 48 K.

temperature prepared films we also get a minimum reflectance here. However, different from the spectra measured on room-temperature prepared films, most of the spectra show a positive slope except those below 1.5 nm.

In Fig. 4.23 we show the development of reflectance at 4000 cm^{-1} of this film compared with the developments of transmittance at two wave numbers of another film (No.mag16) prepared under similar conditions. We find the same conclusion that the minimum reflection stays at a thickness above the percolation threshold.

In Fig. 4.24 we show relative transmission spectra of one film grown on an air-cleaved (No.mag16) and another one on a UHV-cleaved (No.ds5) MgO(001) surface cooled by liquid He. The evaporation rates for the two films are almost equal. We find at the same thickness and same frequency, the transmittance of the film grown on UHV-cleaved MgO(001) is always lower than the one grown on air-cleaved MgO(001). This shows the reverse case as what we found on room-temperature prepared samples: the percolation threshold of a Ag film grown on air-cleaved MgO(001) is increased.

Refering to Eq. 2.47 we see the substrate temperature affects the n_x in an exponential way. A small decrease of temperature will produce a big increase on the total number of islands. That is one reason why we get smoother films at low temperatures than at high temperatures. Because the Ag adatoms have a high mobility even at low temperatures, the interlayer diffusion will not be suppressed, so that we get very smooth films. On an air-cleaved MgO(001) surface exist a lot of defects. Ag atoms stay more stable on defects so that bigger islands are formed on such a surface than on a defect free MgO(001) surface. That is why we get a higher transmittance of Ag on an air-cleaved MgO(001) surface than on a UHV-cleaved MgO(001) surface at the same thickness.

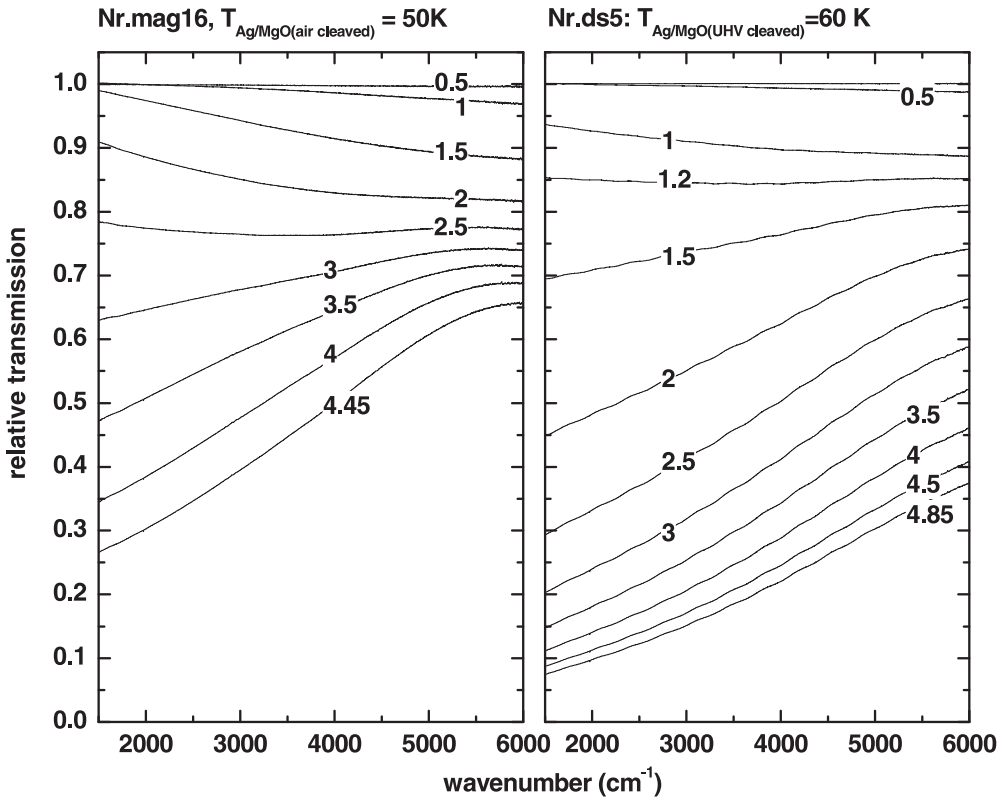

Figure 4.24: Selected relative IR transmission spectra of Ag films grown on: (a) air-cleaved MgO; (b) UHV-cleaved MgO. MgO was cooled with liquid He. The numbers indicate the film thicknesses in nm. In (b) the percolation threshold is reached at a smaller thickness than in (a).

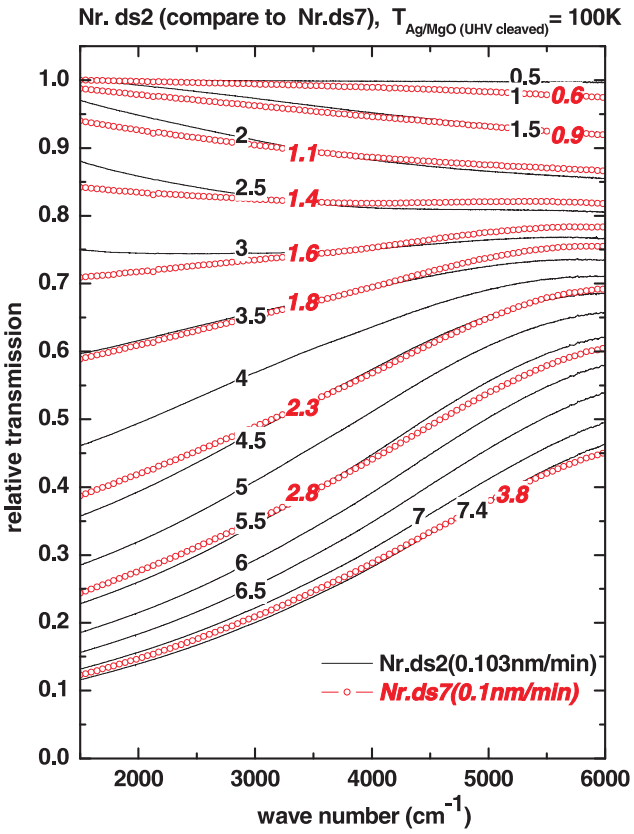

Figure 4.25: Comparison of selected relative transmission spectra from different Ag-film growth experiments. Both films were grown on UHV-cleaved MgO(001) surfaces at about 100 K. The two films are deposited with similar evaporation rates and their spectra are superposable. The big divergence on thickness is due to the misalignment of metal flux with the substrate surface during the growth of film No.ds2. Its thickness should be smaller.

4.2.2 IR Spectra of Ag Films Grown on MgO(001) at about 100 K

The film growth at 100 K on MgO(001) is also reproducible. In Fig. 4.25 we show relative transmission spectra of two films grown on UHV-cleaved MgO(001) surfaces at about 100 K with similar evaporation rates. Although there is a big difference on the corresponding thicknesses, the spectra are well superposable. The big thickness difference is from film No.ds2. The metal flux from the evaporator and the substrate surface was misaligned during the growth of this film. Its real thickness should be smaller.

In Fig. 4.26 we show relative transmission spectra of three Ag films grown at the same temperature (100 K), but with different evaporation rates and on substrates prepared

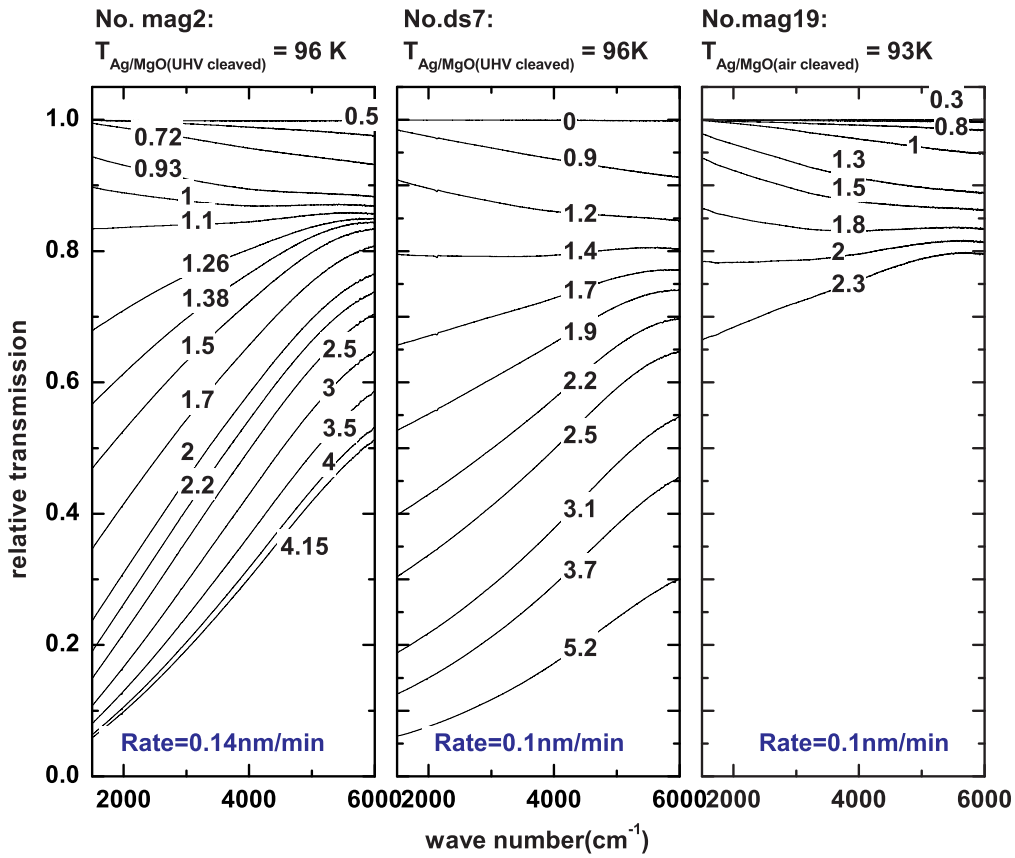

Figure 4.26: Selected relative transmission spectra of three Ag films grown on air- or UHV-cleaved MgO(001) surfaces at about 100 K. The evaporation rate of each film is indicated in the figure.

in different ways. We find a similar phenomenon as we saw on the films grown at 50 K: at the same thickness and the same frequency, the transmittance of a Ag film grown on an air-cleaved MgO(001) surface is higher than that of a film grown on a UHV-cleaved MgO(001) surface. We found the evaporation rate shows an obvious effect also. From Eq. 2.47 we can see, on the basis of the big effect from a low temperature, a small change on the evaporation rate R will affect the density of islands a lot.

4.2.3 Fitted Transmission Spectra of Ag Films Grown on MgO(001) at 50 K and 100 K

As we have dealt with the room-temperature prepared films, we fitted the measured transmission spectra based on the bulk data at low temperatures. The two Drude parameters for Bulk Ag from Ordal [38] at low temperatures are:

$$\omega_{\tau\mathrm{b}} = 16.5\,\mathrm{cm}^{-1} + 0.0386 \cdot \omega, \qquad \omega_{p\mathrm{b}} = 74110\,\mathrm{cm}^{-1} \tag{4.3}$$

for bulk Ag at 60 K, and

$$\omega_{\tau\mathrm{b}} = 37.6\,\mathrm{cm}^{-1} + 0.0386 \cdot \omega, \qquad \omega_{p\mathrm{b}} = 74110\,\mathrm{cm}^{-1} \tag{4.4}$$

for bulk Ag at 100 K. To calculate the spectra of thin films, we still use the two frequency independent but thickness dependent parameters $\omega_{\tau\mathrm{s}}$ and β as fit parameters.

When we perform Drude type fits to the transmission spectra of low-temperature prepared films, we often find that the β values are above unity. This could be due to the uncertainty in the thickness calibration [45]. Thus we tried a fit with thicknesses normalized by an increase of 10% to exclude the uncertainty from thickness calibration. For the two fits we will show in Fig. 4.27 and Fig. 4.28 we use the normalized film thickness.

In Fig. 4.27 (B) the best fitted spectra with the Drude type model of a film grown at about 60 K are shown; in (A), the total relaxation rate ω_τ at 2000 cm^{-1} instead of $\omega_{\tau\mathrm{s}}$, the *deviation* and the scaling factor β for ω_p versus average film thickness are shown. Different from the phenomenon found on the calculation of room-temperature prepared Ag films, the spectra of this cold-deposited film are fitted perfectly only by varying the two thickness-dependent fit parameters $\omega_{\tau\mathrm{s}}$ and β. The total relaxation rate ω_τ due to the surface scattering part $\omega_{\tau\mathrm{s}}$ becomes very big even at the final thickness. Besides the surface roughness, that accounts for the voids and defects in low-temperature prepared films. Due to the big ω_τ, the transition of $\mathrm{Im}\,\varepsilon_{\mathrm{eff}}$ at ω_{max} is not obvious anymore [76]. Thus the spectra are well fitted. At the final thickness, the scaling factor β for ω_p is almost equal to 1, which means the film behaves like bulk silver. The decrease of β with decreasing thickness corresponds to an increase of depolarization fields. An increase of these depolarization fields indicates an increasing amount of tilted surface

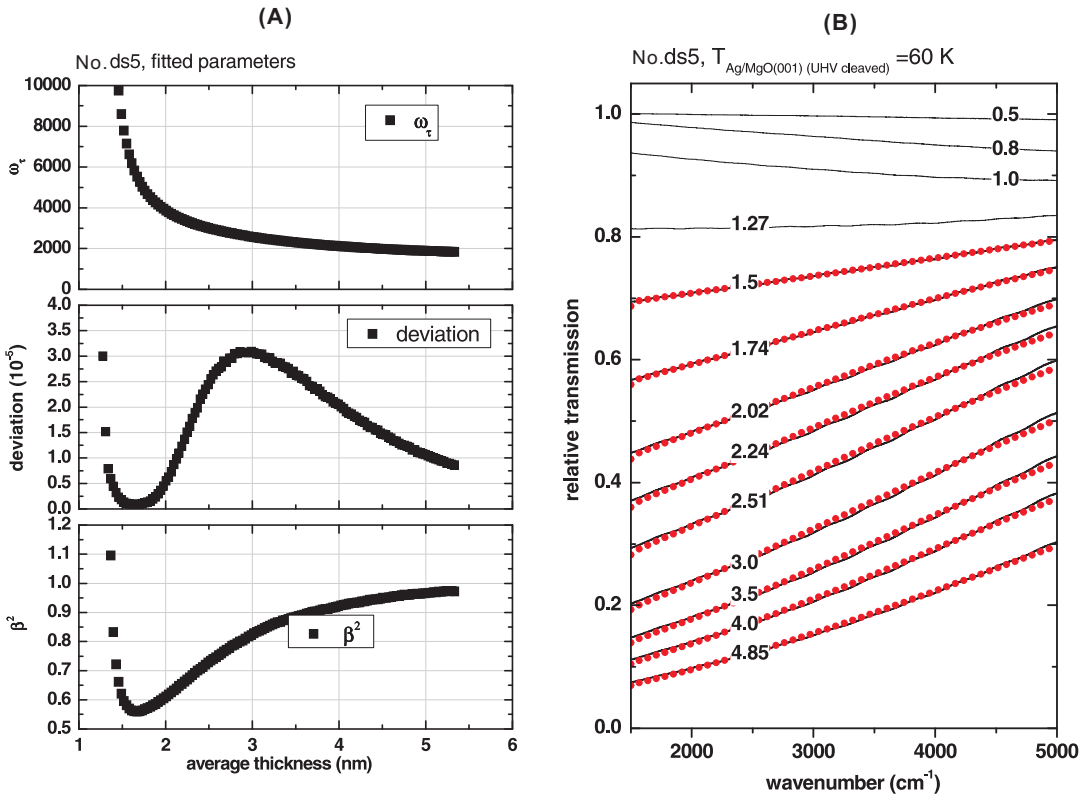

Figure 4.27: Results of a fit to the relative transmission spectra of a film grown on a UHV-cleaved MgO(001) surface at about 60 K with the drude type model. In (A), the total relaxation rate of the film ω_τ at 2000 cm^{-1} instead of $\omega_{\tau s}$, the *deviation*, and the scaling factor β for ω_p versus the average film thickness are shown together; In (B), best fitted spectra (dotted lines) are shown together with the measured ones (solid lines).

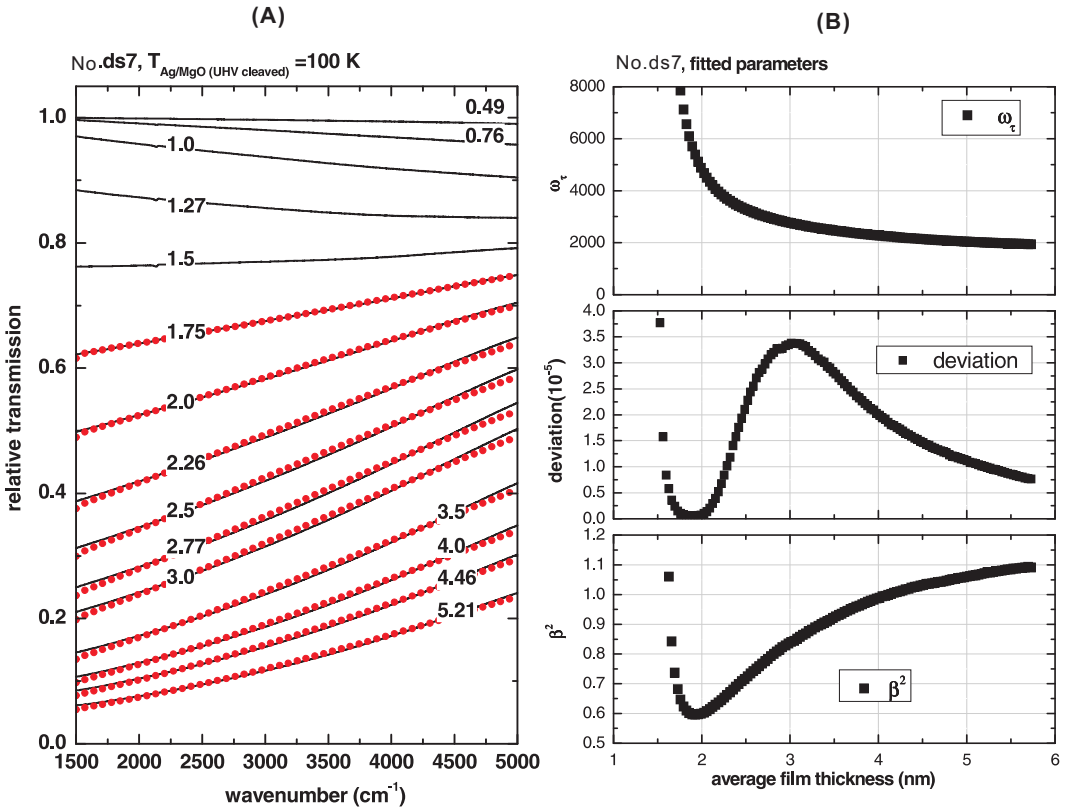

Figure 4.28: Results of a fit to the relative transmission spectra of a film grown on a UHV-cleaved MgO(001) surface at about 100 K with the drude type model. In (A), best fitted spectra (dotted lines) are shown together with the measured ones (solid lines); in (B), the total relaxation rate of the film ω_τ at 2000 cm^{-1} instead of $\omega_{\tau s}$, the *deviation* , and the scaling factor β for ω_p versus the average film thickness are shown together.

Table 4.4: List of experiments performed at high temperatures. The average film thickness is denoted by *d*. "rate" denotes the evaporation rate; "geometry" means the measurement in transmission (T) or in reflection (R) geometry.

	Substrate temperature	Pressure during deposition	Deposition	final thickness	IR Spectroscopy	CO exposure		
Exp	T (K)	P (10^{-10} mbar)	rate (nm/min)	d (nm)	geometry	T (K)	P_{co} (10^{-8}mbar)	geometry
ds6	398	3.8	0.092	32	T	95	3	T
mag10	450	1.7	0.148	29	R	90	8	T
ds8	494	4.4	0.113	40.5	T	96	9	T
mag24	500	20	0.125	33.4	T	93	5	T

area or an increasing long-range roughness amplitude. The steep increase of $\omega_{\tau s}$ at around 1.6 nm indicates the breakdown of the Drude model.

In Fig. 4.28, the calculated results with the Drude type model to the spectra of a film grown at about 100 K are shown. We get similar results as shown in Fig. 4.27. Very big ω_τ and perfectly fitted spectra were obtained. Because the percolation threshold of this film is higher than that of the film No.ds5 shown in Fig. 4.27, the breakdown of the Drude model appears at around 1.9 nm in Fig. 4.28. Although with normalized film thicknesses, the values of β^2 are still above unity at high thicknesses. Fe films grown on MgO also show such kind of increased plasma frequency at a thickness far above the percolation threshold [45]. Further investigations are necessary to explain this.

4.3 Ag Films Prepared at High Temperatures (400 K, 450 K, 500 K)

The sticking probability of Ag on MgO(001) between 100 K and 500 K has been determined by M.-H. Schaffner *et al.* [62]. They found almost a zero probability of Ag atoms staying on a MgO surface at 500 K. However, an epitaxial growth of Ag islands grown on MgO(001) obtained above 500 K has been reported [81]. Additionally we find Ag can adsorb on a MgO(001) surface at 500 K in a probability bigger than zero and also follows an epitaxial growth. In this section we present the IR spectroscopy and AFM studies of Ag films grown on hot MgO(001) substrates. In table 4.4 a list of experiments performed at high temperatures is given, of which the results are shown in this section.

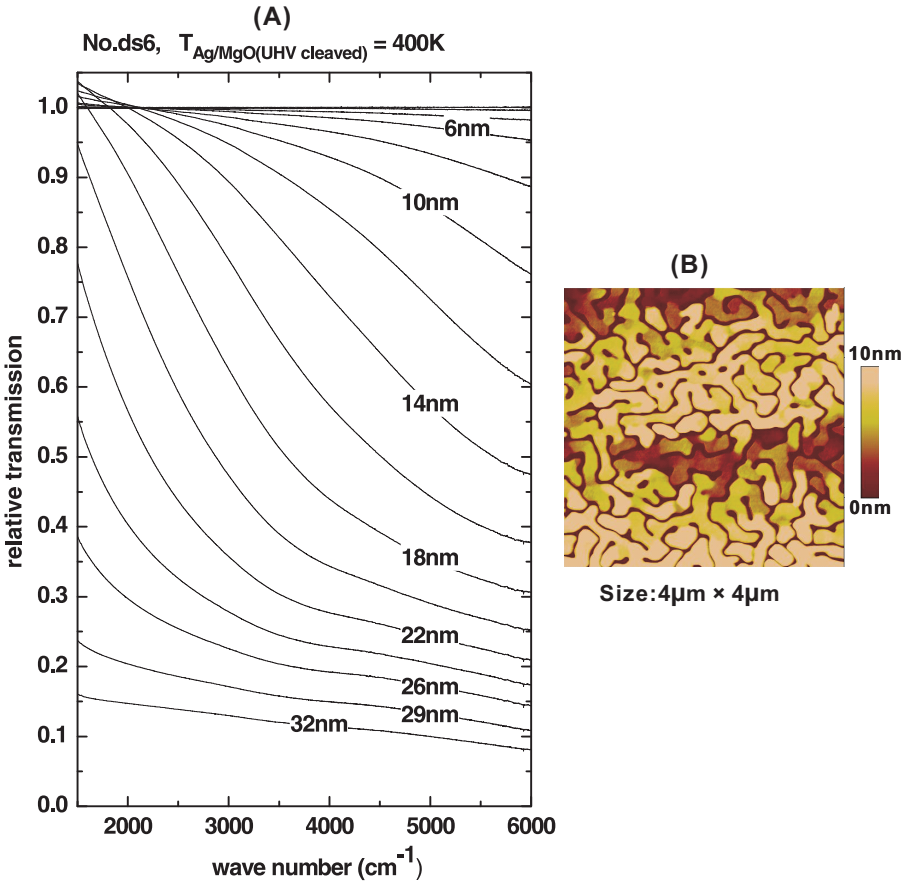

Figure 4.29: (A) IR relative transmission spectra of a Ag film grown on a UHV cleaved MgO(001) surface at about 400 K. The percolation threshold did not appear even at a thickness of 32 nm. (B) The AFM image of this film. The scan size is $4\times4\,\mu m^2$. The structure is very similar but is about 7 times larger than that on the room-temperature prepared film with a thickness near to the percolation threshold.

4.3.1 IR Transmission Spectra of Ag Films Grown on MgO(001)

In Fig. 4.29 (A) we show selected relative transmission spectra of a Ag film grown on a UHV-cleaved MgO(001) surface at 400 K. The average film thickness indicated in the figure is that measured by the quartz microbalance based on the assumption that all the arriving metal atoms will stay on the substrate. Since not all the arriving metal atoms will stay on such a hot surface, the real thickness for this film should be smaller.

The development of the transmittance following the increase of Ag coverage is similar as we found on room-temperature prepared films. Compared with that, the transmittance near the percolation threshold on this film is quite low. That is owing to the never coalesced big islands which can be seen by the AFM image shown in Fig. 4.29 (B).

The AFM image shows a structure corresponding to the percolation threshold. The structure size is about 7 times bigger than that on the room-temperature prepared films.

In Fig. 4.30 (A) and (B), selected relative transmission spectra of two films grown on UHV-cleaved MgO(001) substrates at about 500 K are shown. The spectra of the two films are not superposable probably due to the different base pressure during film growth. At 500 K the sticking coefficient of Ag on MgO is even smaller, so the divergence between the presented thickness in the figure and the real thickness is even bigger.

At high temperatures, as can be seen from Eq. 2.47, the total number of islands is reduced. Consequently big islands will be formed with the increase of Ag coverage. Also Ag adatoms have high mobility, moreover there is a very small lattice mismatch ($< 3\%$) between Ag and MgO, an epitaxial growth is possible. The AFM images of the two films in (A) and (B) are shown in Fig. 4.30 (C) and (D). Very big islands are presented in the images and an epitaxial growth is obvious. Most of the islands are distributed regularly and have a rectangular shape. The edges of the rectangular shaped islands are orientated along the $<110>$ or $<1\bar{1}0>$ direction of the MgO(001) substrate and their surfaces are flat and quite smooth. As we mentioned in § 2.6 the energy barrier for Ag adatoms diffusing on MgO(001) is much smaller when diffusing along the $<110>$ direction than along the $<100>$ direction. This fact results in the rectangular shape of the islands. The epitaxial distribution of the islands is mainly due to the small lattice mismatch between Ag and MgO(001) and the high diffusion rate of Ag adatoms on both MgO and Ag itself at 500 K.

4.3.2 IR Reflection Spectra of Ag Films Grown on MgO(001)

For the convenience of evaporation IR reflection spectra were captured during a Ag film growth on an air-cleaved MgO at 450 K. In Fig. 4.31 we show its relative reflection spectra in (a), and some detailed change of reflectance in a small thickness range in (b). As we found on room-temperature prepared films the spectra have a negative slope at low Ag coverage. The over-100% reflectance at lower wave numbers was also observed, which is due to a shift of the multi-phonon absorption edge of MgO caused by the anti-absorption of certain arrays of islands . The base lines of the spectra are oscillating up and down in a range of 6% due to the instability of the sample position. Because of the small sticking coefficient of Ag adsorbed on MgO at 450 K, we did not reach the minimum reflectance although a large amount of Ag was evaporated.

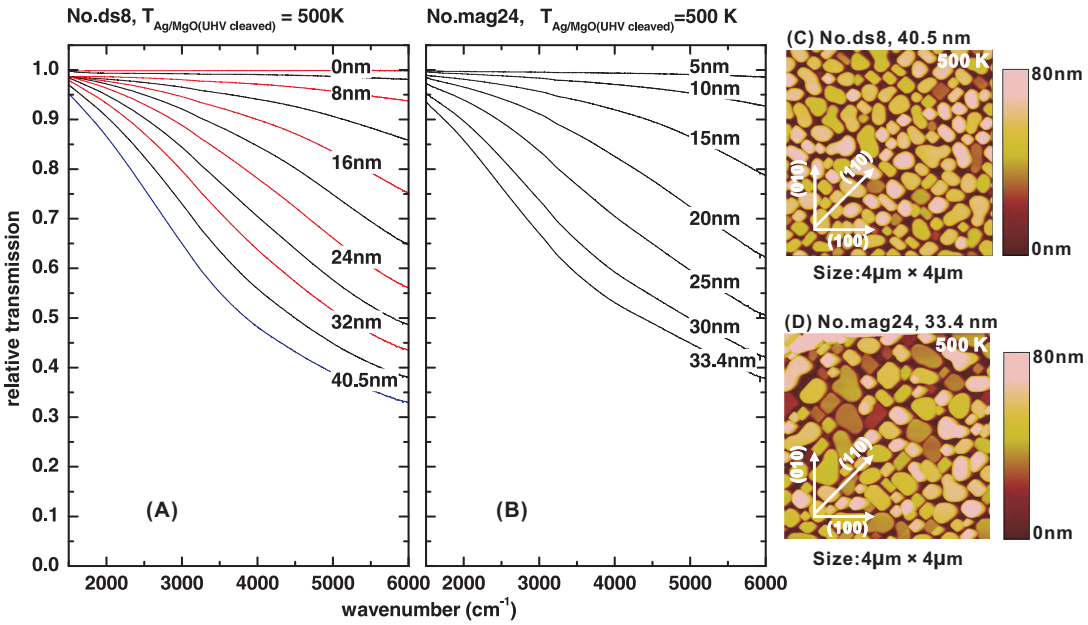

Figure 4.30: (A) Selected IR relative transmission spectra of a Ag film grown on UHV cleaved MgO at 500 K. The base pressure during film growth is below 1×10^{-10} mbar; (B) Selected IR relative transmission spectra of another Ag film grown on UHV cleaved MgO at 500 K. The base pressure during film growth is above 5×10^{-9} mbar; (C)and (D) AFM images of the two films. The scan size is 4×4 μm^2. The inset arrows show the lattice orientation of the MgO(001) substrate.

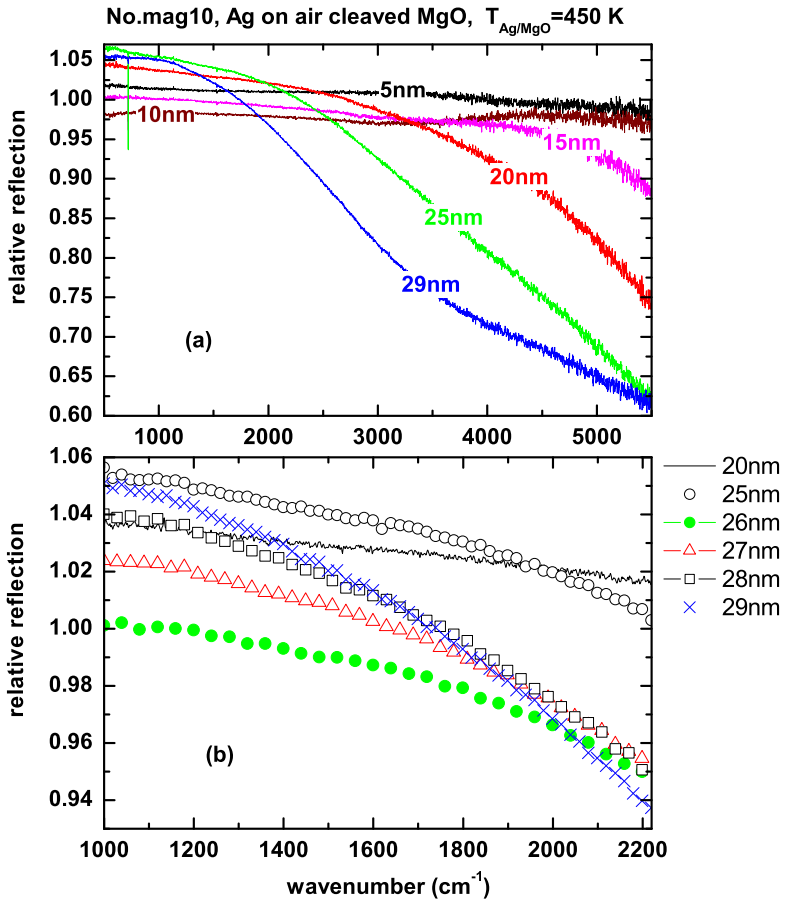

Figure 4.31: (a) Selected IR relative reflection spectra of a Ag film grown on an air cleaved MgO surface at about 450 K. At low wave numbers an anti-absorption effect was observed. Some spectra are shown in (b) in a small spectral range for the purpose of showing some details about the development of the anti-absorption.

Table 4.5: List of experiments for Ag films consisting of small islands performed at room temperature. d denotes the average film thickness; "geometry" means the measurement in transmission (T) or in reflection (R) geometry.

	Substrate temperature	Pressure during deposition	final thickness	IR spectroscopy	CO exposure		
Exp	T (K)	P (10^{-9}mbar)	d (nm)	geometry	T (K)	P_{co}(10^{-8}mbar)	geometry
mag5	299	0.3	1	T	91	3	T
mag25	301	1.9	0.5	T	58	1	T
mag26	299	1.9	0.3	T	56	1.1	T
mag27	303	3	0.2	T	54	1.1	T
mag28	301	3	0.1	T	50	1.1	T

4.4 AFM Images of Ultrathin Ag Films Consisting of Small Islands

In table 4.5 an overview of the experiments of which the AFM images are shown in this section is given.

In Fig. 4.32 we show the AFM images of ultrathin Ag films ($\leq$1 nm) grown on UHV-cleaved MgO(001) surfaces at room temperature. The images (a) to (e) shown in Fig. 4.32 were measured as soon as every sample was taken into air. From Fig. 2.8 we see the total number of clusters keeps increasing until the coalescence process dominates the growth. However, when we count the islands in the AFM images measured we find the total number of islands did not follow the increase of Ag coverage in this way. So we think the film morphologies already changed because of the coalescence of small islands. The smaller the islands are the faster the diffusion is. J. W. Evans [82] reported a fast coalescence ($<$3 hours) of pairs of islands by either corner-to-corner or side-to-side connection.

As we can see from the AFM image of the 0.5 nm Ag film in Fig. 4.32, some uncompleted coalescence of pairs of islands in both ways still exist. The images in the second row of Fig. 4.32 are taken after the film was exposed to air for two or three hours. The first one is for the 0.1 nm film and the second one is for the 0.2 nm film. The islands on the film coalesce fast and rough films were formed.

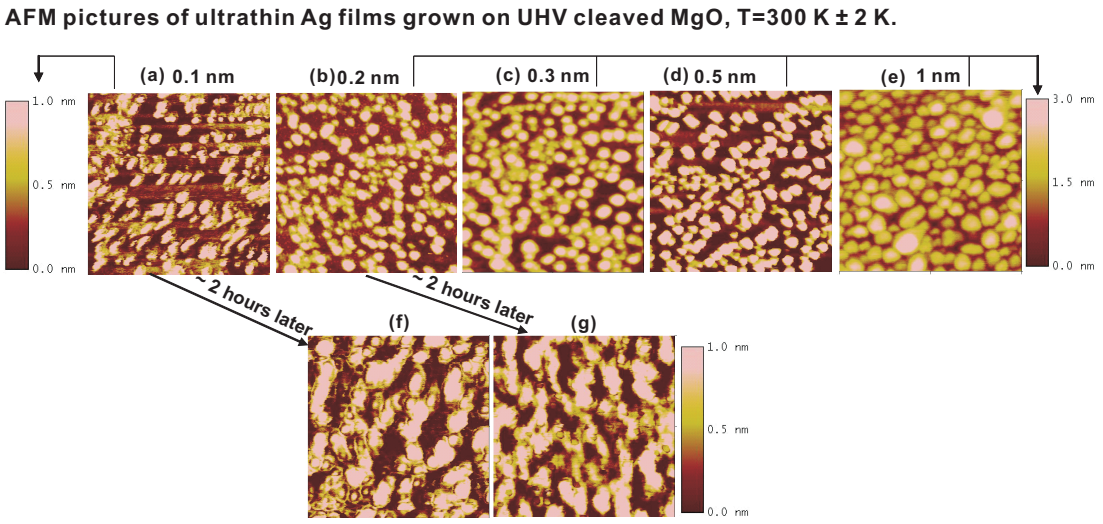

Figure 4.32: AFM images of ultrathin Ag films consisting of small islands. All the films were grown at room temperature. The average film thickness of each film was indicated on the top of the first row of images. The images in the first row were measured soon after the sample were taken out from UHV chamber; the images (f) and (g) in the second row were captured about two hours after (a) and (b) were measured.

4.5 SEIRA of CO Adsorbed on Several Kinds of Ag Films

4.5.1 SEIRA of CO Adsorbed on Cold-deposited Ag Films

Most of the low-temperature prepared films were kept at the preparation temperature and exposed to CO gas. SEIRA spectra of CO adsorbed on these films were measured in situ. All the related Ag films of which we will show the CO sepectra are grown on UHV-cleaved MgO(001) surfaces.

In Fig. 4.33, the relative transmission spectra of CO adsorbed on a 4.85 nm film at 60 K are shown. A single peak appears at 2124 cm^{-1} in the beginning of exposure and shifts to lower frequencies with the increase of CO coverage. At about a dose of 2.7 L CO the peak gets saturated. This is the typical behavior of chemisorbed CO on cold-deposited Ag films.

On the CO spectra of the other two Ag films grown at 100 K, we only see non-shifted peaks. For CO adsorbed on film No.ds2, as shown in Fig. 4.34, the peak locates at 2140 cm^{-1} and saturation features were observed. For CO adsorbed on film No.ds7, as shown in Fig. 4.35 (A), the peak locates at 2124 cm^{-1} and saturation features are also observed. After the valve of gas dosing was closed, this peak disappeared soon. These

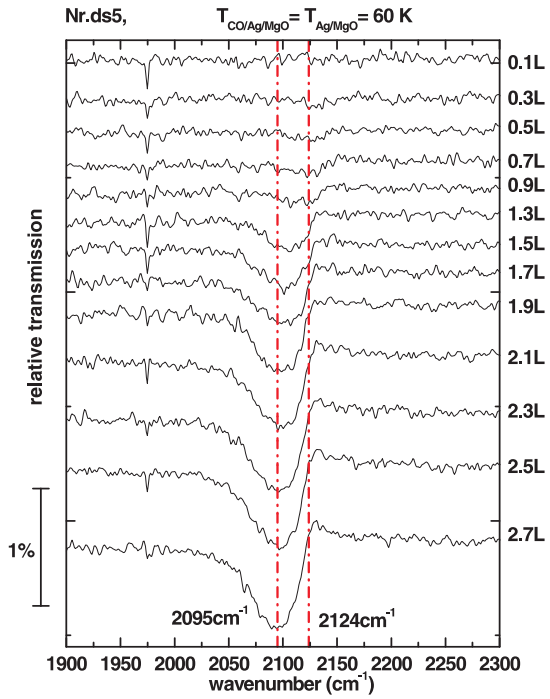

Figure 4.33: SEIRA of CO adsorbed on a 4.85 nm Ag film at about 60 K. The Ag film was deposited at the same temperature. The spectra are vertically shifted.

two peaks at different frequencies were due to physisorbed CO on different facets or on different sites on the same facet.

Incidentally, in Fig. 4.35 (B), we show the AFM image of film No.ds7. To some extent the film shows a flat surface, whereas there are some mild undulations. By IR transmittance studies we have validated that the mesoscopic structure of the film does not significantly change due to a slow annealing process of the film [26]. However, the structure at atomic scale on the island facets was affected, which cannot be resolved with the AFM. Thus owing to the resolving power of AFM, the surface morphology shown by the AFM images measured at room temperature can be approximately considered as that observed at low temperatures.

4.5.2 SEIRA of CO Adsorbed on Small Ag Islands

CO adsorbed on ultrathin Cu films (below 0.3 nm) at about 100 K has been well studied [16]. When Cu was evaporated onto MgO(001) at room temperature, islands were formed. CO adsorbed on these islands at 100 K shows a SEIRA effect. Up to saturation exposure, both the intensity and the frequency of the SEIRA peak are related to the Cu film thickness. Also the amount of exposed CO gas at the saturated spectrum of each film increases with the film thickness because of the increased sites for adsorption. In this work we will show some additional results about CO adsorbed on small Cu islands

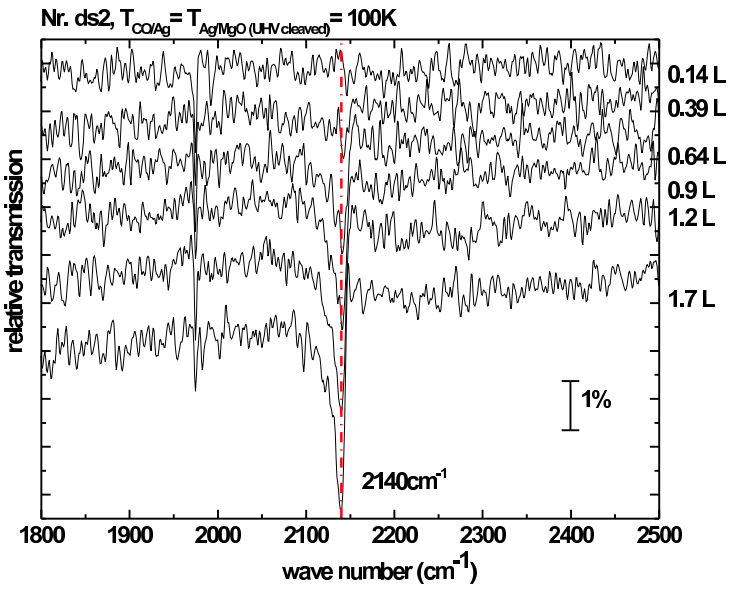

Figure 4.34: Selected relative transmission spectra of CO adsorbed on a 100 K prepared Ag film at the same temperature. The Ag film was grown on a UHV cleaved MgO(001) surface. The spectra are vertically shifted.

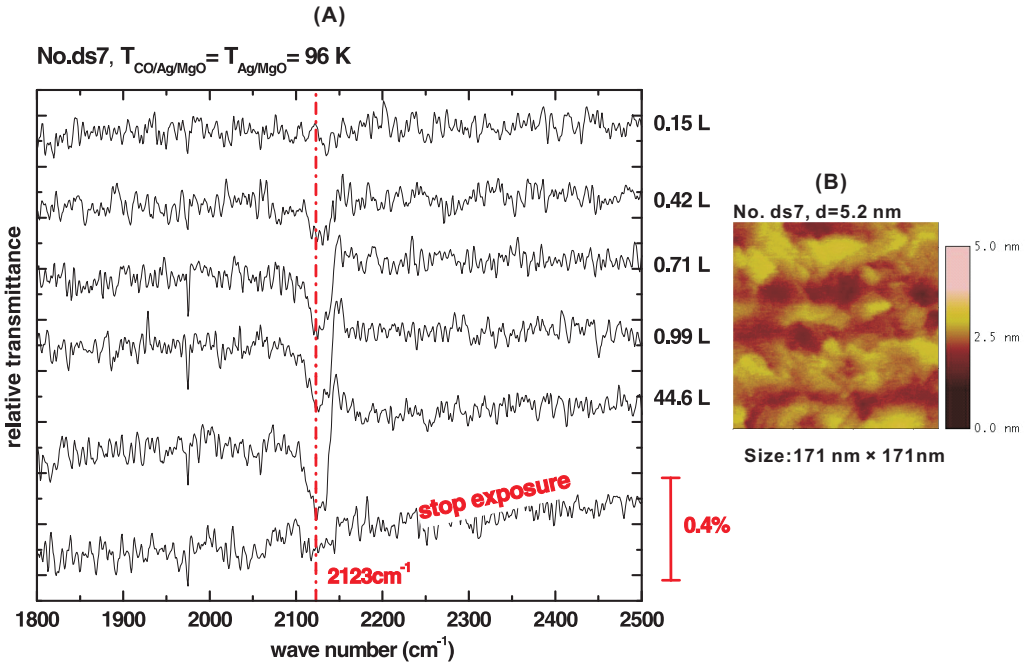

Figure 4.35: (A) Selected relative transmission spectra of CO adsorbed on a 100 K prepared Ag film No.ds7 at the same temperature. The Ag film is 5.2 nm thick and is grown on a UHV cleaved MgO(001) surface. (B) The AFM image of this film was taken at room temperature in air. The scan size is $170 \times 170\,\mathrm{nm}^2$.

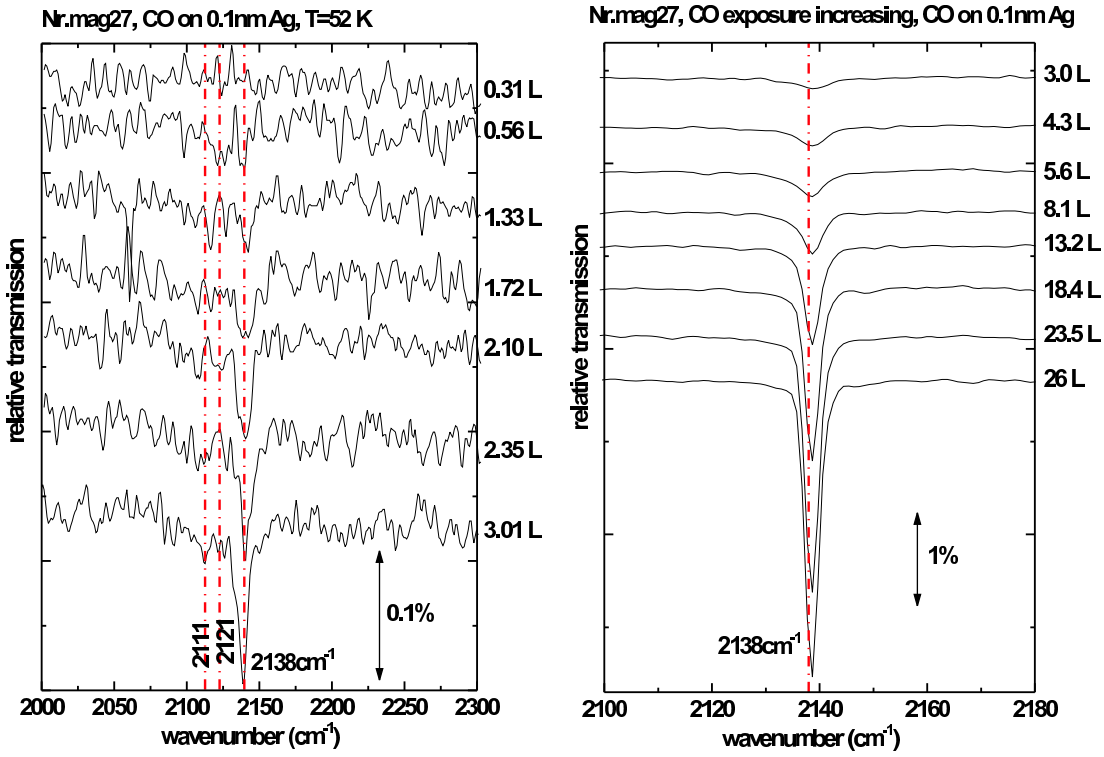

Figure 4.36: SEIRA of CO adsorbed on a 0.1 nm Ag film prepared at room temperature on a UHV cleaved MgO(001) surface. The base pressure in the UHV chamber is around 3×10^{-9} mbar. In (A) the CO peak appears at 2121 cm^{-1} first then shifts to 2111 cm^{-1} following the increase of CO coverage. The peak appears later at 2138 cm^{-1} accounts for the CO adsorbed on MgO. In (B) the growth of peak 2138 cm^{-1} following the increase of CO coverage was shown and no saturation was found at the end of exposure.

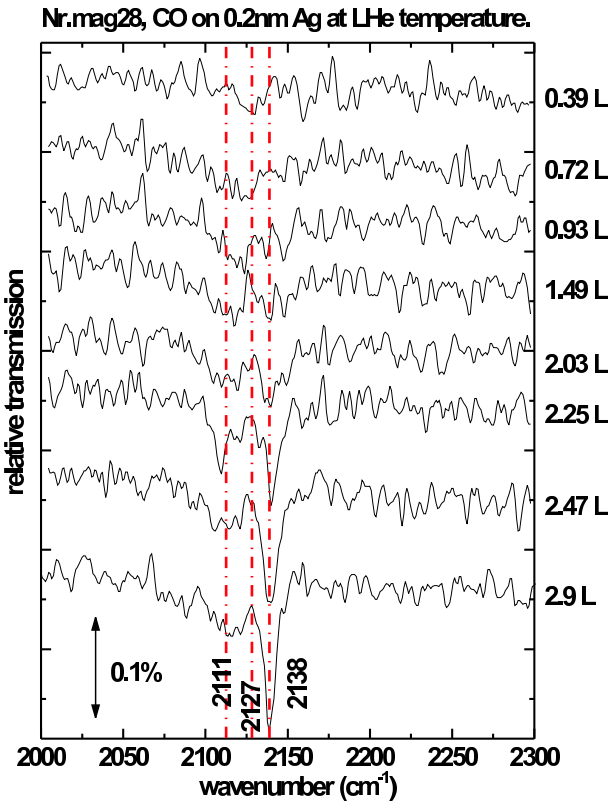

Figure 4.37: SEIRA of CO adsorbed on a 0.2 nm Ag film at about 50 K. The Ag film was prepared at room temperature on a UHV cleaved MgO(001) surface. The base pressure in the UHV chamber was about 3×10^{-9} mbar. The CO peak appears at 2127 cm^{-1} first then shifts to 2112 cm^{-1} following the increase of CO coverage. The peak appears later at 2138 cm^{-1} accounts for CO adsorbed on both the Ag and the MgO surface.

in § 5.4.1. Ag films grown on MgO(001) at room temperature at low coverage also show separated islands. As we mentioned in § 2.6, the diffusion barrier and adsorption energy of Cu on MgO are much higher than that of Ag on MgO. At the same temperature, compared with the same amount of deposited Cu (very low coverage), from Eq. 2.46 we know the total number of Ag islands will be less than that of Cu. In Fig. 5.1 we can directly see that from AFM images. The total number of Cu islands per unit area of a 0.5 nm Cu film is about 6 times that of a same thick Ag film, i.e., the average size of Ag islands is about 6 times of that of Cu islands. Thus a study of adsorption of CO on very small Ag islands as that on Cu would need Ag deposited on a cooled sample. At room temperature the islands already show the CO frequency close to that on an extended surface.

Some ultrathin Ag films grown on UHV-cleaved MgO(001) surfaces at room temperature, of which the AFM images were shown in Fig. 4.32, were cooled down with liquid Helium to about 50 K and exposed to CO gas. Simultaneously relative IR spectra were

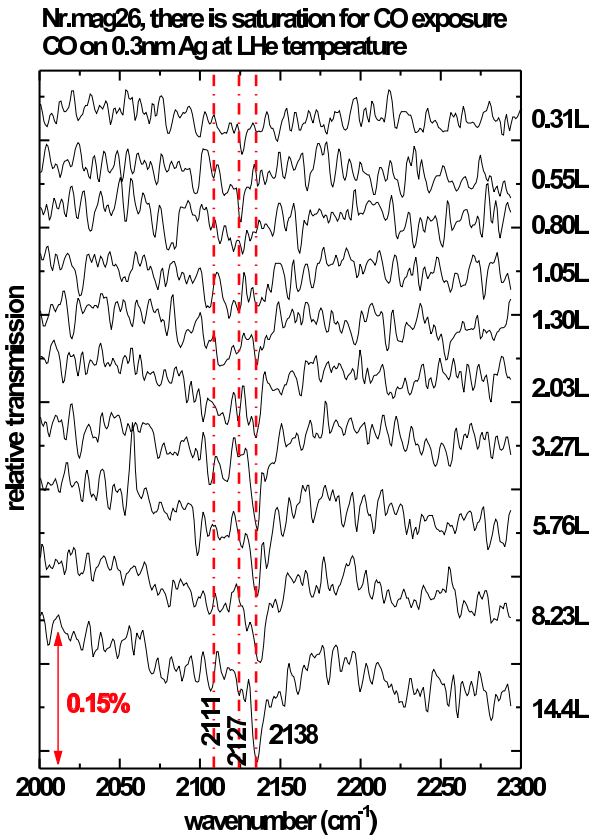

Figure 4.38: SEIRA of CO adsorbed on a 0.3 nm Ag film at about 50 K. The Ag film was prepared at room temperature on a UHV cleaved MgO(001) surface. The base pressure in the UHV chamber is about 3×10^{-9} mbar. The CO peak appears at 2127 cm^{-1} first then shifts to 2111 cm^{-1} following the increase of CO coverage. The peak appearing later at 2138 cm^{-1} accounts for CO adsorbed on both the Ag and the MgO surface.

measured in transmission geometry.

In Fig. 4.36 to Fig. 4.39, the SEIRA spectra of CO adsorbed on Ag films ranging from 0.1 nm to 0.5 nm are shown. On the CO spectra of most films a peak at around 2127 cm^{-1} appears first, then shifts to 2111 cm^{-1} with the increase of CO coverage. Later on, another sharp peak at 2138 cm^{-1} appears. On some films it becomes (on the 0.3 nm film) saturated at higher exposure, but on the other films (on the 0.1 nm, 0.2 nm and 0.5 nm films) it keeps increasing with the CO dose without getting saturated. Knowing from the literature studies as we listed in the beginning of this section, the peak at 2127 cm^{-1} should be due to chemisorbed CO. This means we have some atomic scale roughness on the film surface. The sharp peak is due to a physisorbed species. The appearance of this peak could be a result of two facts. First it could be due to CO adsorbed on MgO(001) surface. We have checked that CO adsorbed on an air cleaved MgO(001) surface at the same temperature also shows a peak at the same frequency. Second we might get some ordered sites on a room temperature prepared Ag film.

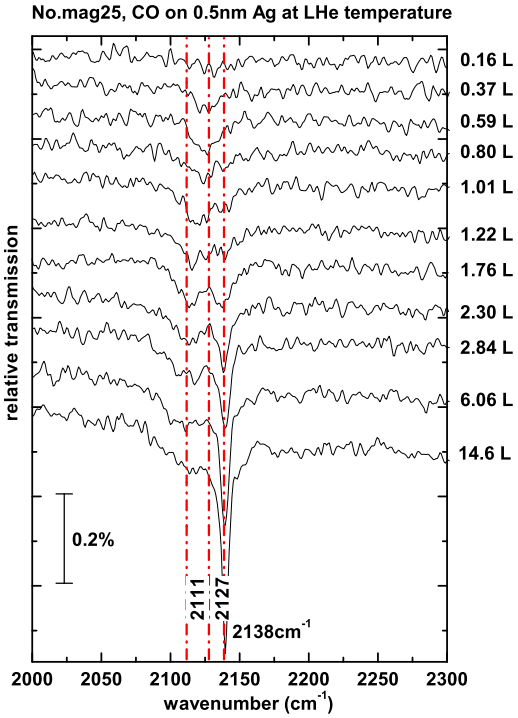

Figure 4.39: SEIRA of CO adsorbed on a 0.5 nm Ag film at 50 K. The Ag film was grown on a UHV cleaved MgO surface at room temperature. One CO peak appears at 2127 cm^{-1} first, then shifts to 2111 cm^{-1} following the increase of CO coverage. The peak appearing later at 2138 cm^{-1} accounts for CO adsorbed on both the Ag and the MgO surface.

However, the ongoing increase of the peak is due to CO condensed on the MgO(001) substrate. On the 0.3 nm Ag film we find this peak gets saturated. Since we are at the temperature edge where CO easily desorbs from MgO, the saturated peak could be ascribed to a physisorbed species only on Ag at a little bit higher temperature.

On some films, the SEIRA spectra of adsorbed CO shows two vibrational bands. We collect the last SEIRA spectrum of CO adsorbed on each film, on which the peak due to physisorbed species did not appear yet together in Fig. 4.40. On these spectra, every peak due to chemisorbed CO shows saturation. We did not find a thickness dependent frequency of CO as we find on Cu (see § 5.4.1). The peak intensity becomes high following the increase of Ag coverage.

On a thicker film (1 nm) the CO spectra are distinct: six peaks were found after a large dose of CO. The peak at 2059 cm^{-1} could be due to chemisorbed CO on defects or on a bridge side of the metal lattice. The two very broad peaks at 1643 cm^{-1} and 3213 cm^{-1} should be due to contamination. The other two narrow peaks at 2122 cm^{-1} and 2142 cm^{-1} are due to physisorbed CO on different facets or on different sites of the same facet. The very tiny peak at 2341 cm^{-1} arises from the asymmetric stretching

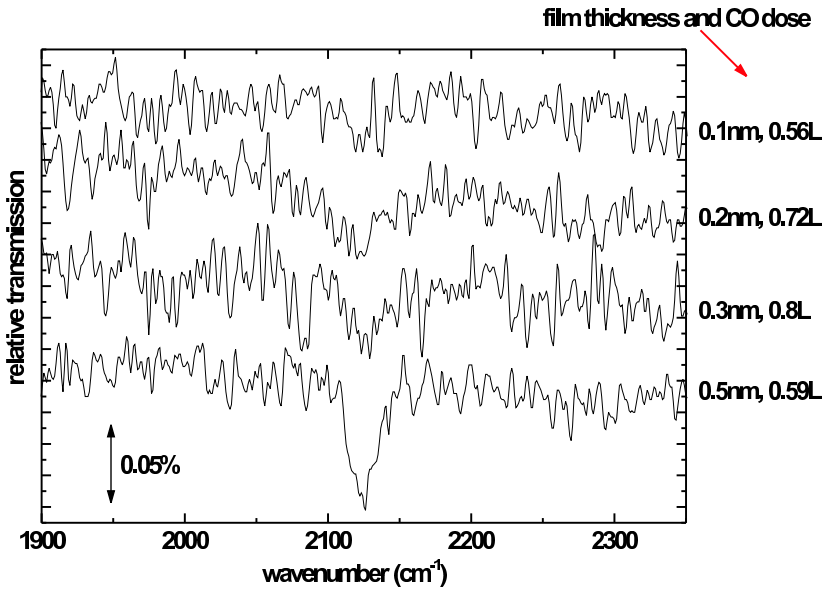

Figure 4.40: Collection of SEIRA of CO on small Ag islands at saturation dose as described above.

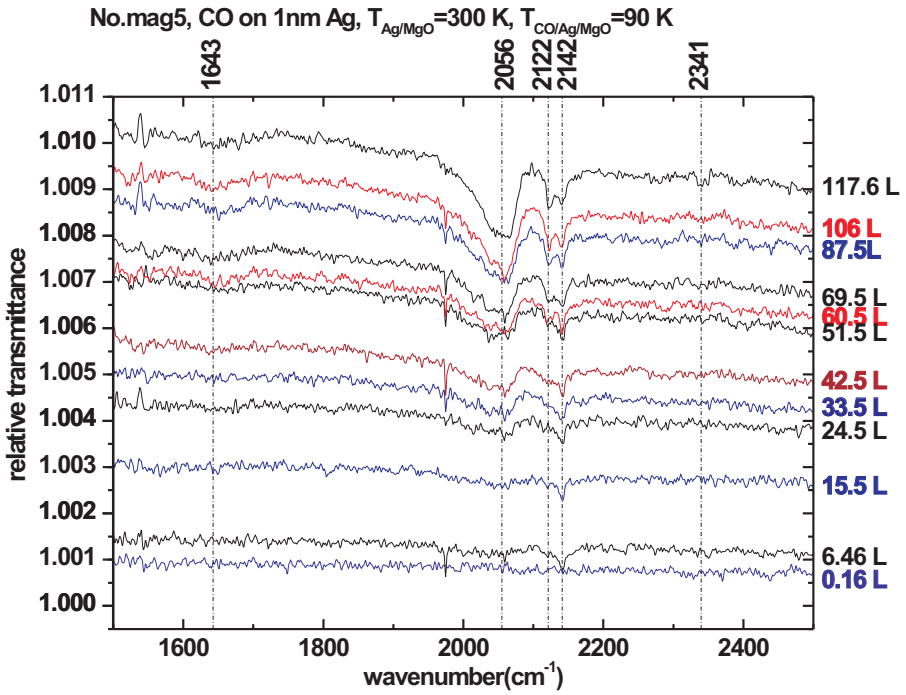

Figure 4.41: SEIRA of CO adsorbed on an 1 nm Ag film at about 90 K. The spectra were shown as measured. The Ag film was prepared on a UHV cleaved MgO surface at 300 K. The multi-peaks will be found also when CO adsorbs on thicker Ag films prepared at 300 K.

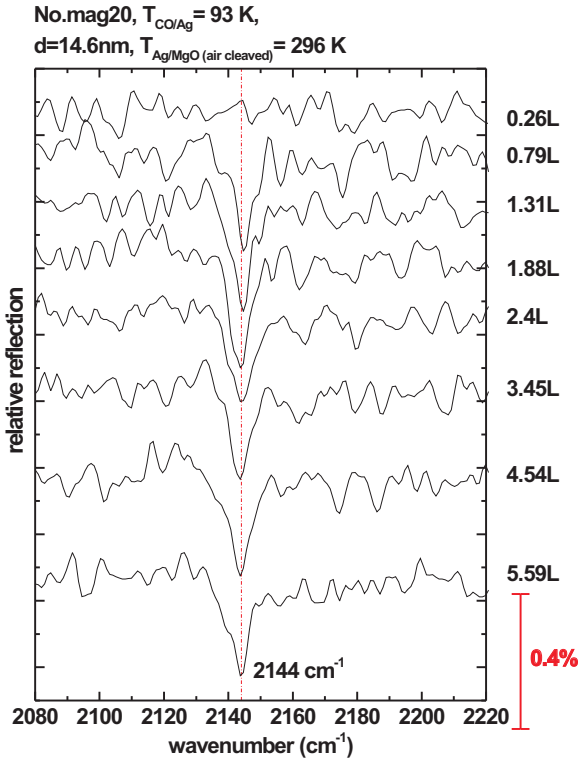

Figure 4.42: IRRS (IR reflection spectra) of CO adsorbed on a 14.6 nm Ag film (Nr.mag20) at about 100 K. The film was prepared at 300 K on air cleaved MgO and the spectra captured during evaporation are shown in Fig. 4.18. Spectra were also captured in normal transmission geometry when CO was exposed to the film at 100 K and no signal was observed.

of adsorbed CO_2. It seems that an 1 nm film already shows polycrystalline properties. We will see all these peaks again when CO adsorbed on thick Ag films grown at 300 K with a structure corresponding to the percolation threshold at 100 K. There a detailed explanation will be given.

4.5.3 SEIRA of CO Adsorbed on Smooth Ag Films Prepared at Room Temperature

The AFM images of very thick Ag films show a very flat surface including some rectangular holes (see Fig. 4.2 (B), and image (3) and (4) in Fig. 4.1 (B)). No CO vibration and base line shift were observed on them by measuring in transmission geometry. However, on films with thicknesses close to the percolation threshold, whose AFM images show big seperated sinuous structures (for example, see image (1) and (2) in Fig. 4.1), multi-CO vibration peaks were found.

On a 6.4 nm Ag film (No.mag1), of which the AFM image is shown as image (3) in Fig. 4.1, no CO signal was found by measuring in transmission geometry when CO was exposed to it at about 100 K. There are two possibilities for what we observed. The first one is that CO may not adsorb on such a surface at 100 K. The second one is that all the bonds of CO molecules are oriented to the normal direction of the very smooth Ag surface so that we cannot detect them in normal transmission. For the second case we can perform a measurement in oblique reflection geometry to find out.

In Fig. 4.42 we show the reflection spectra of CO adsorbed on a very thick and smooth film (No.mag20) at 94 K. On this film at the same temperature we did not detect a CO signal when measuring in transmission geometry. The intensity of the peak shown in the figure is very weak. It seems that there is almost no atomic scale roughness and no enhancement. Now it is clear that CO molecules adsorb on very smooth Ag films with all the bonds oriented to the metal surface normal direction.

4.5.4 SEIRA of CO Adsorbed on Ag films Showing Big Separated Islands

4.5.4.1 SEIRA of CO Adsorbed on Room-temperature Prepared Ag Films Near the Percolation Threshold

On Ag films with thicknesses near the percolation threshold, of which the AFM images show big sinuous structures, we find strong SEIRA of CO at about 100 K. Below in Fig. 4.43 (A), Fig. 4.44, Fig. 4.45 (a), and Fig. 4.46 we show the SEIRA spectra of CO adsorbed on such films measured in normal transmission geometry in the sequence of increasing film thickness. On such kind of films we frequently observe six vibration peaks. We number them as 1 to 6 following the increase of their frequencies. From film to film the peaks shift a little bit. We collect all the peak frequencies from these five films and put them in table. 4.6. Peak No.1 at around 1640 cm^{-1} and No.2 at around 2030 cm^{-1} are all broad so their frequencies are not so critical. As we just mentioned, CO adsorbs on a smooth Ag surface with all bonds orientated to the surface normal, so the signal we measured is due to the CO adsorbed on the side walls of the big sinuous structures.

When CO was exposed, all the peaks did not appear at the same time. There is a sequence for the appearance of every peak. It helps to understand easily if we have a plot of the changing intensity of every peak versus the CO dose. In order to get that we choose some points which do not change much relative to the 100% line in the spectra as reference, then subtracts the lowest transmittance of the stretching peak by the transmittance of one choosed point, the absolute peak-height scaled to 100% is achieved. Certainly there is some approximation because the lowest transmittance of a peak usually shifts a little bit with increased gas exposure whereas we take the frequency of the peak at the final dose as the peak position through all the measured spectra. In Fig. 4.43 (B), Fig. 4.45 (b) and Fig. 4.47, we show such kind of plots for CO

Table 4.6: Statistics of the frequency of the vibrational peaks measured when CO was exposed to rough Ag films grown at room temperature. We number all peaks as 1 to 6 following their increasing vibration frequencies. The unit of the peak frequency is cm^{-1}. The UHV is kept by an ion getter pump together with a TSP when these experiments were performed.

Figure	Film	T_{film}	d(nm)	T_{CO}	geometry	1	2	3	4	5	6
Fig. 4.43 (A)	No.mag4	300 K	3.4	100 K	T	1622	2029	2069	2120	2135	2332
Fig. 4.44	No.mag11	300 K	3.64	100 K	T	1636	2030	2071	2123	2136	2331
Fig. 4.45 (a)	No.mag7	300 K	5.23	100 K	T	1673	2041	2072	2123	2139	2334
Fig. 4.46 (a)	No.mag3	300 K	5.3	100 K	T	1674	2040	2072	2123	2135	2331
Fig. 4.46 (b)	No.mag13	300 K	5.43	100 K	T		2030	2071	2123	2135	2331

adsorbed on film No.mag4 (see Fig. 4.43 (A)), film No.mag7 (see Fig. 4.45 (a)) and film No.mag3 (see Fig. 4.46 (A)). From these plots we can easily see the appearing sequence of the peaks and their later developments.

Let us take the SEIRA of CO adsorbed on film No.mag4 shown in Fig. 4.43 as an example. From the plots of intensity development or the series of SEIRA spectra we can see that peak No.5 at about 2135 cm^{-1}always appears as the first one and shows saturation structure at a low exposure. From literature we know this peak is due to monolayer physisorbed CO on which almost no shift was observed. The peak has a Fano-line shape [83, 84], which is asymmetric and is an indication of a rough surface. The extent of asymmetry indicates how rough the surface is. At the percolation threshold the asymmetry reaches its maximum. After exposing a small dose of CO this peak becomes saturated. After that, following the increase of exposure its intensity starts to decrease and at the same time the sharp peak No.4 appears at 2120 cm^{-1} as a shoulder of it. Later the intensity of the peak at 2135 cm^{-1} becomes smaller and smaller. On some films, it even disappears after a dose of hundreds of L of CO. On the contrary, the intensity of No.4 at 2120 cm^{-1} keeps increasing and no saturation was observed.

The broad peak No.2 at about 2030 cm^{-1} appears after No.5 and before No.4. This peak was not reported in literature yet. Because it is broad and at a low frequency it could be due to CO chemisorbed on defects and polycrystalline sites, or CO bonds to a bridge side of a metal lattice [15].

Another sharp peak No.3 at 2069 cm^{-1} appears almost at the same time as No.4 at 2120 cm^{-1}. It is a shoulder of No.2 at 2030 cm^{-1}. Both No.3 and No.4 are sharp and their intensity increases with exposure without getting saturated and without shifting. All these properties indicate multi-layer physisorbed species. There are different possibilities about the existence of these two peaks. First it could be CO molecules adsorbed on different ordered facets or on different sites of the same facets [53]. A band due to CO adsorbed on Ag(110) was found at 261±4 meV (2105±32 cm^{-1}) by EELS [51]. Because of the low resolution of EELS we cannot relate this peak to any one of

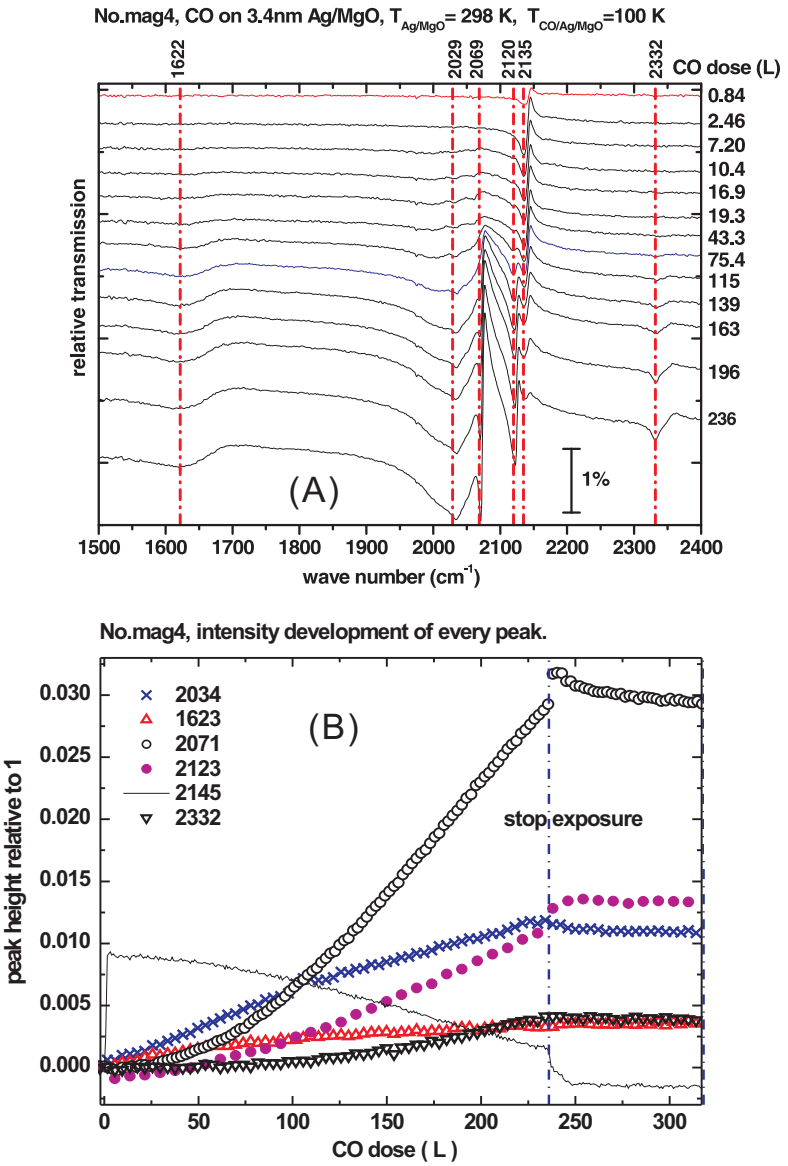

Figure 4.43: (A) SEIRA spectra of CO adsorbed at about 100 K on a room-temperature prepared film with a thickness (3.4nm) near to the percolation threshold. The spectra are normalized and vertically shifted. The position of every CO peak is indicated at the top of every erect dot-dashed line, and also the dosage of CO gas for every spectrum is given in a unit of L (1L=1×10^{-6} Torr·s) at the right side .
(B) Intensity development of every peak found in (A) versus dose of CO after the CO gas exposure was started. The erect line indicates the moment when CO exposure was stopped. The doses shown at the right side of the erect line have no physical meaning anymore but are only a hint of elapsed time.

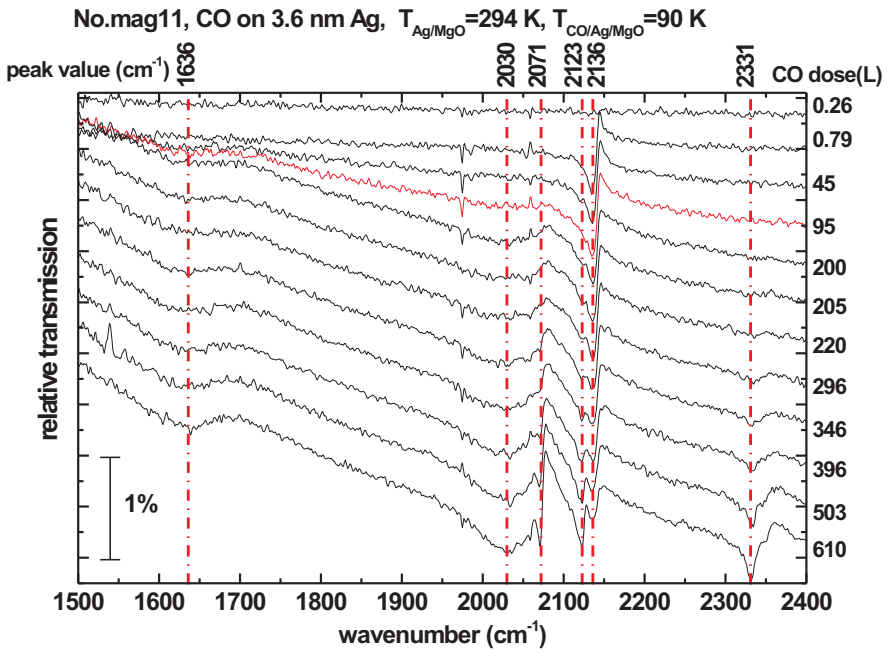

Figure 4.44: SEIRA of CO adsorbed on a 3.64 nm thick Ag film at about 100 K. The film was prepared at 300 K on a UHV cleaved MgO(001) surface.

what we found. Second because they appeared later, it could be due to a reorder of already adsorbed CO molecules [9, 10].

After a dose of 20 to 50 L of CO, the last two peaks appeared as No.1 around 1640 cm^{-1} and No.6 around 2331 cm^{-1}. No.6 is assured to be the asymmetric stretch of adsorbed CO_2 molecules. No.1 could be the condensed Carbon which is often found on a Raman spectrum of metal film as contamination. The appearance of these two peaks is amazing not only because their inexistence in the gas source but also because of the adsorption of CO_2 on Ag at such a high temperature. There are a few possibilities about their appearance. The first possibility is a Boudouard reaction $CO + CO \rightarrow CO_2 + C$ happened among adsorbed CO molecules. We clearly find this type of reaction always (also on Ag films grown at 400 K and 500 K) on Ag island films showing small and deep grooves but not on the cold-deposited films and not on the films well beyond the percolation threshold, for example not on the smooth film grown at 300 K mentioned above (on which no CO signal was found by measuring in transmission geometry). This reaction is observed at only 100 K, which is a very low temperature for the Boudouard reaction [85] and the understanding of that needs more experimental and theoretical work.

Another possibility is the CO_2 comes from the tiny contamination in CO gas source. The CO_2 peak only appears after long time exposure and the absorption of CO_2 on such kinds of films was strongly enhanced. The adsorption of CO_2 could also be morphology sensitive. We excluded the possibility that CO comes from the residual gas by measuring long time on a fresh cooled Ag film prepared at room temperature. The thickness of this film is near to the percolation threshold. The peak No.1 could be due to some contamination on the surface.

On the other four films, we find the appearance of the six peaks following the same sequence. The frequency of every peak is varied a little on films with different thicknesses.

In Fig. 4.43 (A) and Fig. 4.47, at the moment that the CO exposure was stopped, the intensity of peak No. 3 at 2072 cm^{-1} jumped to a high value. This phenomenon is not found in Fig. 4.45. The reason remains unclear.

CO_2 Adsorbed on a Ag Film Surface at about 100 K

As mentioned above, we always get a peak for the CO_2 asymmetric stretch mode [52] when CO gas was exposed to Ag films at 100 K. We made a test by exposing CO_2 gas directly to the Ag films to see how CO_2 adsorbs on Ag films. In Fig. 4.48, SEIRA of CO_2 adsorbed on a 3.94 nm Ag film at about 100 K is shown. The peaks are at the same position as we find on the SEIRA spectra of CO. The Ag film is not fresh. Just after it was prepared on a UHV cleaved MgO(001) surface at room temperature, it was cooled down to about 50 K and exposed to N_2 gas; on the second day, after it was warmed up naturally to room temperature, it was cooled down again but to about 100 K and was exposed to CO_2 gas. The enhancement of CO_2 absorption ascribes to

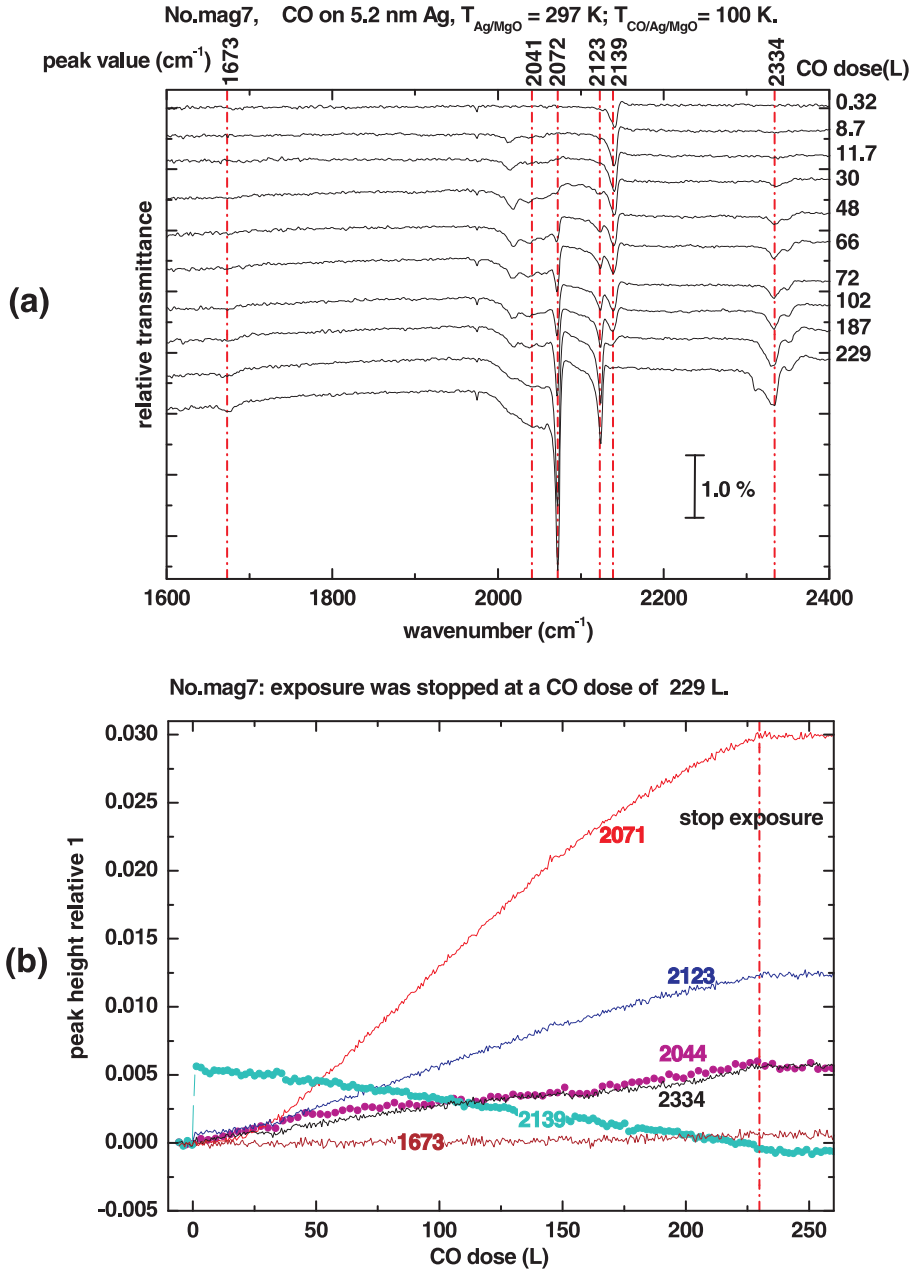

Figure 4.45: (a) SEIRA of CO adsorbed on a 3.64 nm thick Ag film at about 100 K. The film was prepared at 300 K on a UHV cleaved MgO(001) surface in a CO gas surrounding at a pressure of 4×10^{-8} mbar.
(b)Intensity development of every peak found in (a) versus dose of CO after the CO gas exposure was started. After 230 L dose of CO the exposure was stopped. The doses above 230 L shown on the axis have no physical meaning but are only a hint of elapsed time.

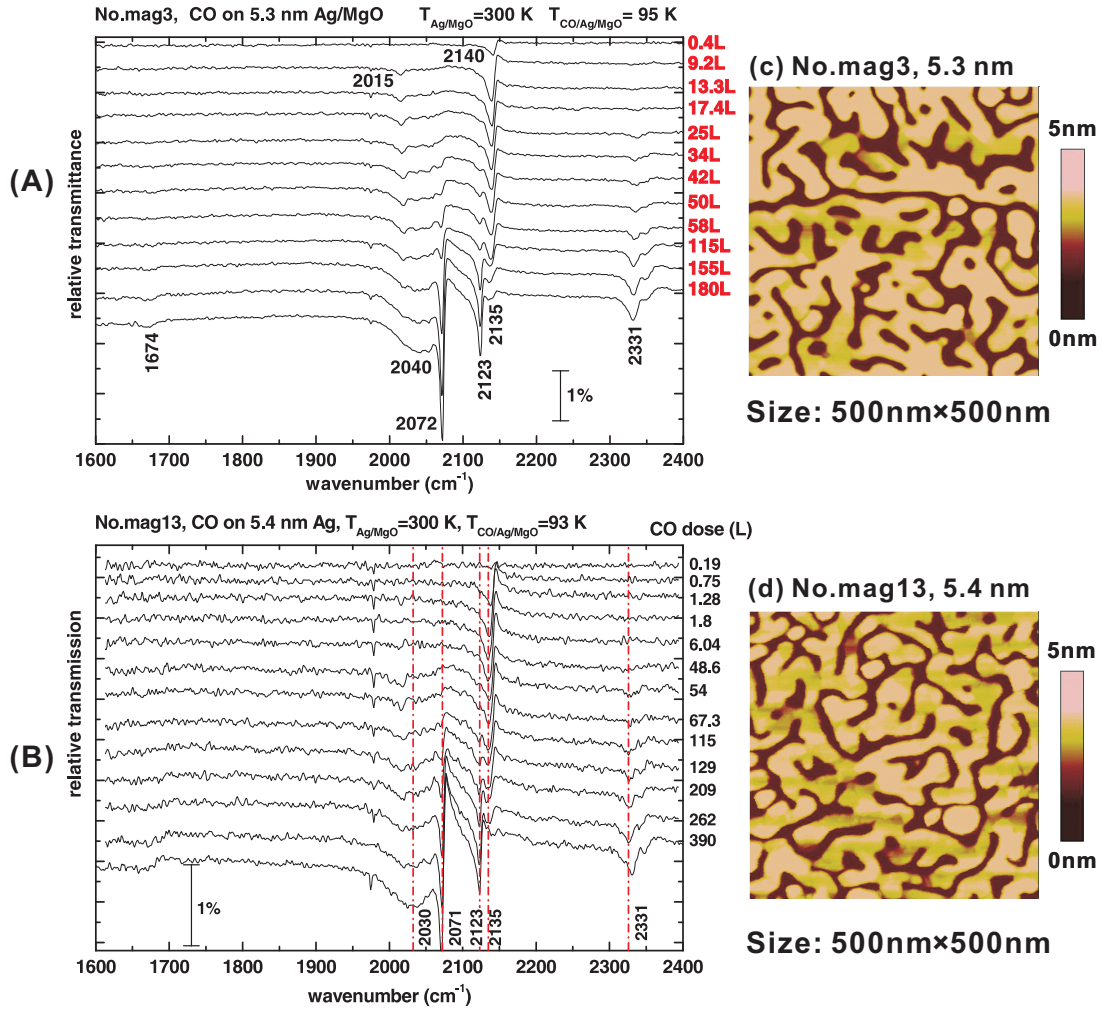

Figure 4.46: (A) SEIRA spectra of CO adsorbed on a 5.3 nm thick Ag film at about 100 K. The film was prepared at 300 K on a UHV cleaved MgO(001) surface and the AFM image of which shows sinuous structures (see (c)).
(B)SEIRA of CO adsorbed on a 5.4 nm thick Ag film at about 100 K. The film was prepared at 300 K on a UHV cleaved MgO(001) surface. The AFM image of it also shows sinuous structures (see (d)).

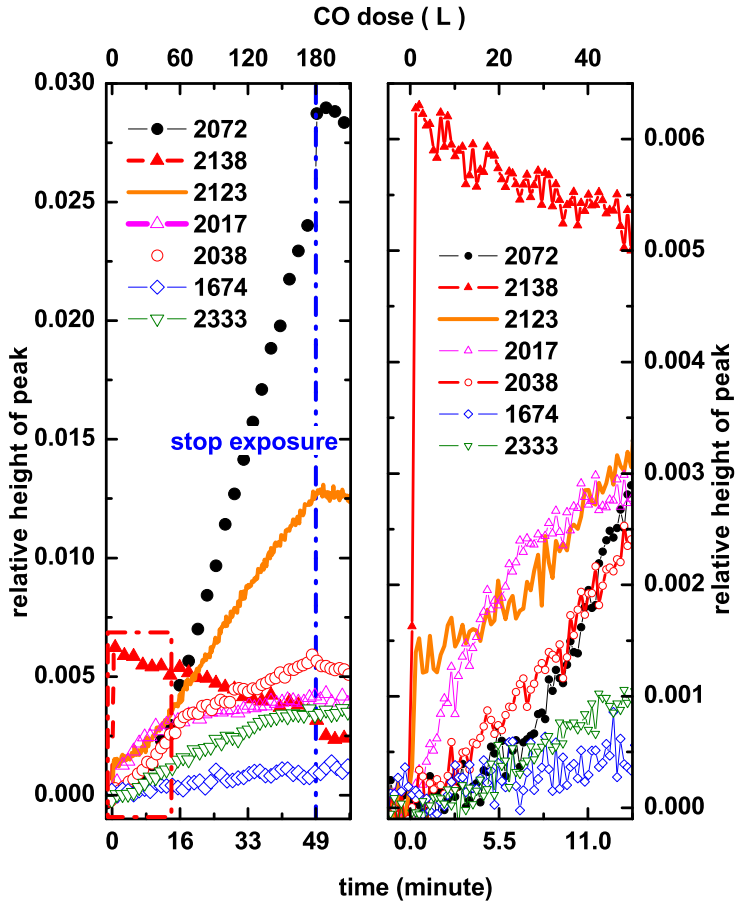

Figure 4.47: Intensity development of every peak found in Fig.4.46 (a) versus the elapsed time after the CO gas exposure was started. In the figure at the left side the development is shown till the exposure was stopped for some time. The dashed erect line indicates the moment at which the exposure was stopped. The area that the dashed line box indicates is shown again in a bigger scale in the figure at the right side.

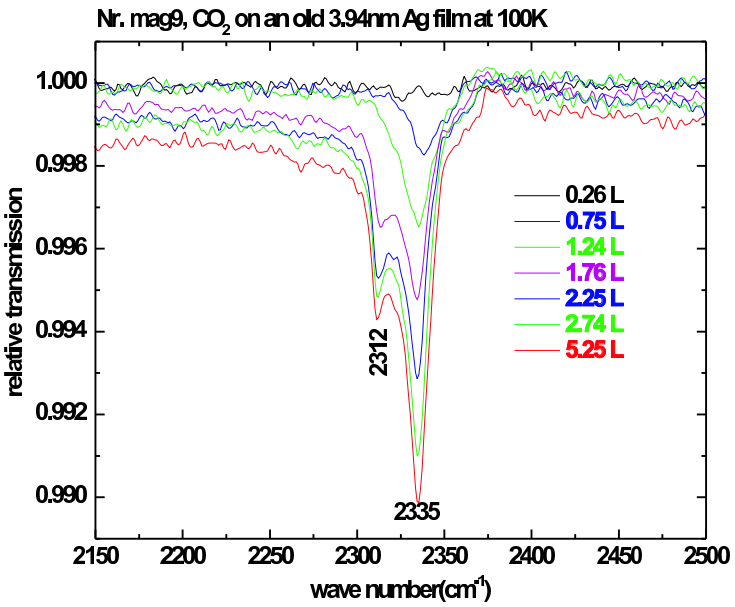

Figure 4.48: SEIRA of CO_2 adsorbed on a 3.4 nm Ag film prepared at room temperature. The details of this Ag film can be found in text. The SEIRA spectra are shown as measured. From up to down the peak intensity increases following the increasing coverage of CO_2 gas on Ag film. The dose of gas for every spectrum is indicated in the same sequence.

the smooth sinuous structures, which will be explained later in § 4.5.4.2. During the long time exposure of N_2 no CO_2 peak on the spectra was found.

Measurements in Reflection Geometry As we discussed above, because of the dipole selection rule on a metal surface, IR reflection spectroscopy in oblique incidence can detect the adsorbed species oriented perpendicularly to a smooth metal surface. In Fig. 4.49 (A) we show the reflection spectra measured at an incident angle of 80° during CO exposure to a 6.6 nm Film (No.mag6). The AFM image of the film is shown in (B). Based on a flat surface there are some small surface structures which give an enhancement to the CO absorption. That is why we only see the three sharp peaks due to physisorbed CO on ordered facets.

We measured the spectra of CO adsorbed on film No.mag8 alternately in both transmission and reflection geometry. The thickness of film No.mag8 is close to the percolation threshold. The reflection spectra of the film are shown in Fig. 4.50 (A) and the transmission spectra in Fig. 4.50 (B). All the relative transmission spectra of CO were calculated with a pre-measured transmission spectrum of the Ag film. Reflection spectra mainly show the absorption of molecules adsorbed on the surface, while transmission spectra show that of molecules adsorbed on side walls. Because of the special surface structure we get strong signals by measuring in both geometries. Certainly, there are some difference on the intensity and frequency between the two kinds of

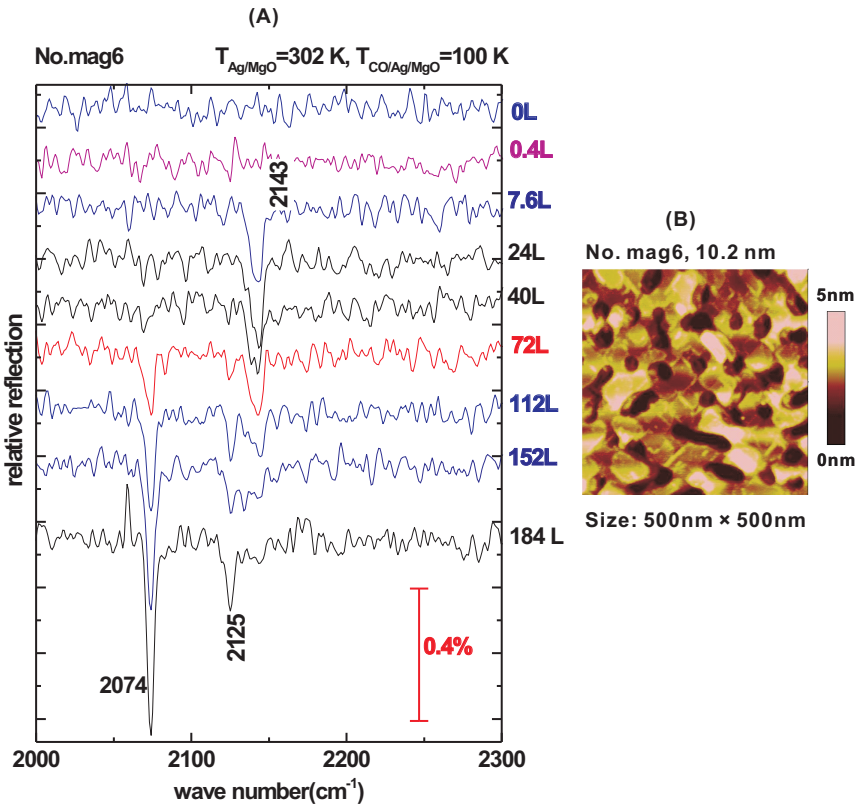

Figure 4.49: (A) Selection of relative IR reflection spectra measured in situ during CO exposure to a relatively smooth film (No.mag6) at 100 K. Only the three peaks due to physisorbed species appeared. (B) The AFM image of this film. It shows a flat surface with some shallow holes and small structures on it.

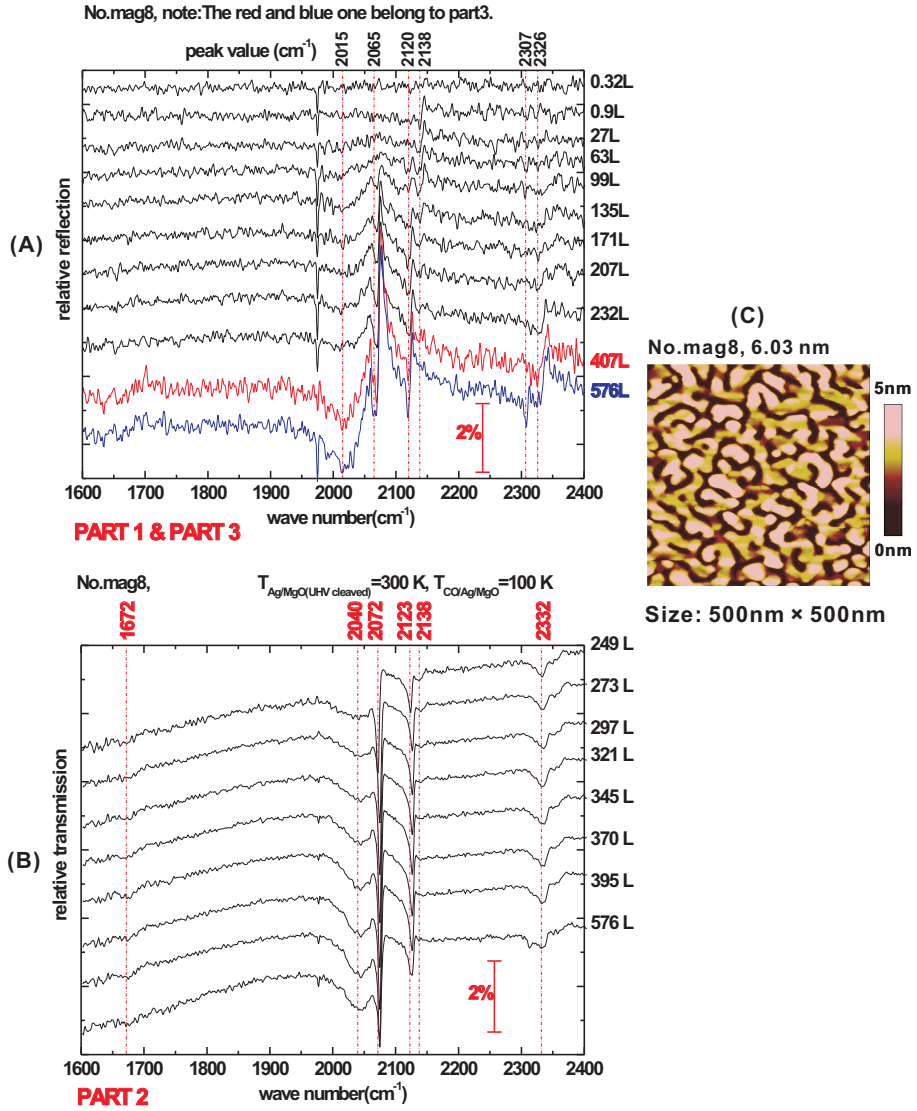

Figure 4.50: (A) and (B) Selection of relative IR spectra measured in situ in both geometries during CO exposure to a 6.03 nm Ag film (No.mag8) at 100 K. In (A) the reflection spectra and in (B) the transmission spectra are shown. We measure the reflection spectra in the beginning. After some time, we turn the sample to the position for transmission geometry and measure the spectra of the total sample against vacuum. Using a pre-measured reference the relative transmission spectra of CO were calculated. The base line shift could not be true. Again after some time we turn the sample back to the position for reflection measurement. With the same method we calculate to get the relative reflection spectra of CO (which are shown as the last two spectra in (A)). At the end, after the exposure was stopped the spectrum does not change if the sample temperature was kept. So we have the possibility to measure the spectrum at the final dose in transmission geometry again.
(B) AFM image of this film.

spectra. For example on the reflection spectra we did not see the peak at 1672 cm^{-1}.

4.5.4.2 SEIRA of CO Adsorbed on Ag Films Grown at High Temperatures

As shown in Fig. 4.29 (B), the 32 nm film grown at 400 K shows a structure corresponding to the percolation threshold; in Fig. 4.30 (C) and (D), the two films grown at 500 K show big islands with smooth surfaces. When we expose CO gas to these films at about 100 K we get strong SEIRA of CO by measuring in transmission geometry. In Fig. 4.51 (A), Fig. 4.52 (a) and Fig. 4.53, the SEIRA spectra of CO adsorbed on such films are shown in a sequence of the substrate temperature at which the films were deposited. Except for the film No.mag24 shown in Fig. 4.53 (B) (which was deposited under a high base pressure), we find the spectra of CO adsorbed on all the other films show multi-peaks as we found on the room-temperature prepared films in the percolation area. The appearance of those multi-peaks is owing to the same reason as we have explained there. Because we measure in normal transmission geometry and the bonds of CO molecules absorbed on a smooth surface are usually oriented to the surface normal direction, all the signals we measured come from the molecules adsorbed on the side walls of islands. The intensity of the two sharp peaks, which are around 2071 cm^{-1} and 2123 cm^{-1} corresponding to physisorbed CO molecules on ordered facets, can be affected by some factors, for example the surface area of side walls, the quality of the crystalline, the width of the voids between islands etc. Thus we cannot ascribe the different intensities found under the same amount of dosed CO on different films to any dependence like the substrate temperature and the film thickness etc. However, there is one thing we can say about the first appeared asymmetric peak around 2145 cm^{-1}. On the film grown at 400 K, which has a surface structure corresponding to the percolation threshold, the asymmetry of this peak is the highest.

On another 500 K prepared film (No.mag24) which was not included in the series above, whose SEIRA of CO are shown in Fig. 4.53 (B), we find only the two peaks at 2072 $cm^{-1}$and 2124 cm^{-1} due to physisorbed CO. Their intensity keeps increasing with the increased amount of dosed CO without getting saturated. During the film growth, the substrate temperature is kept at 500 K by heating with filaments and the base pressure is high. Before the exposure starts, the filaments were switched off and the sample is already cold, but the base pressure is still as high as 1.2×10^{-9} mbar. It could be the residual gas at such a high pressure that suppresses the CO adsorption on the other sites on which we have observed the CO signal at a better base pressure. Another possibility is due to the ion-getter pump. Although it offers a quite low pressure, it might crack some molecules and produce some ions, which could affect the adsorbed CO and show some confusing IR signals. More experimental studies are necessary to make this clear.

In order to easily see the change of peak intensity versus CO gas dose, we perform some plots as we have done on the SEIRA spectra of CO adsorbed on room-temperature prepared films. In Fig. 4.51 (B) the relative intensity of every peak shown in Fig. 4.51 (A) is plotted as a function of elapsed time. At $t = 0$, the gas exposure starts. When

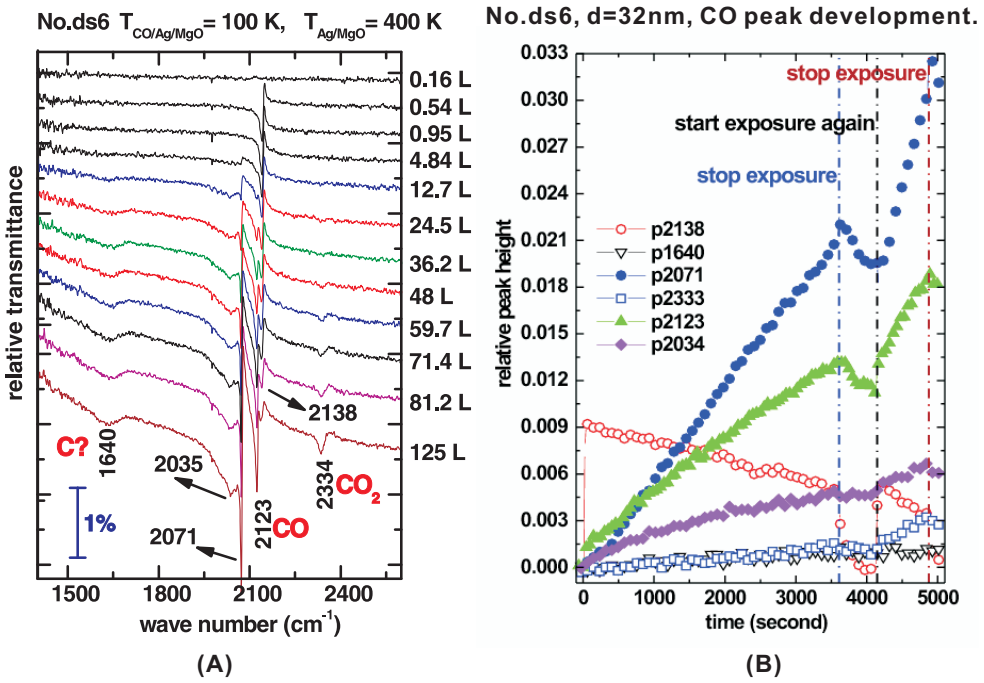

Figure 4.51: (A) Selection of the relative transmission spectra of CO adsorbed on a Ag film at 100 K. The Ag film was prepared at 400 K on a UHV cleaved MgO(001) surface. The labels with unit "L" show the dose of CO gas (1L=1×10^{-6} mbar). The labels without unit are the stretching frequencies of adsorbed CO and CO_2. (B) Intensity development of every peak found in (A) versus elapsed time after the CO gas exposure was started. There are three dashed erect lines which indicate the beginnings of three different processes as shown by the words. "stop exposure" means from then the gas dose valve was closed and pressure decreased fast. "start exposure again" means after that time the gas dose valve was open again and the CO pressure goes to the same level as in the former exposure. The third line means from then the exposure was stopped again. At every time that the exposure was stopped, the intensity jump of the peak at 2071 cm^{-1} was observed.

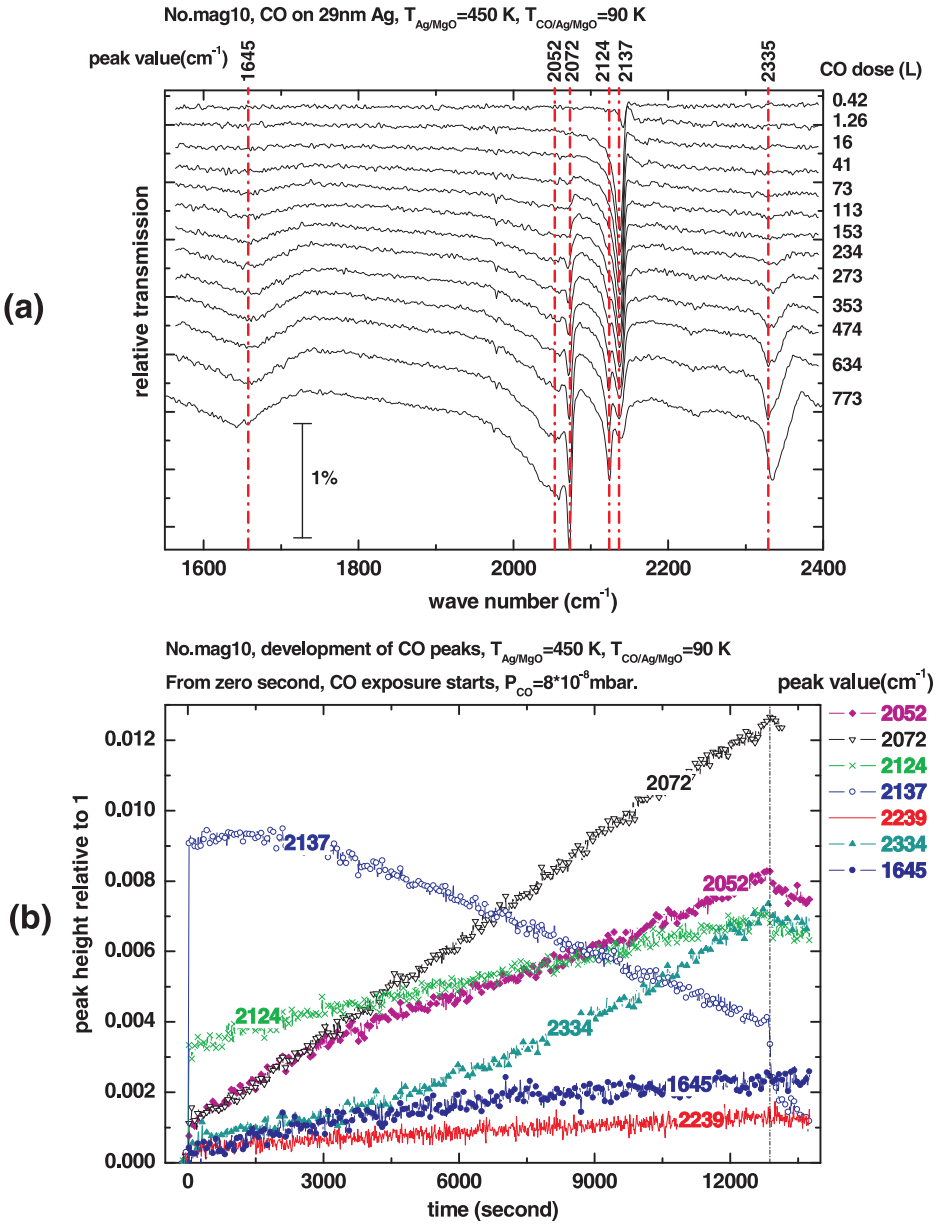

Figure 4.52: (a) SEIRA of CO absorbed on a 450 K prepared Ag film at 90 K. (b)Development of every peak found in (a) since CO was exposed. At $t = 0$ second, CO exposure starts. The erect dashed line indicates the moment when CO exposure was stopped.

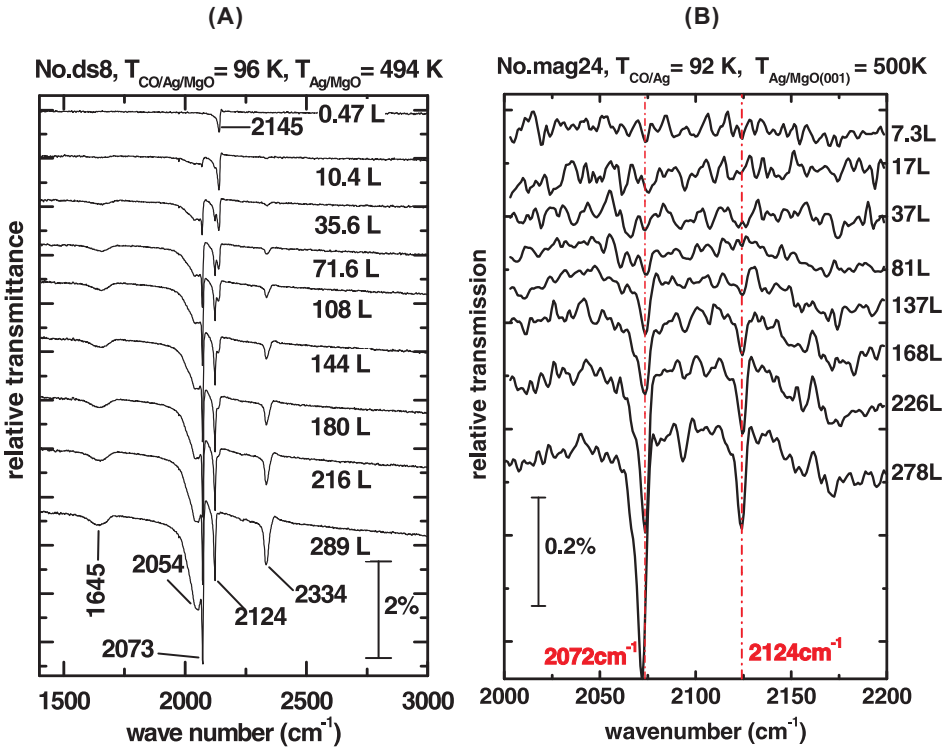

Figure 4.53: (A) SEIRA of CO adsorbed on a 500 K prepared film at about 90 K. The UHV was kept by an ion getter pump together with a TSP.
(B) SEIRA of CO adsorbed on a 500 K prepared film at 92 K. The UHV was kept only by a Turbo molecular pump. The base pressure just before exposure starts is around 1.2×10^{-9} mbar. The Ag film was deposited under a base pressure higher than 5×10^{-9} mbar.

the valve of gas dose was closed, the intensity of peaks at 2071 cm^{-1} and 2123 cm^{-1} decreases. That is a typical property of physisorbed species. The phenomenon that the intensity of the peak at 2071 cm^{-1} jumps to higher values then starts to decrease at the moment when CO exposure was stopped was observed again. The reason for this phenomenon is unclear yet.

In Fig. 4.52 (b) we make the same kind of plot for every peak we observed in Fig. 4.52 (a). However, at the moment that exposure was stopped, we did not observe the intensity jump on the peak at 2072 cm^{-1}. The intensity of most peaks decreases when the CO dose valve was closed.

4.5.5 Discussion on SEIRA of CO Adsorbed on Ag Films

In this chapter we presented the IR spectra of various Ag films and SEIRA spectra of CO adsorbed on them. We can sort the films by the CO signal found on them:

1. On cold-deposited Ag films and room-temperature prepared ultra-thin films consisting of tiny islands, we find CO vibrations as reported in the literature.
2. On smooth Ag films we observed only the weakly physisorbed CO species.
3. On room-temperature prepared films with their thicknesses close to the percolation threshold, at 100 K, we find not only strongly enhanced multi-vibrations of CO but also a CO_2 peak which appeared after hundreds of L of CO was exposed.
4. For all the films prepared above 400 K, we never arrived at the percolation threshold. On such kind of films, strongly enhanced multi-vibrations of CO and a CO_2 peak were found as on the films in (3).

The strong enhanced CO signal found on the Ag films in 3 and 4 are surprising: 1. The sticking of CO and CO_2 at 100 K is unusual since we believe that our silver films are not contaminated and since we do not believe in the existence of catalytically active atomic Ag on the MgO surface for films prepared at elevated temperatures. We explain the unusual sticking by different equilibrium conditions in small pores. 2. If the CO_2 peak was considered to be the product of a Boudouard reaction at only 100 K, the temperature for such kind of reaction is quite low [85] and the understanding of it needs more experimental and theoretical work. 3. The strong enhancement of CO vibrations found on high-temperature prepared films is surprising. It could not be induced by the atomic-scale roughness since it doe not exist on high-temperature prepared films any more.

Recently some reports indicate that the strong enhancement is attributed to the excitation of transverse collective electron resonances by incident radiation polarized parallel to the array of islands [13, 14]. A broad absorption band given by the Ag islands deposited on dielectric substrates due to these resonances is well known in the visible range.These resonances can generate an enhanced electromagnetic field near the metal surface, thereby contributing to the enhancement of visible absorption by the adsorbed

surface molecules. It is also recognized that the broad absorption band in the visible range shifts to longer wavelength and becomes broader with increased dipole-dipole interactions of the islands. There is also evidence that the enhancement is restricted within narrow regions (ca. 5 nm) in contact with the metal islands. Moreover, only those vibrations that accompany a change in dipole moment perpendicular to the microscopic surfaces are enhanced. We emphasize the significance of the close packing of elongated islands with definite channels around them to obtain a large absorption enhancement. The small channels between islands are crucial for the enhancement [13].

5 Experimental Results and Analysis II: Cu Films Grown on MgO(001)

For the Cu/MgO(001) system, there exist a lot of studies. Compared with the system Ag/MgO(001), there is a bigger lattice mismatch (≈15%) between the lattice constants of MgO(001) (4.2 Å) [86] and Cu (3.6 Å). Studies also indicate that Ag bonds more weakly to MgO(001) than Cu does in both 2D and 3D islands [87]. As we mentioned in § 2.6, the adsorption energy for Ag on MgO(001) (0.18 eV) is much lower than that for Cu on MgO(001) (0.99 eV), as well as the diffusion barrier of Ag and Cu adatoms on the substrate. Now we refer to Eq. 2.47 again. With a bigger adsorption energy and a higher diffusion barrier, and with the same amount of metal coverage, we will get a higher density of islands for Cu on MgO(001) than for Ag on MgO(001). Such a result is illustrated by the AFM images of a 0.5 nm Cu film and a 0.5 nm Ag film shown in Fig. 5.1. The number of islands per unit area on the Cu film is about 6 times that on the Ag film.

Also at higher thicknesses, Cu films show different morphologies compared to Ag films. As we have shown for Ag films grown on MgO(001), the film growth can be affected by a lot of factors, like the substrate temperature, the base pressure and the presence of a surfactant etc. Here we present our studies with IR spectroscopy and AFM on Cu-film growth on MgO(001). All the Cu films were prepared at room temperature.

In table 5.1 a list of experiments of which the results are presented in this chapter is shown.

5.1 Measured IR Transmission Spectra of Cu Films Grown on MgO(001) at Room Temperature

For a Cu film grown on MgO(001) at room temperature, we vary a lot of factors to see their effect on the film growth. For example, in Fig. 5.2 (A), we show the IR relative transmission spectra of four Cu films grown on UHV-cleaved MgO surfaces under different conditions. UHV-cleaved MgO(001) surfaces are not contaminated so that we can ascribe the difference observed on the IR spectra to the different conditions under which the films were prepared. We have tried to compare the spectra of different films in the way as we did for Ag films. However, no superposition was found on the spectra of each pair of the films. Thus all the factors we varied show effects on the film growth.

Table 5.1: List of experiments about Cu-film growth on MgO(001) performed at room temperature. d denotes the average film thickness; "rate" denotes the evaporation rate; "geometry" denotes the measurement in transmission (T) or in reflection (R) geometry.

	Substrate temperature	pressure during deposition	deposition	final thickness	IR Spectrosopy	CO exposure		
Exp	T (K)	P (mbar)	Rate (nm/min)	d(nm)	geometry	T (K)	P_{CO} (10^{-8}mbar)	geometry
meng6	297	3.1×10^{-10}	0.102	0.5	T	97	2.6	T
meng7	297	8.6×10^{-10}	0.102	0.8	T	99	2.4	T
(till the end)	298	7×10^{-10}	0.109∼0.103	5.9	T	100	2.4	T
meng8	303	2.5×10^{-10}	0.09	0.8	T	98	2.5	T
(till the end)	298	$5\sim1.9\times10^{-9}$	0.103	6	T	104	2.4	T
meng9	297	4×10^{-8} (CO)		0.1	T			
(till the end)	297	1.8×10^{-9}	0.097∼0.092	7	T	111	2.4	T
meng10	300	4×10^{-8} (CO)		0.1	T			
(till the end)	299	1.9×10^{-9}	0.096∼0.092	6.7	T	100	2.4	T
meng11	300	6×10^{-10}	0.095	6.7	T	100	2.6	T
meng12	299	4.6×10^{-10}	0.1	6.9	T	102	2.4	T
meng14	298	5.9×10^{-10}	0.095	6	T	116	2.4	T
meng15	297	4×10^{-8} (CO)	0.102	5.5	T	102	2.5	T
meng16	296	4×10^{-8} (CO)	0.098	6.1	T	100	2.5	T
mengCu	302	1.3×10^{-9}	0.088	5.9	R	93	5	T

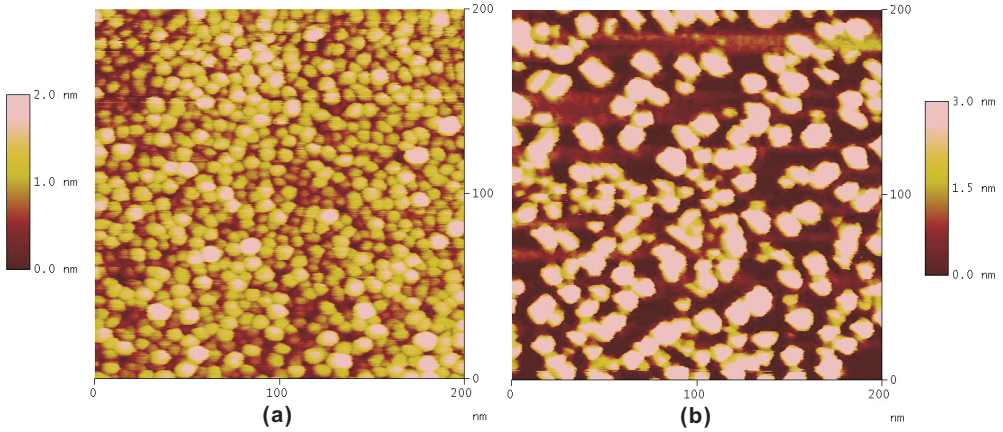

Figure 5.1: (a) AFM image of a 0.5 nm Cu film grown on a UHV-cleaved MgO(001) surface at 300 K; (b) AFM image of a 0.5 nm Ag film grown on a UHV-cleaved MgO(001) surface at 300 K. The scan size for both images is $200 \times 200\,\mathrm{nm}^2$.

For the films shown in picture (b) and (c), we varied the conditions only in the very beginning of the film growth. Thus a change in the nucleation process results the later difference as we saw by IR spectra.

For the film shown in (c), only the initial 0.1 nm thick Cu film was grown with CO exposure. However, the whole film shown in (d) was grown with CO exposure. As we said, the spectra of the two films are not superposable with each other, neither with that of the film shown in (a). Thus CO exposure affects not only the nucleation process but also the later growth process.

For the film grown with 0.8 nm Cu predeposition as shown in picture (b), we see its percolation threshold appears at a lower thickness (3.25 nm) and at a higher transmittance than that of the other three films. The percolation threshold of the film grown with CO exposure shown in (d) appears at a second lower thicknes (3.64 nm) compared with the others. For the left two films, the percolation thresholds are at around 4.25 nm and their transmittance at the percolation threshold do not show obvious discrepancies. The AFM images in a small scan size of the films shown in (a) and (d) are presented in Fig. 5.2 (B). The film grown with CO exposure consists of smaller islands, which results in the shift of the percolation threshold to a lower thickness. The AFM images of this two films will be shown in Fig. 5.9 in a bigger scan size and compared to the images of the other two films.

In Fig. 5.3, we show the series of IR spectra of Cu films grown on air-cleaved MgO(001) surfaces in the same sequence as in Fig. 5.2 (A). Like we have found for the Cu films grown on UHV-cleaved MgO(001), the IR spectra of these four films are not superposable with each other either. Different from that we saw in Fig. 5.3, the film grown with CO exposure at 4×10^{-8} mbar shown in (d) shows a percolation threshold at a lower thickness ($<$3.5 nm) and at a higher transmittance than that of the other three films. Its spectrum at the final thickness looks more Drude like. For the other three films, the

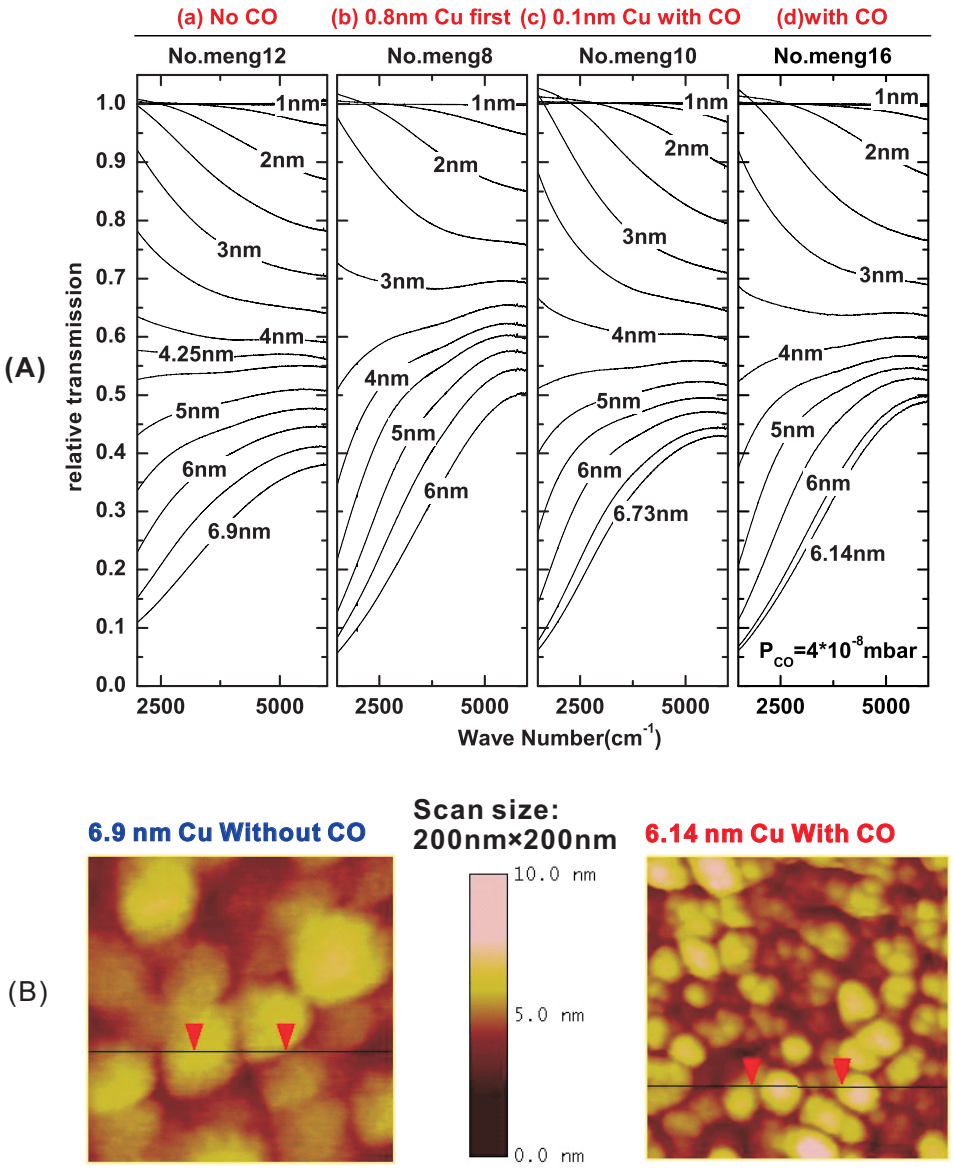

Figure 5.2: (A) Selected IR relative transmission spectra of Cu films grown on UHV-cleaved MgO(001) surfaces. (a) the film is grown under normal conditions; (b) 0.8 nm Cu was grown first, then it was cooled down to about 100 K and exposed to CO, after that it was heated back to room temperature to continue the growth until the end; (c) Only the initial 0.1 nm Cu film was grown with CO exposure at 4×10^{-8} mbar; (d) the total film was grown with CO exposure at 4×10^{-8} mbar. (B) AFM images of the two films shown in (a) and (d).

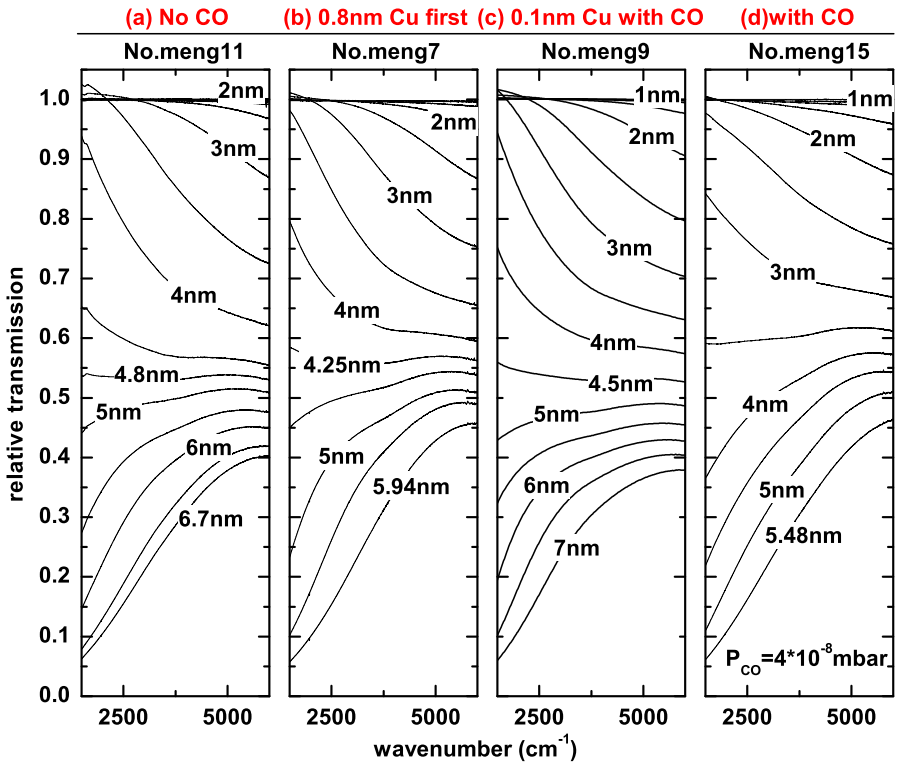

Figure 5.3: Selected IR relative transmission spectra of Cu films grown on air-cleaved MgO. (a) the film is grown under normal conditions; (b) 0.8 nm Cu was grown first, then it was cooled down to about 100 K and exposed to CO, after that it was heated back to room temperature to continue the growth until the end; (c) Only the initial 0.1 nm Cu film was grown with CO exposure at 4×10^{-8} mbar; (D) the total film was grown with CO exposure at 4×10^{-8} mbar.

thickness at the percolation threshold of each film is in the range of 4.3 nm to 4.8 nm. The reason for this difference is that the defects on every MgO(001) surface are not equivalent, and they account partially for the difference we saw in the IR spectra.

A comparison for Cu films grown on different-way prepared MgO(001) surfaces is made on the two films grown with CO exposure. As shown in Fig. 5.6, the Cu film grown on air-cleaved MgO(001) behaves more like bulk Cu.

5.2 Fit of the Transmission Spectra with the Drude Type Model

Fits of the spectra in different spectral ranges

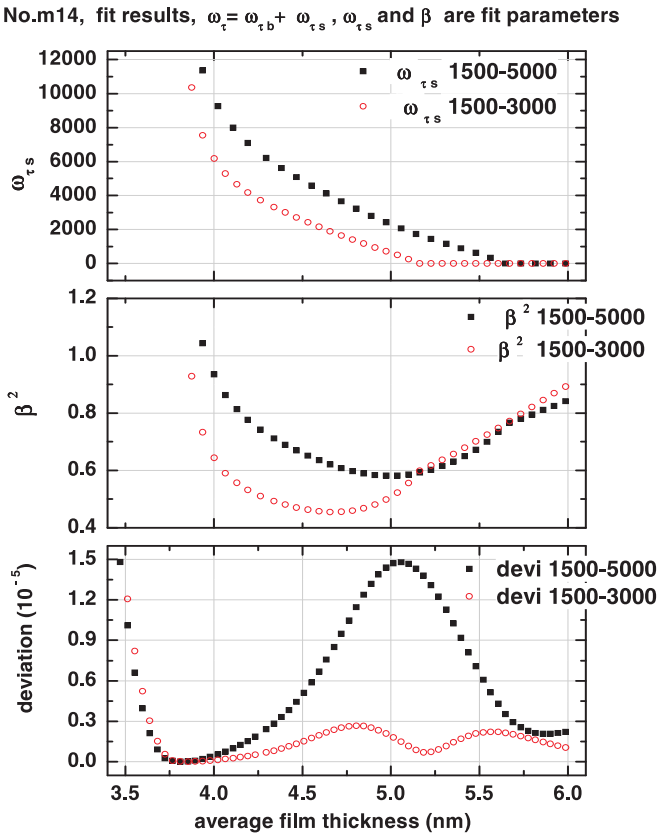

Figure 5.4: The *deviation* and the best-fit parameters $\omega_{\tau s}$ and β^2 versus the film thickness of two fits to the spectra of film No. meng14 in different spectral ranges.

With the same Drude type model, the relative transmission spectra of percolated Cu films are calculated. The frequency dependence of the two Drude parameters $\omega_{\tau b}$ and ω_{pb} of Bulk Cu shown by Eq. 2.50 is very important for the calculation. As we did for the spectral calculation for Ag films, the two frequency independent parameters $\omega_{\tau s}$ and β are used as fit parameters. Fits in two different spectral ranges are performed to the spectra of the film No. meng14, which is grown on an air-cleaved MgO(001) surface at about 300 K under normal conditions. The fitted parameters are shown in Fig. 5.4 and the best fitted spectra are shown in Fig. 5.5. We met the same problem as when we fit the spectra of room-temperature prepared Ag films. When the spectral range for the fit concentrates at the low-frequency side, the fit quality is better and more spectra can be fitted. The abnormal behavior of spectra at the high-frequency side is induced by the strong dipole-dipole interaction between Cu islands.

Fit Results to the Spectra of Two Different Films

In Fig. 5.6, fitted results to the spectra of two films and the best-fit spectra are shown in (a) and (b) respectively. Both films were grown with CO exposure but one

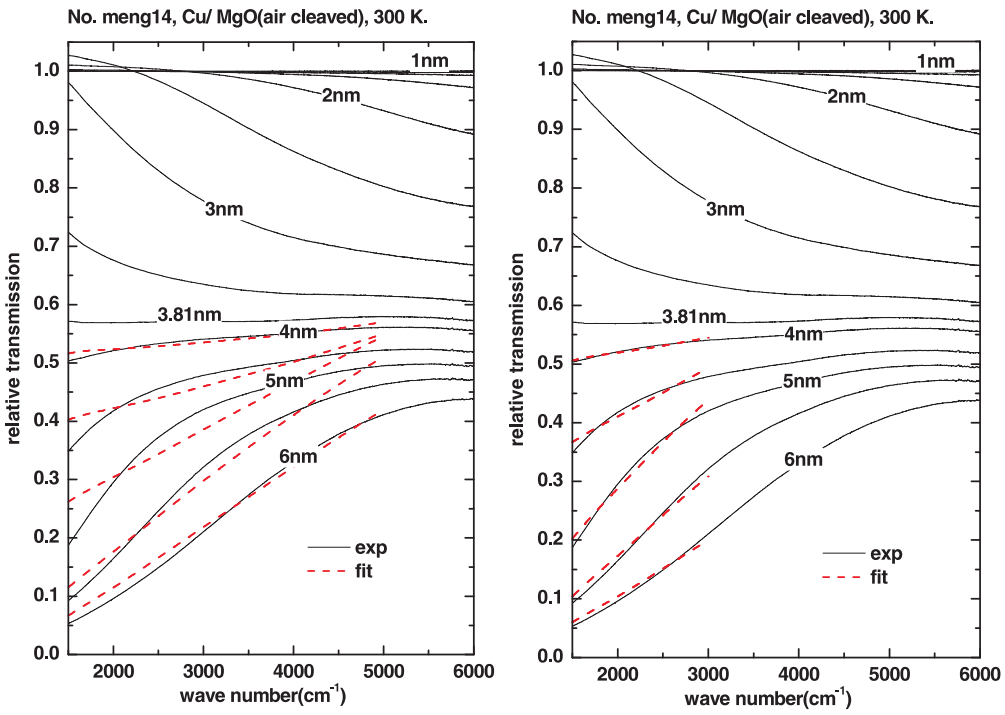

Figure 5.5: Comparison of the measured spectra (solid lines) of film No.meng14 and the best fitted ones (dashed lines) in different spectral ranges: (a) 1500-3000 cm^{-1}; (b) 1500-5000 cm^{-1}.

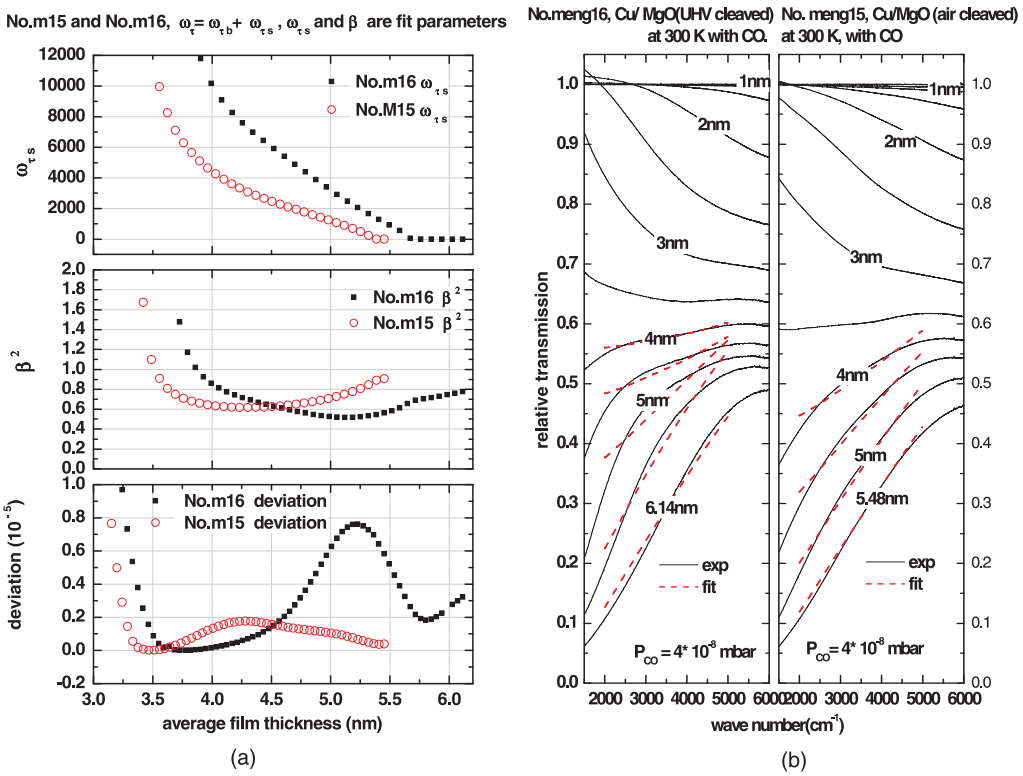

Figure 5.6: (a) The *deviation* and the best-fit parameters $\omega_{\tau S}$ and β^2 versus the film thickness of the fits to the spectra of film No.meng16 and film No.meng15. (b) Best fitted spectra of the two films.

on air-cleaved MgO(001) and another on UHV-cleaved MgO(001). Comparing the fitted parameters of the two films at the same thicknesses in (a), a smaller surface relaxation rate $\omega_{\tau S}$ and a smaller *deviation* were observed for the film grown on air cleaved-MgO with CO exposure. Also a near unity β^2 value is shown at a smaller thickness on the same film. All these smaller parameters indicate a film starts to display bulk Cu properties at a smaller thickness. Accordingly, in graph (b) we see better fitted spectra for the film grown on air-cleaved MgO(001).

5.3 Reflection Spectra of Cu Films Grown on MgO(001) at Room Temperaure

In Fig. 5.7 the reflection spectra of a Cu film grown on an air-cleaved MgO surface at 300 K are shown. Similar to the Ag/MgO(001) system, a reflectance minimum at 5.6 nm is observed. The thickness of the reflection minimum is above the percolation threshold shown in Fig. 5.3.

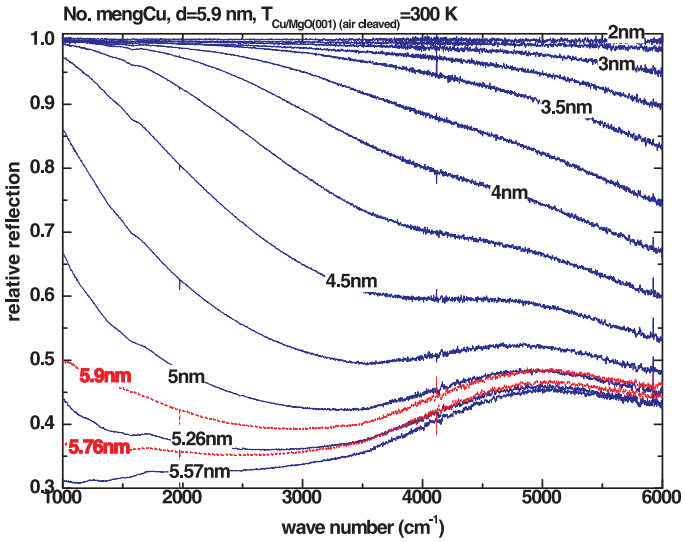

Figure 5.7: Selected IR relative reflection spectra of a Cu film grown at 300 K on an air-cleaved MgO(001) surface.

5.4 AFM Images of Cu Grown on MgO(001)

The AFM images of Cu films show quite different morphologies from that of the Ag films. In a thickness range of 5.5 nm to 7.0 nm, the Cu films are all island like. This is due to the bigger diffusion barrier and adsorption energy of Cu on Cu and Cu on MgO than that of the Ag/MgO system.

The AFM images of the Cu films grown on air-cleaved MgO(001) are shown in Fig. 5.8 and that of the films grown on UHV-cleaved MgO(001) are shown in Fig. 5.9. The thicknesses of the films distribute in a range of 5.5 nm to 7.0 nm. In both figures, we see smallest islands on the two films grown with CO exposure (see Fig. 5.8 (c) and Fig. 5.9 (d)). Also the size and shape distribution of the islands on both films is more homogenous than that on the other films. The films grown under normal conditions (see Fig. 5.8 (a) and Fig. 5.9 (a)) show bigger islands than on the other films. The biggest islands belong to the film shown in Fig. 5.9 (a). A further comparison is difficult because the films have different thicknesses.

In conclusion, predeposition of 0.8 nm Cu and CO exposure at different growth stages can help to get small islands. Exposure of CO during the total film growth works efficiently.

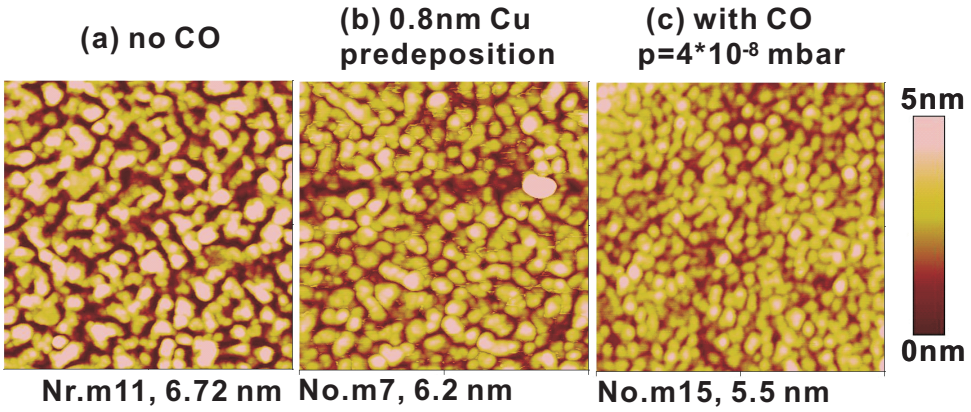

Figure 5.8: AFM images of Cu films grown on UHV-cleaved MgO(001) surfaces at room temperature under different conditions. The scan size is the same for every image: $500\times500\,\mathrm{nm}^2$. (a) normal growth, pressure $< 1\times10^{-10}$ mbar; (b) after 0.8 nm Cu film was prepared, it was cooled down to about 100 K and exposed to CO, then it was heated back to room temperature to continue the growth until the end; (c) the total film was grown with CO exposure at 4×10^{-8} mbar.

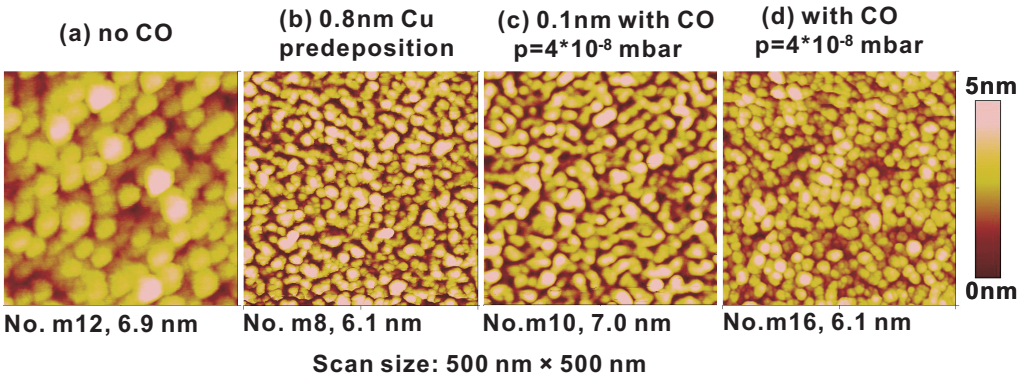

Figure 5.9: AFM images of Cu films grown on UHV-cleaved MgO(001) surfaces at room temperature under different conditions. The scan size is the same for every image: $500\times500\,\mathrm{nm}^2$. (a) normal growth, pressure $<1\times10^{-10}$ mbar; (b) after 0.8 nm Cu film was prepared, it was cooled down to about 100 K and exposed to CO, then it was heated back to room temperature to continue the growth until the end; (c) only the initial 0.1 nm Cu film was grown with CO exposure at 4×10^{-8} mbar; (d) the total film was grown with CO exposure at 4×10^{-8} mbar.

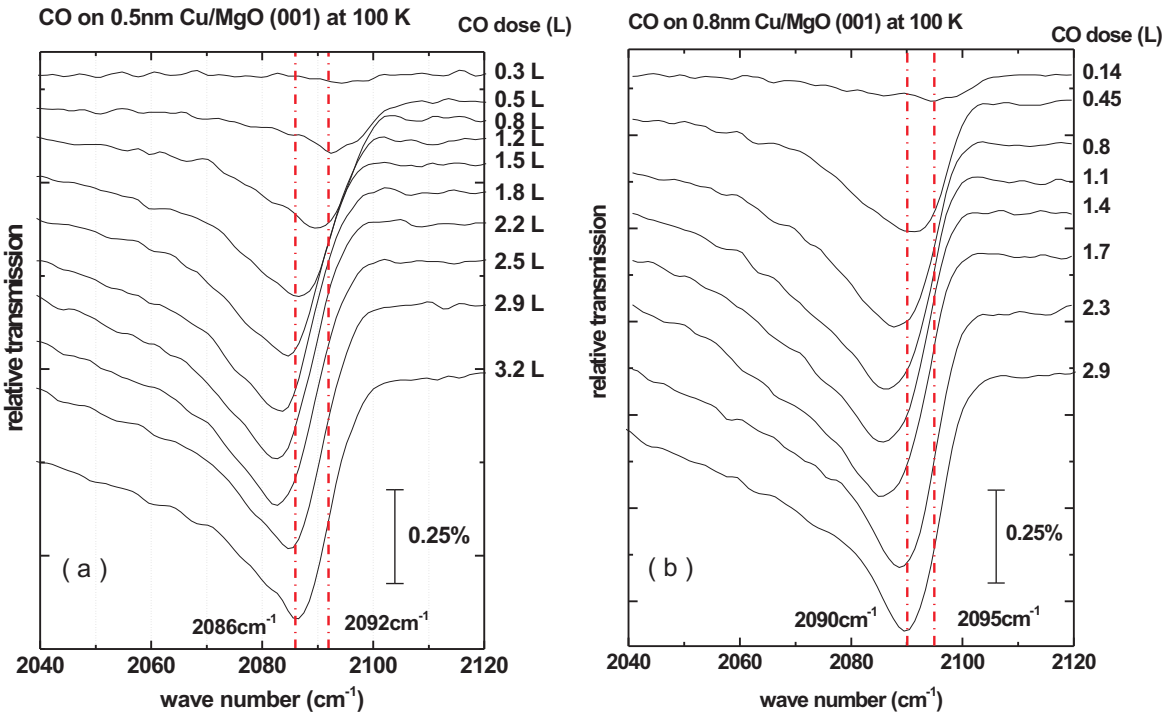

Figure 5.10: SEIRA of CO adsorbed on a 0.5 nm Cu film (a) and on a 0.8 nm Cu film (b) at about 100 K. The spectra were shown from the beginning of exposure until the saturation, and the dosage of CO was counted in L (Langmuir, 1L=1×10^{-6} Torr·s). The MgO(001) substrate was cleaved in the UHV chamber.

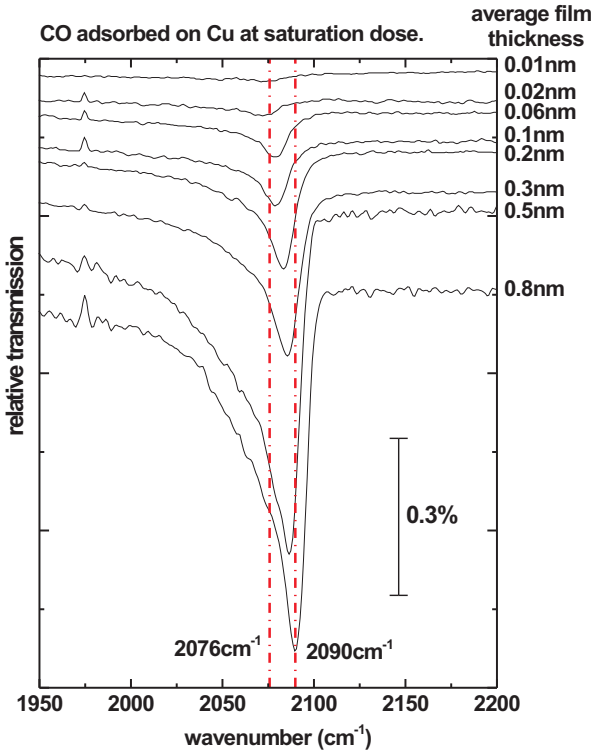

Figure 5.11: Comparison of SEIRA of CO adsorbed on ultrathin Cu films consisting of small Cu islands at saturation exposure.

5.4.1 SEIRA of CO Adsorbed on Ultrathin Cu Films Consisting of Small Islands

In Fig. 5.10 the SEIRA spectra of CO adsorbed on a 0.5 nm and a 0.8 nm film were shown until saturation. In the beginning, the vibrational frequency of CO on both films decreases with the increase of CO coverage. Later on , the frequency increases back and stops at 2086 cm^{-1} and 2090 cm^{-1} respectively. The peak appeared on both films is for CO adsorbed on Cu(001) facets [16, 15]. The shift to lower frequencies could be due to chemical effects (back donation). However the later shift to higher frequencies could be attributed to [16, 15]: (1) a weak dipole-dipole coupling of the adsorbed molecules, (2) the island like mechanism of the adsorbed film growth, (3) mutual compensation of a blue shift from mode coupling and a red shift due to chemical effects (back donation).

In Fig. 5.11 we show the CO peaks at saturation exposure on various thick Cu films. The spectra of CO adsorbed on Cu films with a thickness at and below 0.3 nm are from Ref. [16]. Following the increase of Cu coverage, the peak area increases and the frequency of the peak shows a blue shift. In Fig. 5.12 we plot the frequency of the CO peak on each film versus the average film thickness of Cu. The vibrational frequency of CO adsorbed on Cu films below 0.3 nm indicates CO adsorbed on Cu(111)

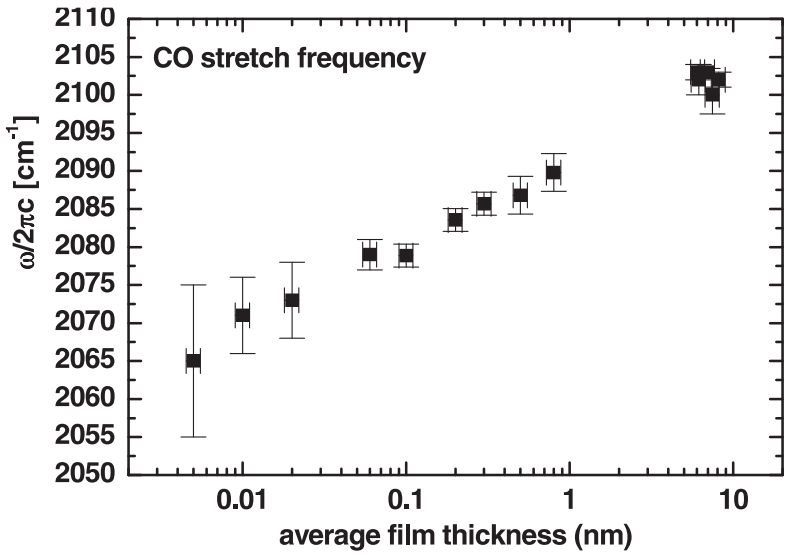

Figure 5.12: CO vibrational frequency at saturation exposure versus the average thickness of ultrathin Cu film.

facets, whereas the frequency of CO adsorbed on Cu films from 0.3 nm to 0.8 nm thick indicates CO adsorbed on Cu(001) facets. The increase of peak area is due to the increase of Cu coverage, so as to the adsorbate sites for CO.

5.4.2 SEIRA of CO Adsorbed on Thick Cu Films

In Fig. 5.13 we show SEIRA of CO adsorbed on two thick Cu films. In (a) the spectra are for CO adsorbed on the Cu film (No.meng12) on which we see the biggest islands by AFM image shown in Fig. 5.2 (a). The spectra show two CO peaks. In the beginning of CO exposure, an asymmetric peak appears at 2098 cm^{-1} owing to CO adsorbed on Cu(110) facets or polycrystalline Cu. This peak doesn't shift following the increase of CO coverage. Its large asymmetry and big intensity indicate a very rough Cu surface [88]. Later on, another broad peak appears at about 2077 cm^{-1}. This second peak is for CO adsorbed on Cu(111) facets and also does not shift with the increase of CO coverage. The intensity of both peaks has a similar size.

In (b) the spectra for CO adsorbed on the Cu film (No.meng11) grown on air-cleaved MgO(001) under normal conditions are shown. The AFM image of this film is shown in Fig. 5.8 (a). The size of the islands on this film is smaller than that on film No.meng12 (Fig. 5.2 (a)). Different from that we see in this figure (a), the spectra show two peaks having a big discrepancy in intensity. The strong peak appears at 2100 cm^{-1} and the very weak shoulder appears at 2083 cm^{-1}. Neither peaks shift with the increase of CO coverage. The strong peak is for CO adsorbed on Cu(110) facets or polycrystalline Cu. The very weak shoulder is for CO adsorbed on Cu(001) facets. The SEIRA features of CO adsorbed on film No.meng11 indicate a higher degree of disorder of the film

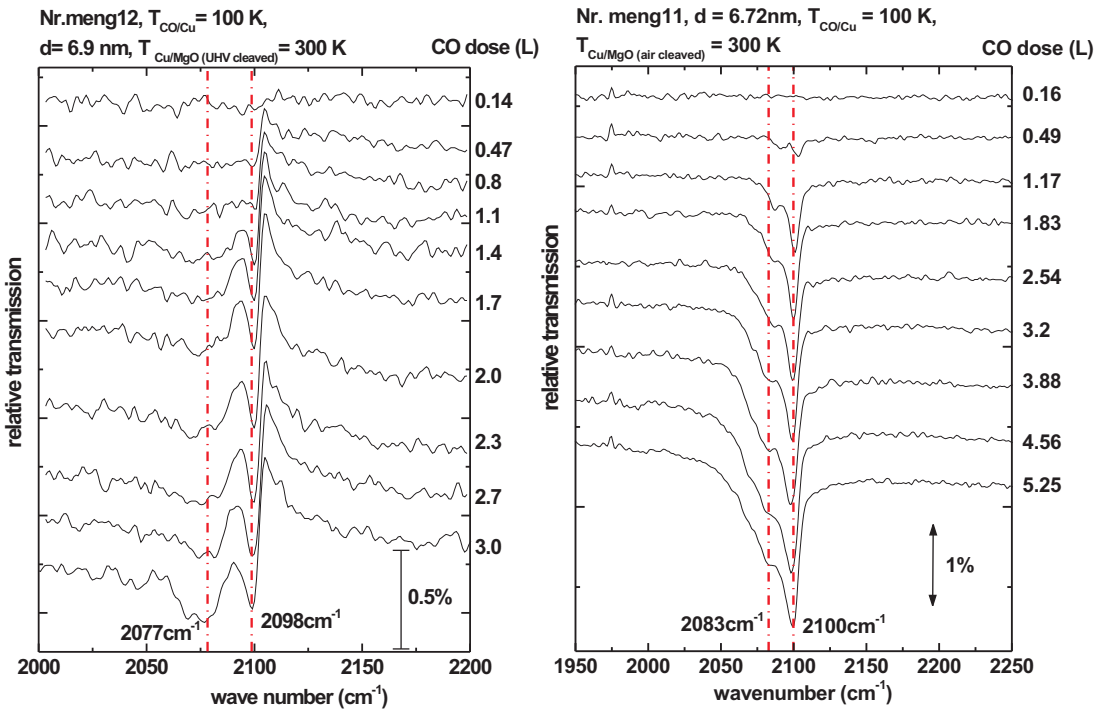

Figure 5.13: (a) SEIRA spectra of CO adsorbed on a 6.9 nm Cu film (a) and a 6.72 nm Cu Film (b) at about 100 K. The spectra were shown from the beginning of exposure until saturation, and the dosage of CO gas was counted in L (Langmuir, 1L=1×10^{-6} Torr·second). The peak position of CO stretching was also indicated. The AFM image of the Cu film in (a) is shown in Fig. 5.9(a) and that of the Cu film in (b) is shown inFig. 5.8 (a).

surface than that of film No.meng12.

The SEIRA of CO on the other films with smaller islands is very similar to that shown in (b).

6 Conclusion and Discussion

In this thesis, the ability of FTIR for investigating the properties of nanofilms and SEIRA effect are brought into full play. With it we studied the IR properties of ultrathin Ag and Cu films grown on MgO(001) substrates under various conditions, and SEIRA of CO adsorbed on Ag and Cu films with different morphologies. The surface morphology is measured by Scanning probe microscopy (SPM), which is a very useful tool for analyzing the surface morphology of films on insulate substrates.

Ag Films Grown at Various Temperatures

In most cases, during a film growth we measured IR relative transmission spectra due to its convenience and high signal to noise ratio. The Ag films grown at elevated temperatures show increased percolation threshold, that can be easily seen by the plot in Fig. 6.1. There in each picture we show the development of transmittance of a Ag film versus the average film thickness at two wave numbers. The five films shown are grown in elevated temperatures. In picture (a), (b) and (c), the crossover of the two curves indicates the percolation threshold. The film thickness and relative transmittance at the percolation threshold are increasing with the preparation temperature. In (d) and (e) the film thickness is still below the percolation threshold.

AFM images of films prepared at different temperatures show quite different morphologies. The film grown at 100 K shows a smooth surface, whereas the 42 nm thick film grown at 500 K shows very big islands in epitaxial distribution. The 300 K-prepared Ag films show various morphologies when the film thickness is different. For example, below 1 nm, the film consists of small separated islands; near the percolation threshold, some big and separated sinuous structures are observed; far above the percolation threshold, the film shows a smooth surface with some shallow holes on it. The 400 K-prepared film is near to the percolation threshold and it shows also sinuous structures similar to that on the 300 K-prepared films but 7 times larger.

Ag and Cu Films Grown with gas Exposure at Room Temperature

The effect of the presence of CO or N_2 at a pressure of 4×10^{-8} mbar on the film growth of Ag and Cu were studied. The presence of CO (in the initial growth stage or in the whole growth process) helps to get smaller Cu islands with homogenous size. However, the presence of CO and N_2 during Ag film growth did not make obvious change seeing from both the IR transmission spectra and the AFM images.

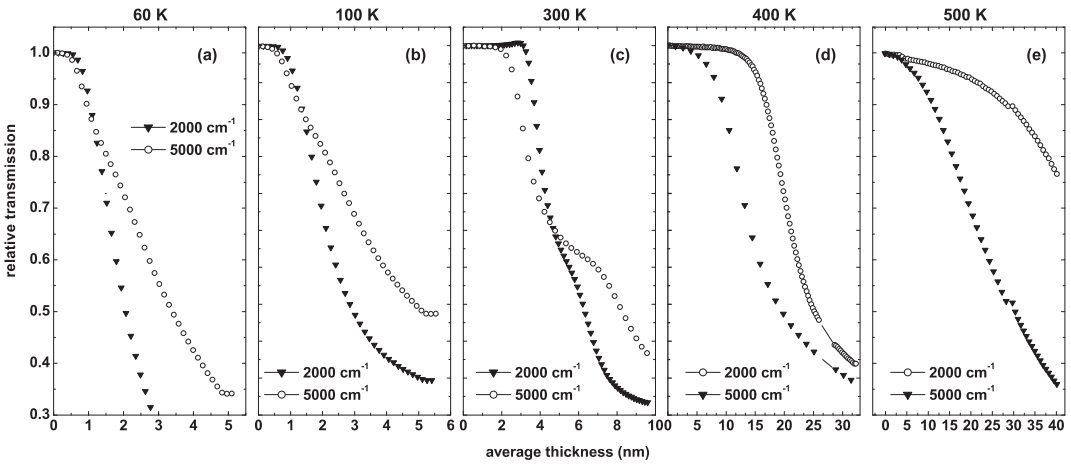

Figure 6.1: Development of transmittance versus the average film thickness at two wave numbers for five Ag films prepared on UHV cleaved MgO(001) surfaces at different temperatures. In (a), (b) and (c) the crossover indicates the percolation threshold.

Reflection Spectra of Ag and Cu Films

During the film growth of both Ag and Cu on MgO(001), IR relative reflection spectra were measured. For both systems, the reflectance shows a minimum at a certain thickness. This certain thickness is slightly above the percolation threshold. Such a phenomenon is not reported in literature yet. For a room-temperature prepared film, except the vicinity of the percolation threshold, all the reflection spectra show a negative slope. However, for the 50 K prepared film, most spectra show a negative slope except in the very beginning of film growth.

Calculations of the IR Spectra of Ag and Cu

The relative transmission spectra of Ag and Cu filmS above the percolation threshold are calculated with a Drude-type model. The spectra of a cold-deposited Ag film are fitted very well. However, the spectra of 300 K-prepared Ag films can only be fit in a spectral range concentrated at the low-frequency side. The reason is that the strong dipole-dipole interaction between separated sinuous structures affected the IR absorption of the film. The same problem is encountered when we make a fit to the spectra of Cu films grown at 300 K.

Below the percolation threshold, in the range of 2.5 nm to 3.5 nm, both the transmission and reflection spectra of the 300 K-prepared Ag films can be fitted well by a 3D Bruggeman Model. However, in the vicinity of the percolation threshold, neither kind of spectra can be fitted by this Model. At higher thicknesses far above the percolation threshold, the transmission spectra can be fitted well and the fit results are consistent with that of a Drude Model fit, whereas, there is a big deviation between the calculated reflection spectra and the measured ones, which probably indicates the anisotropy of the film conductivity.

SEIRA of CO adsorbed on Various kinds of Ag Films

SEIRA of CO adsorbed on ultrathin Ag films ($\leq$0.5 nm) (they were prepared at room temperature) consisting of very small islands at about 50 K give one band for chemisorbed CO and another one for physisorbed CO. The big intensity of physisorbed CO is mainly due to condensed CO on the MgO(001) substrate. The same band of chemisorbed CO is found on the 60 K-prepared film. These are in accordance with the reports from literature.

SEIRA of CO on 100 K-prepared films only shows one band due to physisorbed CO.

SEIRA of CO on the 1 nm film grown at 300 K starts to show multi-CO-bands at 100 K. That indicates the film shows multi-crystalline properties.

Big separated structures are observed on high-temperature prepared films and on 300 K prepared films near the percolation threshold. CO adsorbed on such kind of films at 100 K show multi-CO-bands. Also two other bands appeared, one at 1642 cm^{-1} (condensed C?) and another one at 2335 cm^{-1}(CO_2 band). A Boudouard reaction $CO + CO \rightarrow CO_2$ is assumed to account for the presence of them. Another possibility is that they come from the contamination in gas source.

A film prepared at 300 K having a thickness far above the percolation threshold shows a flat surface with some shallow holes on it. The bonds of CO adsorbed on such a film at 100 K are orientated perpendicular to the smooth Ag surface. Its signal can be detected by measuring in oblique reflection geometry.

SEIRA of CO adsorbed on Cu Films

The frequency of CO molecules is very sensitive to the sites on which they adsorb on Cu films. For example, on a film below 0.3 nm, CO shows a frequency corresponding to Cu(111) facets; on both a 0.5 nm and a 0.8 nm thick film, the peak indicates CO adsorbed on Cu(100) facets; on thick Cu films, CO shows frequencies corresponding to CO adsorbed on Cu(110) facets or polycrystalline Cu.

Open Problems

In most of the experiments, the UHV (Ultra-High Vacuum) as low as 1×10^{-10} mbar is kept by an ion-getter pump together with a TSP (Titanium Sublimation Pump), and in some experiments, the UHV is kept only by a Turbo molecular pump to 1×10^{-9} mbar. SEIRA of CO adsorbed on similar rough Ag films under these two different vacuum conditions show some difference. The difference could be due to the different base pressure, or ascribed to the ion-getter pump. Ion-getter pump might crack some molecules and produce some ions, which could produce special defects on the metal film. A UHV kept only by a Turbo molecular pump and TSP to the same level as kept by the ion-getter pump will help to make it clear.

Bibliography

[1] Krishna Seshan. *Handbook of thin-film deposition processes and techniques.* Noyes Publications, 2002.

[2] Matthias Wuttig and Xiangdong Liu. *Ultrathin Metal Films.* Springer-Verlag Berlin Heidelberg, 1. edition, 2004.

[3] J. A. Venables, G. D. T. Spiller, and M. Hanbücken. Nucleation and growth of thin films. *Rep. Prog. Phys.*, 47:399–459, 1984.

[4] Harald Brune. Microscopic view of epitaxial metal growth nucleation and aggregation. *Surface Science Reports*, 31:121–229, 1998.

[5] H. Bubert and H. Jenett. *Surface and Thin Film Analysis.* Wiley-VCH Verlag GmbH, 2002.

[6] C.H. Shek, G.M. Lin, J.K.L. Lai, and J.L. Li. Fractal structure and optical properties of semicontinuous silver films. *Thin Solid Films*, 300:1–5, 1997.

[7] Guido Eilers and Kōichi Mukasa. Surface Morphology of Thin Cu films Grown on Magnesium Oxide (100). *Jpn. J. Appl. Phys.*, 39:3780–3783, 2000.

[8] A. Hartstein, J. R. Kirtley, and J. C. Tsang. Enhancement of the infrared absorption from molecular monolayers with thin metal overlayers. *Phys. Rev. Lett.*, 45(3):201–204, Jul 1980.

[9] P. Dumas, R. G. Tobin, and P. L. Richards. Study of adsorption states and interactions of CO on evaporated noble metal surfaces by infrared absorption spectroscopy. *Surface Science*, 171:555–578, 1986.

[10] I. Mrozek, C. Pettenkofer, and A.Otto. Raman spectroscopy of carbon monoxide adsorbed on silver island films. *Surface Science*, 238:192–198, 1990.

[11] C. Pettenkofer, I. Mrozek, T. Bornemann, and A. Otto. On the contribution of classical electromagnetic field enhancement to Raman scattering from adsorbates on coldly deposited silver films. *Surface Science*, 188:519–556, 1987.

[12] D. P. DiLella, A. Gohin, R. H. Lipson, P. McBreen, and M. Moskovits. Enhanced Raman spectroscopy of CO adsorbed on vapor-deposited silver. *J.Chem.Phys.*, 73:4282–4295, 1980.

[13] T. Wadayama, M. Takada, and A. Hatta. IR absorption enhancement for ionized p-nitrobenzoic acid on silver island films epitaxially grown on the 7×7 reconstructed Si(111) surface. *Applied Physics A: Materials Science & Processing*, 80:615–619, 2005.

[14] T. Tanabe, Y. Suzuki, and A. Hatta. Enhancement of Surface Infrared Absorption on Silver Islands: Effect of Lateral Interactions. *Phys. Low-Dim. Struct.*, 10:13–22, 1997.

[15] V. P. TOLSTOY, I. V. CHERNYSHOVA, and V. A. SKRYSIIEVSKY. *Handbook of infrared spectroscopy of ultrathin films.* Springer-Verlag, 1. edition, 2003.

[16] Andreas Priebe. *Oberflächenversärkte Infrarotabsorption von CO auf ultradünnen Metallfilmen.* Dissertation, Universität Heidelberg, 2002.

[17] O. S. Heavens. *Thin Film Physics.* Methuen & Co Ltd, 1973.

[18] Vladimir G. Bordo and Horst-Günter Rubahn. *Optics and Spectroscopy at Surfaces and Interfaces.* WILEY-VCH, 1. edition, 2005.

[19] Scout-software package for optical spectroscopy, including dielectric function database, supplied by M.Theiss Hard- and Software(Aachen,Germany).

[20] W. Suetaka. *Surface Infrared and Raman Spectroscopy - Methods and Applications.* Kluwer Academic Publishers, 1995.

[21] Zhijun Zhang and Toyoko Imae. Study of Surface-Enhanced Infrared Spectroscopy: 1. Dependence of the Enhancement on Thickness of Metal Island Films and Structure of Chemisorbed Molecules. *Journal of Colloid and Interface Science*, 233:99–106, 2001.

[22] Masatoshi Osawa. Dynamic processes in electrochemical reactions studied by surface-enhanced infrared absorption spectroscopy (SEIRAS). *Bull. Chem. Jpn.*, 70:2861–2880, 1997.

[23] Masatoshi Osawa and Ken ichi Ataka. Electromagnetic mechanism of enhanced infrared absorption of molecules adsorbed on metal island films. *Surface Science*, 262:L118–L122, 1992.

[24] A. Priebe, M. Sinther, G. Fahsold, and A. Pucci. *Journal of Chemical Physics*, 119:4887, 2003.

[25] X. Zhang and D. Stroud. *Physical Review B*, 52:2131, 1995.

[26] Andrew Zangwill. *Physics at Surfaces.* Press Syndicate of the University of Cambridge, 1988.

[27] David Fuks, Simon Dorfman, Yuri F. Zhukovskii, Eugene A. Kotomin, and A. Marshall Stoneham. Theory of the growth mode for a thin metallic film on an insulating substrate. *Surface Science*, 499(1):24–40, February 2002.

[28] V. Musolino, A. Selloni, and R. Car. First priciples study of adsorbed cu_n (n=1-4) microcluster on MgO(100): structural and electronic properties. *Jounal of Chemical Physics*, 108:5044–5054, 1998.

[29] V. Musolino, A. Selloni, and R. Car. Atomic and electronic structure of Cu clusters on MgO. *Surface Science*, 402-404:413–417, May 1998.

[30] Yuri F Zhukovskii, Eugene A Kotomin, David Fuks, Simon Dorfman, A Marshall Stoneham, and Gunar Borstel. Adhesion trends and growth mode of ultra-thin copper films on MgO. *J. Phys.:Condens. Matter*, 16:4881–4896, 2004.

[31] Yu.F. ZHUKOVSKII, D. GRYAZNOV, A. FINOGENOV, and Yu.N. SHUNIN. Ab initio simulations of the Cu/MgO(001) interface. *SOLID STATE PHYSICS: Computer Modelling and New Technologies*, 5(1):28–41, 2001.

[32] Yuri F. Zhukovskii, Eugene A. Kotomin, David Fuks, and Simon Dorfman. First principles slab calculations of the regular Cu/MgO(001) interface. *Surface Science*, 566-568:122–129, September 2004. Part 1, Proceedings of the 22nd European Conference on Surface Science.

[33] J. R. Jasperse, A. Kahan, J. N. Plendl, and S. S. Mitra. Temperature Dependence of Infrared Dispersion in Ionic Crystals LiF and MgO. *Phys. Rev.*, 146(2):526–542, Jun 1966.

[34] David M. Roessler and Donald R. Huffman. *Handbook of Optical Constants of Solids II*. Academic Press, 1991.

[35] David R. Smith and F. R. Fickett. Low-Temperature Properties of Silver. *J. Res. Natl. Inst. Stand. Technol.*, 100(2):119–171.

[36] Neil. W. Ashcroft and N. David Mermin. *SOLID STATE PHYSICS*. Saunders College Publishing, international edition, 1975.

[37] www.chemicool.com.

[38] M. A. Ordal, R. J. Bell, R. W. Alexander Jr., L. L. Long, and M. R. Querry. Optical properties of the metals Al, Co, Cu, Au, Fe, Pb, Ni, Pd, Pt, Ag, Ti, and W in the infrared and far infrared. *Applied Optics*, 22(7):1099–1120, 1983.

[39] H. J. Hagemann, W. Gudat, and C. Kunz. Optical constants from the far infrared to the x-ray region: Mg, Al, Cu, Ag,Au, Bi, C, and Al_2O_3. *Journal of the Optical Society of America*, 65:742–744, 1975.

[40] H. E. Bennett and J. M. Bennett. Optical properties and electronic structure of metals and alloys. *North-Holland, Amsterdam*, page 175, 1966.

[41] P. B. Johnson and R. W. Christy. Optical Constants of the Noble Metals. *Phys. Rev. B*, 6:4370–4379, 1972.

[42] D. B. Tanner and D. C. Larson. Electrical Resistivity of Silver Films. *Phys. Rev.*, 166(3):652–655, Feb 1968.

[43] M. A. Ordal, Robert J .Bell, R. W. Alexander Jr., L. L. Long, and M. R. Querry. Optical properties of fourteen metals in the infrared and far infrared: Al, Co, Cu, Au, Fe, Pb, Mo, Ni, Pd, Pt, Ag, Ti, V, and W. *Applied Optics*, 24:4493–4499, 1985.

[44] G. Fahsold, M. Sinther, A. Priebe, S. Diez, and A. Pucci. Adsorbate-induced changes in the broadband infrared transmission of ultrathin metal films. *Physical Review B*, 65:235408, 2002.

[45] G. Fahsold, A. Bartel, O. Krauth, N. Magg, and A. Pucci. Infrared optical properties of ultrathin Fe films on MgO(001) beyond the percolation threshold. *Phys. Rev. B*, 61(20):14108–14113, 2000.

[46] Gerhard Fahsold, Andreas Priebe, Norbert Magg, and Annemarie Pucci. An IR-transmission spectroscopical study of the influence of substrate surface defects on the morphology and the electronic structure of ultrathin Fe grown on MgO (001). *Thin Solid Films*, 364:177–180, 2000.

[47] G. Fahsold, A. Bartel, O. Krauth, and A. Lehmann. *Surface Science*, 433-435:162, 1999.

[48] G. Fahsold, Wolfgang Keller, Oliver Krauth, and Annemarie Lehmann. *Surface Science*, 402-404:790, 1998.

[49] M. Lust, A. Priebe, G. Fahsold, and A. Pucci. Infrared spectroscopic study of the CO-mediated decrease of the percolation threshold during the growth of ultrathin films on MgO (001). *SURFACE AND INTERFACE ANALYSIS*, 33(19):487–490, 2002.

[50] I. Chorkendorff and J. W. Niemantsverdriet. *Concepts of Modern Catalysis and Kinetics*. WILEY-VCH GmbH & Co.KGaA, Freiburg, 2003.

[51] R. A. Pelak and W. Ho. Low temperature surface photochemistry: O_2 and CO on Ag(110) at 30 K. *Surface Science*, 321(3):L233–L238, December 1994.

[52] M. Sakurai, T. Okano, and Y. Tuzi. Vibrational excitation of physisorbed CO_2 on a Ag(111) surface. *J. Vac. Sci. Technol. A*, 5(4):431–434, 1987.

[53] Thomas H. Wood and Miles V. Klein. Raman scattering from carbon monoxide adsorbed on evaporated silver films. *J. Vac. Scl. Technol.*, 16:459–461, 1979.

[54] A. M. Bradshaw and J. Pritchard. Infrared Spectra of Carbon Monoxide Chemisorbed on Metal Films: A Comparative Study of Copper, Silver, Gold, Iron, Cobalt and Nickel. *Proceedings of the Royal Society of London. Series A, Mathematical and Physical Sciences*, 316:169–183, 1970.

[55] R. Wichtendahl, M. Rodriguez-Rodrigo, U.Hrtel, H. Kuhlenbeck, and H. J. Freund. Thermodesorption of CO and NO from vacuum-cleaved NiO(100)and MgO(100). *physica status solidi (a)*, 173:93–100, 1999.

[56] J. Heidberg, M. Kandel, D. Meine, and U. Wildt. The monolayer CO adsorbed on MgO(100) detected by polarization infrared spectroscopy. *Surface Science*, 331-333:1467–1472, 1995.

[57] P. N. M. Hoang, S. Picaud, and C. Girardet. On the difficulty for finding the orientational geometries of adsorbed monolayers: illustration with the CO/MgO system. *Surface Science*, 360:261–270, 1996.

[58] R. Gerlach, A. Glebov, G. Lange, J. P. Toennies, and H. Weiss. Structure and dynamics of CO/MgO(001): a helium atom scattering study. *Surface Science*, 331-333:1490–1495, 1995.

[59] L. Marchese, S. Coluccia, G. Martra, and A. Zecchina. Dynamic and static interactions in CO layers adsorbed on MgO smoke (100) facelets: a FTIR and HRTEM study. *Surface Science*, 269-270:135–140, 1992.

[60] O. Krauth. *Untersuchung der Oberflächenverstärkten Infrarotabsorption am System Kohlenmonoxid auf dünnen Eisenfilmen*. Dissertation, University Heidelberg, 1999.

[61] J .H. Larsen, J. T. Ranney, D. E. Starr, J. E. Musgrove, and Campbell C. T. Adsoption erergetics of Ag on MgO (001). *Phys. Rev. B*, 63:195410–195417, 2001.

[62] M. H. Schaffner, F. Patthey, and W. D. Schneider. Growth study of silver on MgO(100)/Mo(100). *Surface Science*, 417:159–167, 1998.

[63] Jun-Hyung Cho and Kwang S. Kim. Oscillatory energetics of flat Ag films on MgO (001). *Phys. Rev. B*, 63:113408–113411, 2001.

[64] D. Fuks, S. Dorfman, F. Zhukovskii, Yuri, A. Kotomin Eugene, and A. Marshall Stoneham. Theory of the growth mode for a thin metallic film on an insulating substrate. *Surface Science*, 499:24–40, 2002.

[65] David Fuks, Simon Dorfman, Eugene A. Kotomin, Yuri F. Zhukovskii, and A. Marshall Stoneham. Theoretical Analysis of the Growth Mode for Thin Metallic Films on Oxide Substrates. *Phys. Rev. Lett.*, 85(20):4333–4336, 2000.

[66] Robach O., Renaud G., and Barbier A. Structure and morphology of the Ag/MgO (001) interface during in situ growth at room temperature. *Phys. Rev. B*, 60:5858–5871, 1999.

[67] Y. Nishikawa, T. Nagasawa, and K. Fujiwara. *Vib. Spectrosc.*, 6:43, 1993.

[68] G. Fahsold, A. Priebe, N. Magg, and A. Pucci. Non-contact measurement of conductivity during growth of metal ultrathin films. *Thin Solid Films*, 428:107–110, 2003.

[69] Bauer E. *Thin Solid Films*, 12:167, 1972.

[70] J. Tersoff, A. W. Denier van der Gon, and R. M. Tromp. *Phys. Rev. Lett.*, 72:266, 1994.

[71] M. C. G. Passeggi, Jr. J. E. Prieto, and R. Miranda. *Phys. Rev. B*, 65:35409, 2001.

[72] D. A. Steigerwald, I. Jacob, and Jr. W. F. Egelhoff. *Surface Science*, 202:472, 1988.

[73] M. Wuttig, B. Feldmann, J. Thomassen, H. Zillgen F. May, A. Brodde, H. Hannemann, and H. Neddermeyer. *Surface Science*, 291:14, 1993.

[74] J. Thomassen, F. May, B. Feldmann, M. Wuttig, and H. Ibach. *Phys. Rev. Lett.*, 69:3831, 1992.

[75] A. Kirilyuk, J. Giergiel, J. Shen, and J. Kirschne. *Phys. Rev. B*, 52:R11672, 1995.

[76] G. Fahsold, M. Sinther, A. Priebe, S. Diez, and A. Pucci. Influence of morphology on adsorbate-induced changes in thin-film dynamic conductivity. *Physical Review B (Condensed Matter and Materials Physics)*, 70(11):115406, 2004.

[77] Y. Yagil, M. Yosefin, D. J. Bergman, and G. Deutscher. Scaling theory for the optical properties of semicontinuous metal films. *Phys. Rev. B*, 43:11342–11352, 1991.

[78] S. Berthier and J. Peiro. Infrared Absorption of Nanocermets Close to the Percolation Threshold. *J. Phys. III France*, 7:537–547, March 1997.

[79] J. Heidberg and D. Meine. Polarized infrared spectra of CO_2 adsorbed on the MgO(100) single crystal surface. *Surface Science*, 279:L175–L179, 1992.

[80] Alexei V. Matveev, Konstantin M. Neyman, Ilya V. Yudanov, and Notker Rösch. Adsorption of transition metal atoms on oxygen vacancies and regular sites of the MgO(001) surface. *Surface Science*, 426:123–139, 1999.

[81] C. Revenant, G. Renaud, R. Lazzari, and J. Jupille. Growth of Ag on MgO (001) studied in situ by grazing incidence small angle X-ray scattering. *Nuclear Instruments and Methods in Physics Research B*, 246:112–117, 2006.

[82] C. R. Stoldt, A. M. Cadilhe, M. C. Bartelt, C. J.Jenks, P. A. Thiel, and J. W. Evans. Formation and relaxation of 2D island arrays in metal(100) homoepitaxy. *Progress in Surface Science*, 59:67–77, 1998.

[83] Oliver Krauth, Gerhard Fahsold, and Annemarie Lehmann. Surface-enhanced infrared absorption? *Surface Science*, 433-435:79–82, 1999.

[84] O. Krauth, G. Fahsold, and A. Pucci). Asymmetric line shapes and surface enhanced infrared absorption of CO adsorbed on thin iron films on MgO(001). *Journal of Chemical Physics*, 110(6):3113–3117, 1999.

[85] J. S. Parker K. R. McCrea and G. A. Somorjai. *J. Phys. Chem. B*, 106:10854, 2002.

[86] Wyckoff R. W. G. *Crystal Structures.* Wiley-Interscience, New York: V.1; ibid(1964): V.2, 2 edition, 1963.

[87] Jeffrey T. Ranney, David E. Starr, Jana E. Musgrove, Dan J. Bald, and Charles T. Campbell. A microcalorimetric study of the heat of adsorption of copper on well-defined oxide thin film surfaces: MgO (100), p(2×1) oxide on Mo(100) and disordered W oxide. *Faraday Discuss.*, 114:195–208, 1999.

[88] A. Priebe, F. Meng, and A. Pucci. IR spectra of adsorbates on rough metal films. *Asian J. Phys.*, 15:239, 2006.

Acknowledgement

I would like to thank everyone who supported me for finishing this thesis.

Special thanks go to

Prof. Dr. Annemarie Pucci for offering me the opportunity to study in this interesting field, for her patiently supervision and help, and for her kindly encouragement.

Dr. G. Fahsold for his instant solution of my problems.

Dr. A. Priebe for helping me on my starting in the lab and on the analysis of experimental results.

O. Skibbe for his kindly help on my computer problems, and for the useful tips and for the help during my thesis writing.

Prof. Dr. J. Bille for being the second referee of my thesis.

Specially I thank Robert and Matin for the modification of my manuscripts. I also thank all the current and former colleagues in the work group Pucci. I will miss the happy time that we spend together.

Finally I would like to thank all my families and friends for their supports, for sharing my joys and unhappiness in my life in Germany.

Special thanks to my husband.